2014

CONAE MicroWave Radiometer (MWR) Counts to Brightness Temperature Algorithm

Zoubair Ghazi
University of Central Florida

CONAE MICROWAVE RADIOMETER (MWR) COUNTS TO BRIGHTNESS TEMPERATURE ALGORITHM

by

ZOUBAIR GHAZI

M.S. Kiev International University of Civil Aviation, 2000
M.S. University of Central Florida, 2011

A dissertation submitted in partial fulfillment of the requirements
for the degree of Doctor of Philosophy
in the Department of Electrical Engineering and Computer Science
in the College of Engineering and Computer Science
at the University of Central Florida
Orlando, Florida

Fall Term
2014

Major Professor: Linwood Jones

ABSTRACT

This dissertation concerns the development of the MicroWave Radiometer (MWR) brightness temperature (Tb) algorithm and the associated algorithm validation using on-orbit MWR Tb measurements. This research is sponsored by the NASA Earth Sciences Aquarius Mission, a joint international science mission, between NASA and the Argentine Space Agency (Comision Nacional de Actividades Espaciales, CONAE). The MWR is a CONAE developed passive microwave instrument operating at 23.8 GHz (K-band) H-pol and 36.5 GHz (Ka-band) H- & V-pol designed to complement the Aquarius L-band radiometer/scatterometer, which is the prime sensor for measuring sea surface salinity (SSS). MWR measures the Earth's brightness temperature and retrieves simultaneous, spatially collocated, environmental measurements (surface wind speed, rain rate, water vapor, and sea ice concentration) to assist in the measurement of SSS.

This dissertation research addressed several areas including development of: 1) a signal processing procedure for determining and correcting radiometer system non-linearity; 2) an empirical method to retrieve switch matrix loss coefficients during thermal-vacuum (T/V) radiometric calibration test; and 3) an antenna pattern correction (APC) algorithm using Inter-satellite radiometric cross-calibration of MWR with the WindSat satellite radiometer. The validation of the MWR counts-to-Tb algorithm was performed using two years of on-orbit data, which included special deep space calibration measurements and routine clear sky ocean/land measurements.

ACKNOWLEDGMENTS

I would like to express my sincere gratitude and appreciation to my advisor, Dr. W. Linwood Jones, for his teaching and support to fully complete my research. His trust, endless support, and guidance in my research not only boosted my self-confidence but also helped me to overcome many challenges. I would like also to thank my committee members, Dr. Jeffrey Piepmeier (NASA), Dr. Mikhael Wasfy (UCF), Dr.William Junek (US Air Force), Dr. Lei Wei (UCF), and Dr. Thomas Wu (UCF), for their support and comments that strengthened my dissertation.

I would like also to thank Yazan Hijazin, Maria Marta Jacob, Andrea Santos-Garcia, and Spencer Farrar, for their endless support and guidance during my first days at the lab. Also many thanks to Schneider Larry, Saleem Sahawneh, Ruiyao Chen, Hamideh Ebrahimi, Matin Salemirad, Marco Pantalone, and Brad Clymer for the memorable moments we had together. I will be forever indebted to them.

I am indebted to my parents for their endless love and support. They always showed me the right path which boosted my self-confident to overcome many challenges in my way. I would like to thank my wife for her love, guidance, support, and bringing joy to my life in different ways. Thanks to my sisters and brother, Loubna, Ilham, and Othman, for their love and help that they provided me. This endeavor would never be successful without my family. Also, I would like to thank my friends, Rajib Khalid and Hamid Belfassi, for making life joyful.

TABLE OF CONTENTS

LIST OF FIGURES

LIST OF TABLES

CHAPTER 1
INTRODUCTION

The Aquarius/SAC-D is an Earth science satellite mission to obtain monthly, global, sea surface salinity (SSS) measurements [1]. This program is an international collaboration between the National Aeronautics and Space Administration (NASA) and the Argentine Space Agency (Comisión Nacional de Actividades Espaciales, CONAE). NASA developed the Aquarius instrument (an L-band salinity remote sensor) and provided the satellite launch from Vandenberg Air Force Base in California; and CONAE provided the SAC-D spacecraft, several instruments, telecommunications control and command, and science data acquisition.

1.1 Aquarius Science Objectives

The measurement of ocean salinity will provide a key to better understand the interaction between climate, ocean circulation, and the Earth's water cycle (land runoff, melting and freezing of the sea ice, precipitation and evaporation over the ocean). Over oceans, the sea surface loses the moisture (water vapor) into the atmosphere by evaporation, which causes the sea surface salt content (salinity) to increase. Conversely, the atmospheric circulation transports the ocean's water vapor to form clouds that produce precipitation (rain and snow) that eventually enters the ocean to reduce the salinity. Thus, the ocean SSS is a sensitive tracer of freshwater that will provide scientists to better understand the Earth water cycle and the role of ocean circulation on climate change.

The design of the AQ/SAC-D system is to provide a global SSS map every seven days using a polar-orbiting space-borne, and an active/passive remote sensor. Weekly observations are combined to produce global measurements of SSS on a monthly basis with a required accuracy of 0.2 psu (practical salinity unit) at a spatial resolution of 150 km. Figure 1.1 shows a global image of sea surface measurements provided by the Aquarius instrument during the time period between August 25, 2011 and July 7, 2012. The color scale is chosen to cover the dynamic range of SSS with red representing the highest salinity of 40 psu and the purple representing the lowest salinity of 30 psu.

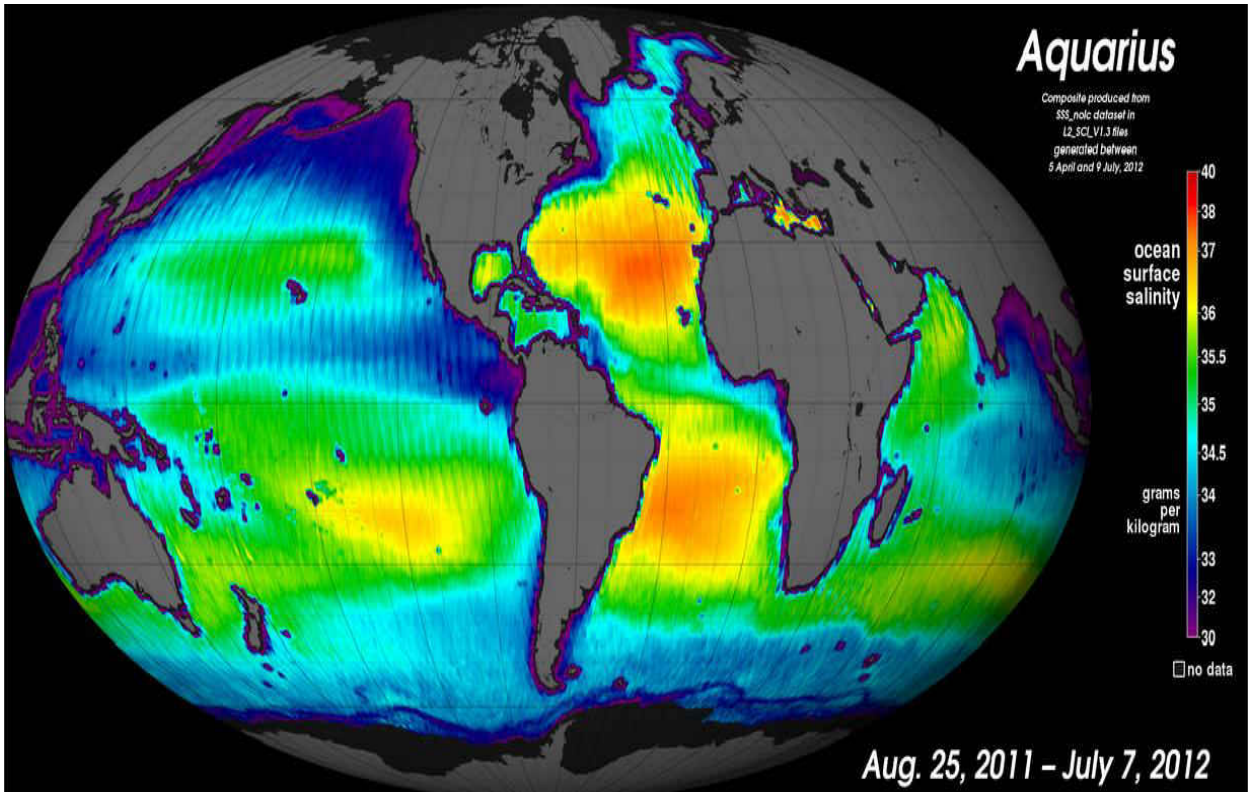

Figure 1-1 Global image of sea surface temperature during the first 10 months of Aquarius operation [18].

1.2 Aquarius/ SAC-D

The SAC-D spacecraft carries several instruments, but only two are relevant to this dissertation, namely: Aquarius and the MicroWave Radiometer (MWR). Figure 1.2 illustrates the Aquarius/SAC-D in the stowed launch configuration (left hand side panel) and in the deployed on-orbit configuration (right hand side panel).

The primary SSS remote sensor is Aquarius [2], a combined passive/active L-band microwave instrument operating at L-band (1.413 GHz, where the brightness temperature Tb is sensitive to changes in salinity). Because the observed brightness temperature also depends on surface roughness (ocean waves), Aquarius also includes a scatterometer operating at 1.26 GHz to provide a critical roughness correction for this effect.

The Aquarius SSS measurements are complemented by a CONAE sensor known as MWR. This instrument, which operates at 23.8 GHz (K-band) and 36.5 GHz (Ka-band), measures the ocean brightness temperature (Tb) and provides geophysical parameters such as rain rate, water vapor, ocean surface wind speed, and sea ice that are used to derive accurate sea surface salinity retrievals.

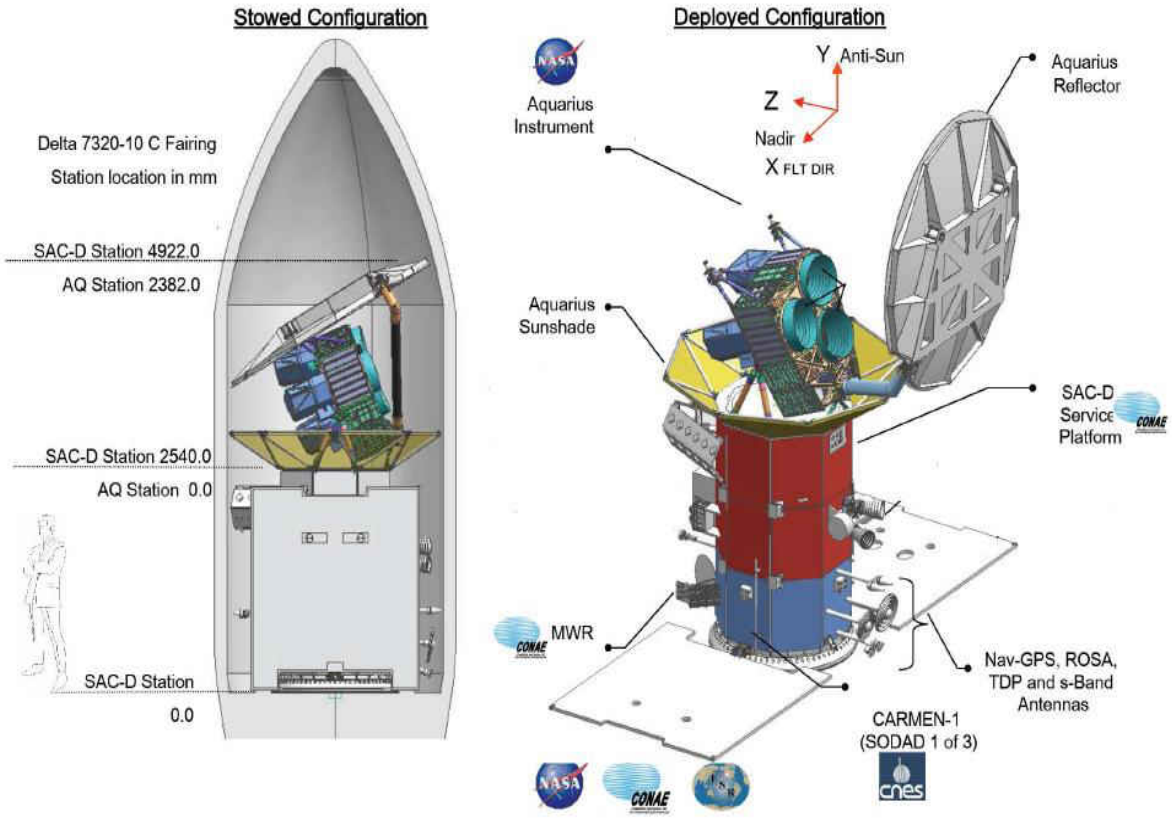

Figure 1-2 Stowed and deployed configurations of Aquarius instrument on SAC-D.

1.3 Aquarius Measurement Geometry

Since the Sun is an intense interference noise source at L-band; the AQ/SAC-D was designed to fly in a 98° inclined, sun-synchronous polar orbit with a sensor viewing away from the sun (dark side of the day/night terminator) as shown in Fig. 1.3. This orbit satellite assures that the Sun never crosses the orbit plane thereby reducing the unwanted effects of solar noise caused by sun glint off the ocean. Further, this repeating ground track orbit results in a global mapping of SSS in exactly 103 orbits (~7days).

The prime remote sensor of SSS, an active (radar)/passive (radiometer), is also named Aquarius. For the passive measurement, AQ consists of three Dicke radiometers that measure microwave brightness temperature in vertical and horizontal polarizations. The three radiometers are connected to three separate horn antennas that share a common 2.5-m offset parabolic reflector to produce three spot-beams. These beams view the surface in the cross-track direction producing three elliptical footprints at earth incident angles (EIA) of 29.3, 38.4 º, and 46.3 º for inner (red), middle (green) and outer (yellow) beams respectively [1, 2], and the corresponding instantaneous field of view (IFOV) are: 79 x 94 km, 84 x120 km, and 96 x 156 km, which results in a measurement swath of 390 km.

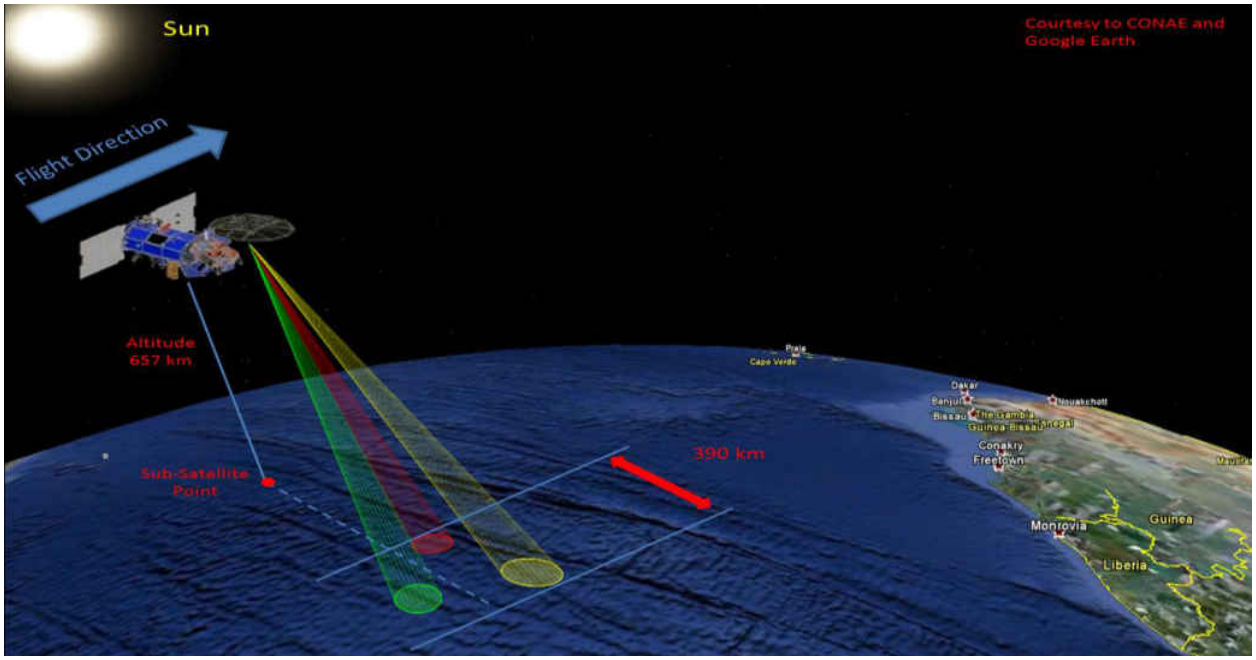

Figure 1-3 Aquarius footprints and on-orbit geometry

1.4 Dissertation Objective

The objective of this dissertation is the development of an improved version of the counts-to-Tb algorithm (V6.0) for the CONAE MWR Instrument. This research began with the comprehensive on-orbit evaluation of the previous version of counts-to-Tb algorithm (V5.0S), which was found to produce anomalous results. Based upon our discoveries, a new algorithm was developed and was successfully validated using inter-satellite radiometric calibration with the WindSat satellite radiometer. Results are presented and demonstrate that this new algorithm (V6.0) is fully compliant with MWR requirements.

This dissertation is organized into six chapters. Chapter 1: Introduction, presents the dissertation objective and an introduction to the Aquarius/SAC-D Mission. Chapter 2: MicroWave Radiometer (MWR), describes the MWR science objectives, the instrument design, and the on-orbit measurement geometry. Chapter 3: MWR Algorithm Counts-to-Tb Development, discusses the MWR algorithm (V5.0S) and presents anomalous Tb measurement performance related to the smear effect and to MWR system non-linearity. Chapter 4: Development of Counts-to-Tb Algorithm (V6.0), is the focus of this dissertation that describes innovative solutions to observed Tb measurement anomalies. Chapter 5: MicroWave Radiometer Post Launch Calibration and Validation, describes the post launch calibration and validation using CFRSL XCAL approach for inter-satellite radiometric comparison with the WindSat satellite radiometer. Chapter 6: Conclusion and Future Work, presents conclusions and recommendations for the next generation of counts-to-Tb V7.0 algorithm.

CHAPTER 2
MICROWAVE RADIOMETER (MWR)

2.1 MWR Science Objectives

CONAE developed the MWR science instrument to fly on AQ/SAC-D satellite to provide the retrieval of relevant geophysical parameters that support the AQ SSS mission objectives. Specifically, MWR measures simultaneous and spatially collocated brightness temperatures that are spatially and temporally collocated with the AQ 3-beam IFOV's. The choice of radiometer channels (frequencies and polarizations) was selected to retrieve the following environmental parameters; ocean surface wind speed, oceanic rain rate, integrated atmospheric water vapor, and sea ice concentration. These geophysical measurements (and other auxiliary data) are used by the AQ data processing system to derive an accurate sea surface salinity (SSS).

2.2 The MWR Instrument Description

MWR is a three-channel, push-broom, Dicke radiometer with noise injection for radiometric calibration, which is similar to the AQ L-band radiometer described by Tanner et al. [3] and the details of MWR are found in [4]. A simplified block diagram, shown in Fig. 2.1, consists of five major subsystems, namely; antenna, antenna switch matrix, radiometer receiver, power detector, and analog-to-digital electronics. Other subsystems, such as electrical power, thermal control and telemetry, are not germane to this dissertation and are therefore omitted.

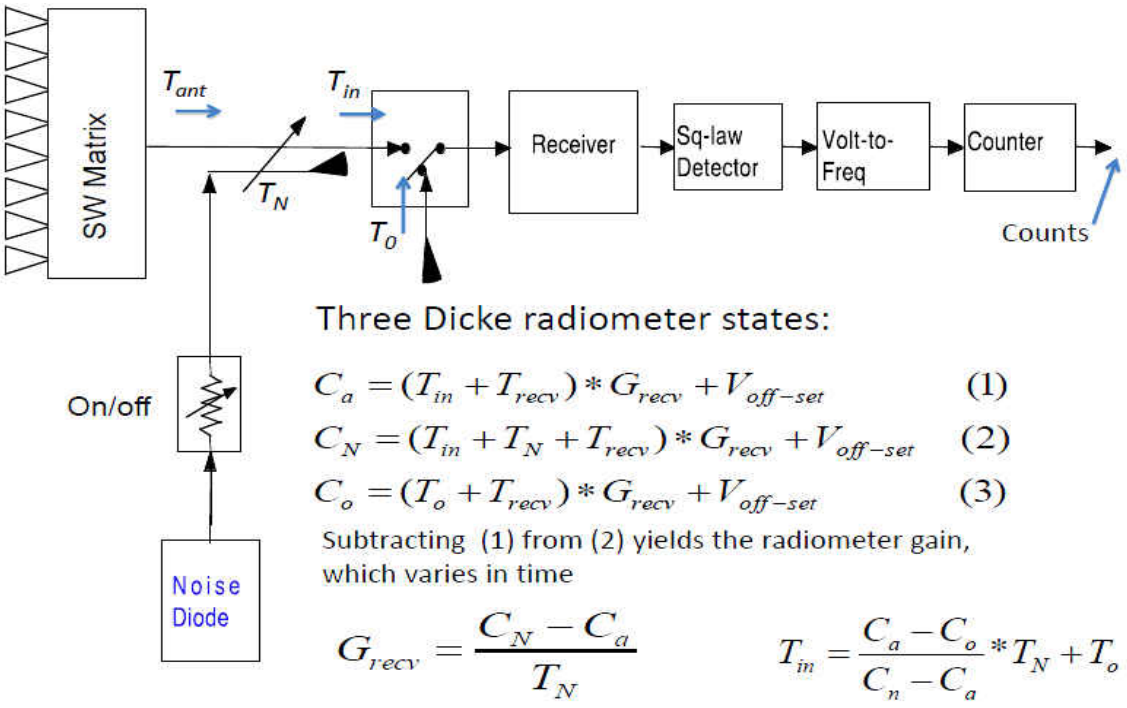

Figure 2-1 MWR radiometer block diagram with two internal calibration

Antenna Subsystem: The MWR antenna subsystem comprises two parabolic torus reflectors and associated feeds to produce two push-broom antennas, one looking forward (Ka-band) and one looking aft (K-band), as shown in Fig. 2.2 (a). Each reflector supports a different frequency band and a set of eight feed-horns arranged in two rows. The MWR IFOV's are approximately 50 km resolution and lie on two conical arcs (odd beams with earth incidence angle -EIA- of 52° and even beams with EIA = 58°) in cross-track direction within the AQ measurement swath. As shown in Fig. 2.2 (b), the 8 MWR beam footprints overlap the AQ beam swath, thereby providing greater than Nyquist spatial sampling.

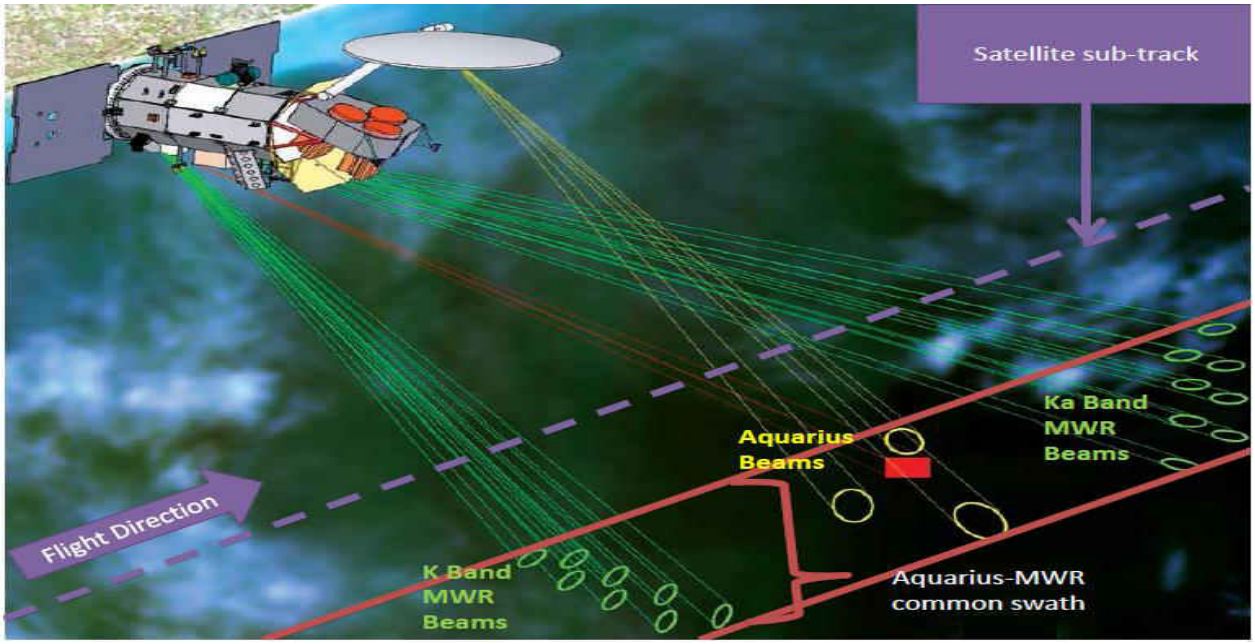

(a)

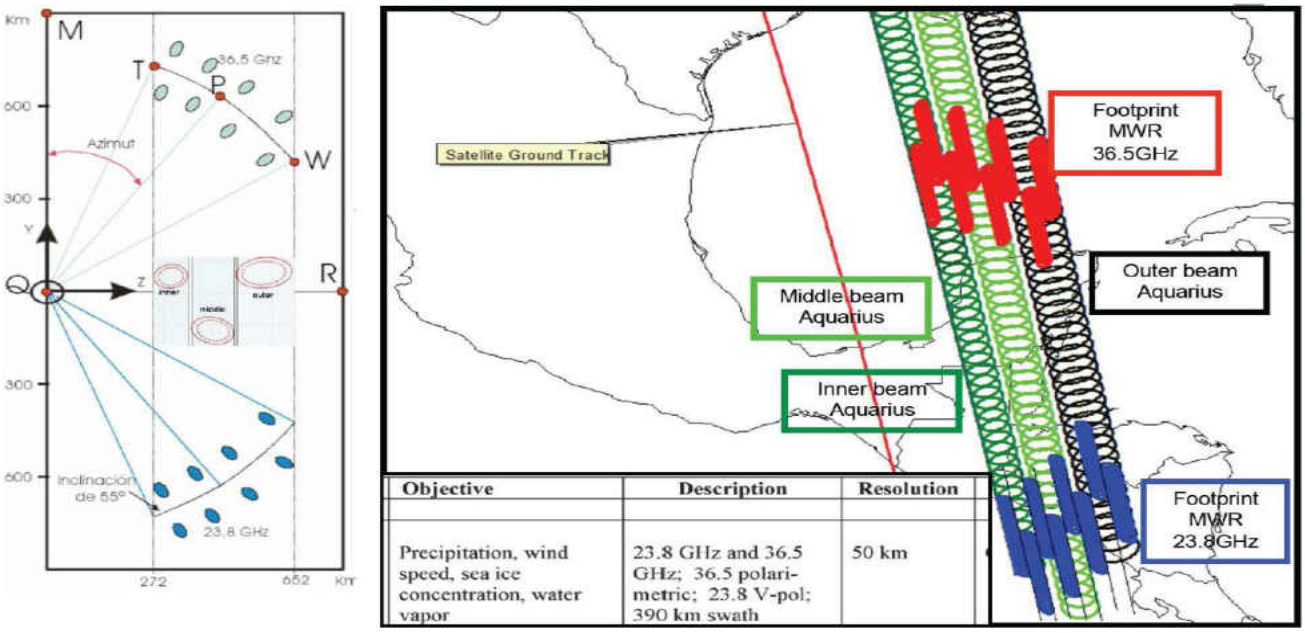

Objective	Description	Resolution
Precipitation, wind speed, sea ice concentration, water vapor	23.8 GHz and 36.5 GHz; 36.5 polarimetric; 23.8 V-pol; 390 km swath	50 km

(b)

Figure 2-2 Aquarius and MWR Geometry.

Antenna Switch Matrix: Three antenna switch matrices (ASM) are used to guide the polarized Tb signals captured by the feed-horns into the corresponding receivers. For each channel, the ASM was divided into three layers for a total of seven switches. Four switches were located at first layer (at the feed horns), two switches at the second layer, and one switch at the input to the directional coupler, as shown in Fig. 2.3. The ferrite circulator switches (magenta color) are electronically switched to a particular port by sending positive or negative current pulses to individual switch drivers to change the magnetic field polarity contained inside the switch. This results in the microwave propagation being either clockwise or counter clockwise within the circulator ferrite puck.

Radiometer Receiver and Power Detector: A microwave radiometer antenna delivers a very weak broadband noise to the receiver with the noise bandwidth higher than the receiver bandwidth. To make measurements in the desired pass-bands in the receiver, a band pass filter is used followed by an amplifier to increase the strength of the signal. Next, the desired signal is extracted by a square-law detector. The square-law output voltage follows the low frequency of the input power (envelop) and is proportional to the input. Next, the signal passes through an integrator (low-pass filter) to remove the high frequency fluctuation of the rectified RF noise and to estimate the mean noise power. Thus, the mean value of the detector output voltage is linearly proportional to the brightness temperature at the input of the receiver.

Analog-to-Digital Electronics: The first stage of the signal processing electronics is a function generator, which is a device that contains an oscillator to generate a waveform as an input to the analog signal. Then an analog signal conditioning is performed to manipulate and make the analog signal suitable at the input of the analog-to-digital converter where the signal is digitized.

2.3 MWR Noise Injected Dicke Radiometer

The detailed block diagram of the MWR is shown in Fig. 2.4 [5]. While the MWR measures 4 polarization states, this dissertation is concerned with only the horizontal and vertical polarized Tb measurement. At each feed there is an ortho-mode transducer (OMT) that separates the brightness temperature into H-pol and V-pol components, connected to two Dicke radiometers, which provide mitigation against the detrimental effects of receiver gain fluctuations [6]. Also, a two point radiometric calibration is provided by using two internal noise sources with different noise levels: 1) a blackbody waveguide termination at ambient physical temperature and 2) an active noise diode that produces an equivalent "hot" blackbody source.

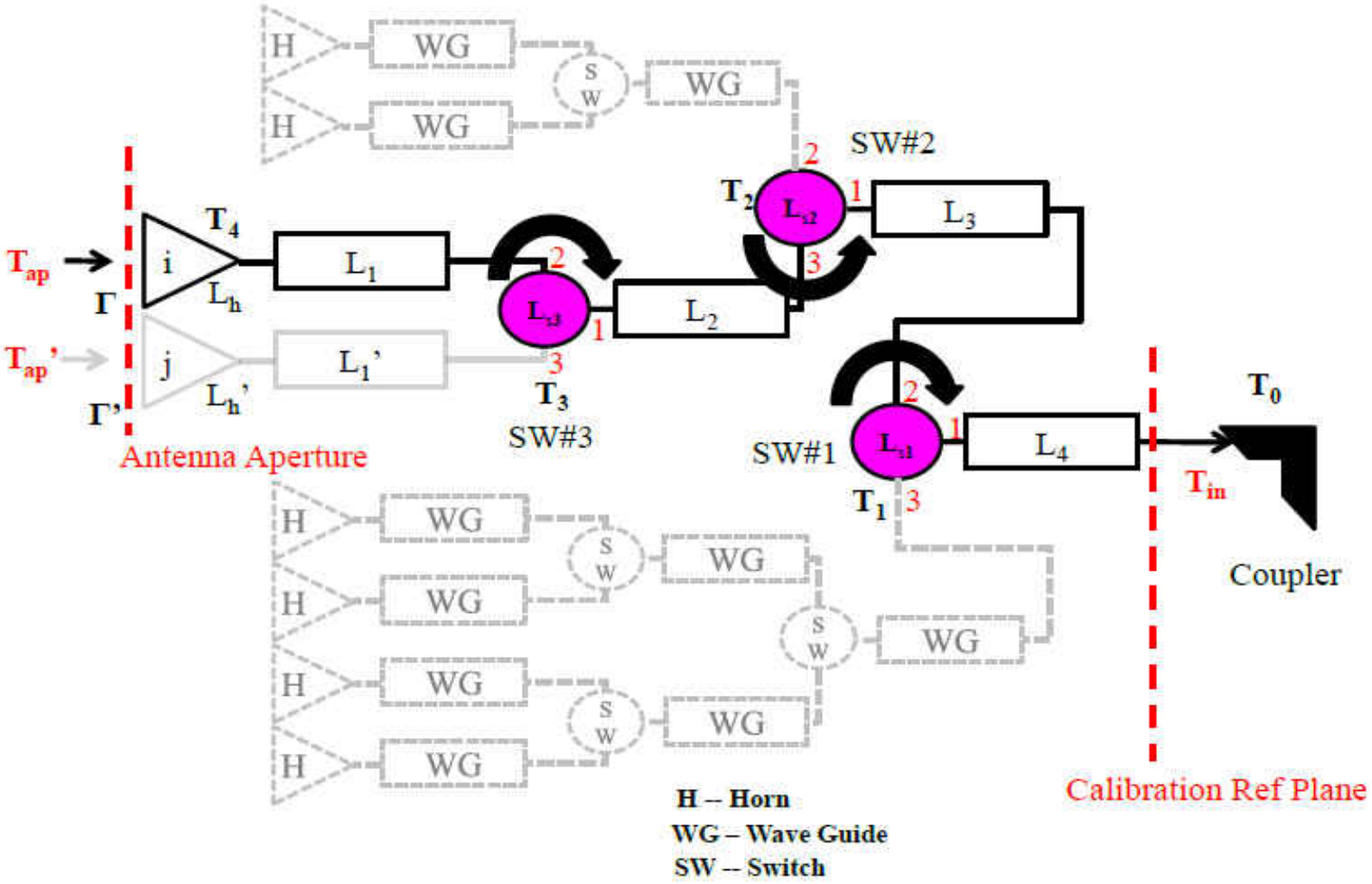

Figure 2-3 Simplified schematic of MWR antenna switch matrix.

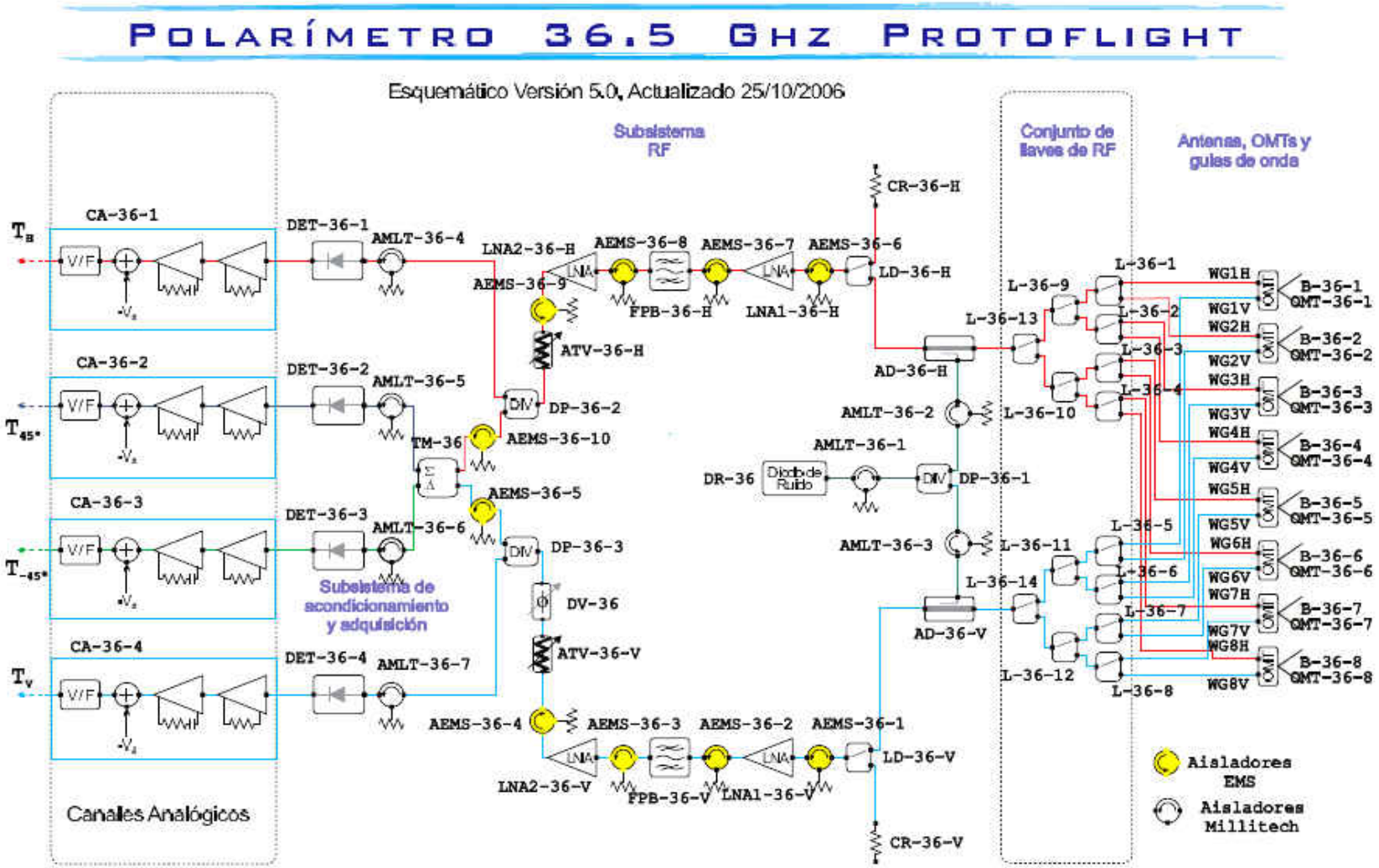

Figure 2-4 Schematic MWR Ka-band [5]

Using the three ASM's, each radiometer receiver time-shares the eight beams sequentially with a beam integration time of 0.24 s, as illustrated in the MWR timing diagram shown in Fig. 2.5, where the beam number corresponds to the feed horn number. Since there are eight beams with an integration time of 0.24 s, each beam is sampled once every 1.92 s. Note that the 0.24 s integration period is distributed into eight cycles, where each cycle includes measurements from; antenna, antenna + noise, and reference load. The cycle integration period is 9 ms to obtain a Tb, and 8 Tb's are averaged on-board to yield a single MWR Tb measurement sample for a given beam. The 1 ms interval between two cycles Tb's is used as a "blanking interval" (null measurement) to protect MWR from potential radio frequency interference from the AQ scatterometer transmit pulse [7].

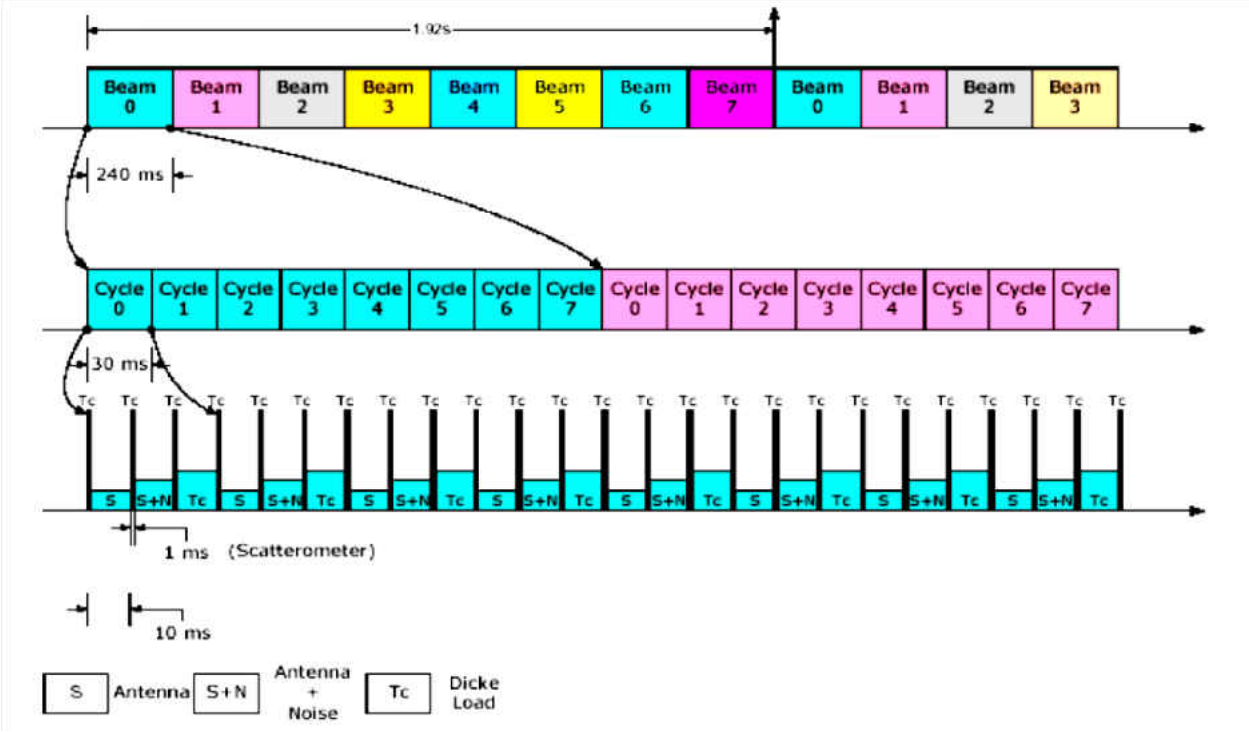

Figure 2-5 The MicroWave Radiometer Timing Diagram.

Radiometer Theory: A microwave radiometer is a very sensitive receiver that makes an absolute measurement of "blackbody emission" power from Earth's surface. The radiometer average noise power captured by the radiometer antenna is expressed as antenna brightness temperature and is defined as:

$$Tb = <P>/kB \tag{2.1}$$

where $<P>$ is the average noise power collected by the antenna, k is Boltzmann's constant and B is the receiver bandwidth.

CONAE MWR is a 3-state Dicke radiometer, and a simplified block diagram of the instrument is presented above in Fig. 2.1. The scene brightness temperature is captured by a feed horn and sequentially routed through the switch matrix to a directional coupler and then to the radiometer receiver input (antenna port of the Dicke switch). The directional coupler allows a Gaussian noise signal (noise diode of known brightness temperature) to be periodically turned on/off and then inject noise into the receiver, for radiometric calibration purposes. The Dicke switch is used to alternately sample the noise collected from the antenna (Dicke switch in antenna position), the antenna plus noise (Dicke switch in antenna position and noise diode is on), and the waveguide terminated in a matched load (Dicke switch in reference load position). After the signal passes through the receiver subsystem, it is detected by the square-law (power) detector, and this analog output voltage is digitized (using the voltage to frequency converter and a frequency counter) to produce the digital "Rad_counts" output.

Considering an ideal (total power) radiometer [6], the MWR radiometric transfer function that relates the output Rad_counts to the radiometer input brightness temperature (T_{in}) is linear

(Fig. 2.6). The slope of the linear regression represents the receiver power gain, which is independent of the input power. Thus, for the 3-Dicke radiometer states, the output counts are:

$$C_a = Gain * T_{in} + offset \tag{2.2}$$

$$C_N = Gain * (T_{in} + T_N) + offset \tag{2.3}$$

$$C_o = Gain * T_o + offset \tag{2.4}$$

where C_a is the radiometer digital output "antenna counts", C_n is the "antenna plus noise" counts, C_o is the "reference load" counts, T_o is the physical temperature of the reference load, T_n is the injected noise diode temperature (constant and known), and T_{in} is the brightness temperature at the antenna port of the Dicke switch.

By subtracting Eq. 2.2 from Eq. 2.3, the gain is derived as:

$$Gain = \frac{(C_N - C_a)}{T_N} \tag{2.5}$$

where C_N - C_a is defined as the noise diode deflection (deflection counts).

For a linear radiometer, the noise diode deflection and noise injection noise are constant and independent of the scene brightness temperature. From Eq. 2.5, it is concluded that the gain for a linear radiometer is also constant and independent of the scene brightness temperature. Using Eq. 2.5 and subtracting Eq. 2.4 from Eq. 2.2, the brightness temperature at the input of the Dicke switch at the antenna port is:

$$T_{in} = \frac{(C_a - C_o)}{(C_N - C_a)} * T_N + T_o \tag{2.6}$$

The next chapter applies the above radiometer theory to a discussion of the counts-to-Tb algorithm V5.0S.

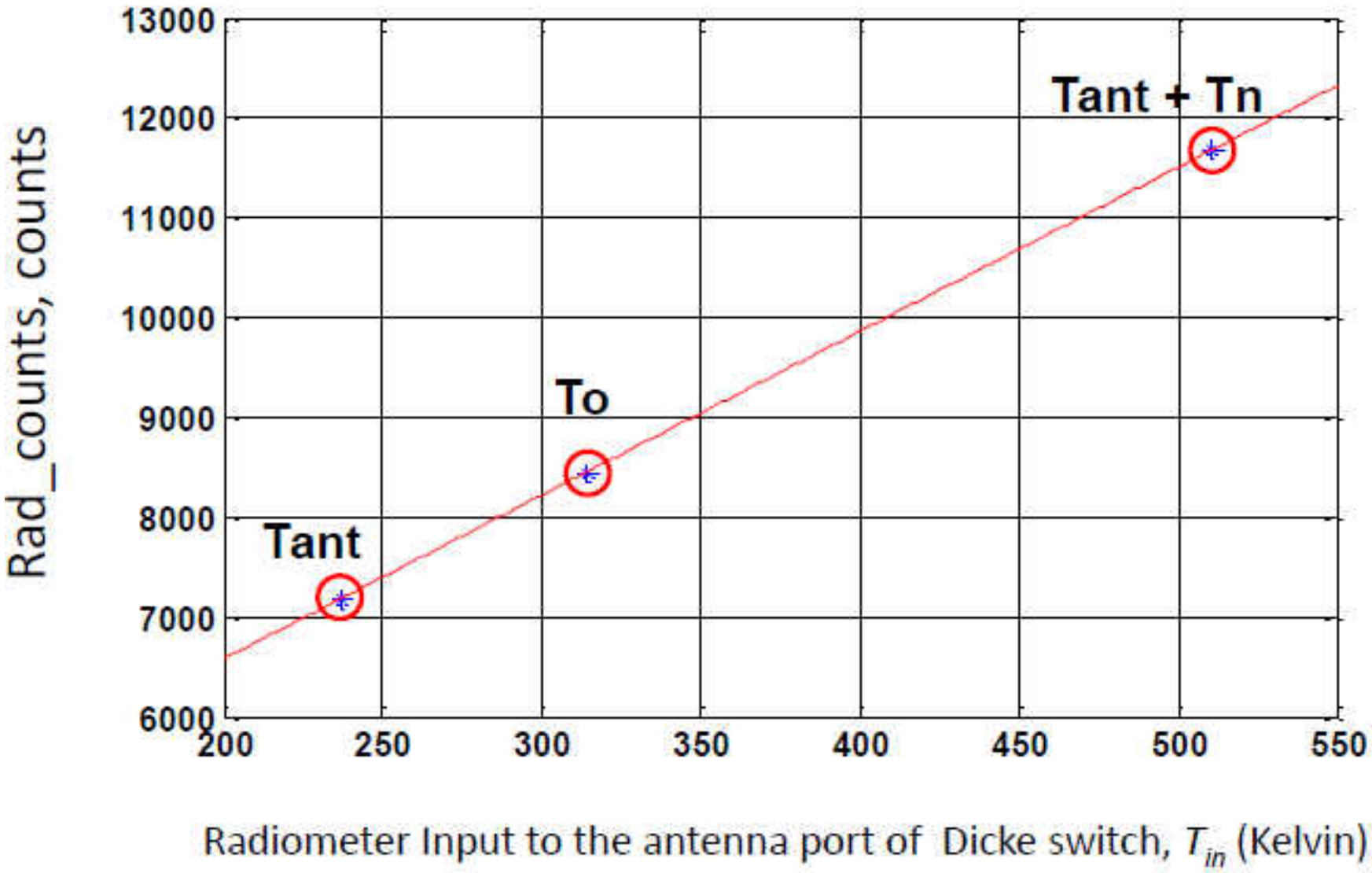

Figure 2-6 Typical Dicke radiometer transfer function.

CHAPTER 3
EVALUATION OF MWR ALGORITHM COUNTS-TO-TB (V5.0S)

A satellite microwave radiometer is a very simple instrument that measures power. It has no knowledge of the radiometric brightness of the earth scene, nor of which antenna beam is being sampled, nor of the satellite position in its orbit. In other words, the radiometer only responds to the magnitude microwave power presented at its input, and its transfer function (input power to output voltage) is independent of all external factors except the ambient physical temperature and the applied electrical power supply (voltage/current). Thus, a reasonable test is to examine the radiometer output voltage (digital counts) under a variety of on-orbit conditions to assure that this fundamental hypothesis is satisfied.

The initial (pre-launch) MWR counts-to-Tb algorithm was developed in 2011 by Biswas [7]. This research effort included the analysis of the pre-launch laboratory testing, the development of a statistical regression algorithm (version 2.0) using MWR thermal vacuum radiometric calibration data, and limited post-launch Tb algorithm calibration/validation (CAL/VAL) using ~ 90 days of on-orbit data. At the end of this period, a modified Tb algorithm (V2.1) resulted, and within the next 6 months, an improved V5.0 was developed and was used to provide MWR Tb data for engineering and scientific utilization. It is important to note that the development of V5.0 is not part of this dissertation; but the Tb validation and the associated algorithm improvements resulting in V6.0 is. To provide background information, a brief overview of the development of V5.0 follows.

3.1 MWR Algorithm Counts-To-Tb (V5.0)

The V5.0 algorithm was the result of the on-orbit calibration/validation (CAL/VAL) analysis that occurred during the first 6 months following MWR turn-on (September, 2011 thru February, 2012). A critical part of this process was the inter-satellite radiometric calibration (XCAL) [8] with the well calibrated WindSat polarimetric radiometer [9] that was developed by the Naval Research Laboratory and operates on board the USAF Coriolis satellite.

Fortunately, the MWR channel frequencies and polarizations are a subset of the WindSat radiometer channels, and the AQ/SAC-D and Coriolis fly in similar sun-synchronous orbits. Thus, on a weekly basis, the orbits drift with respect to one another such that on average ~ 60% of MWR data can be collocated with WindSat data, within ±1hr as described by Kahn [10].

Since the scientific objectives of MWR support those of the AQ sea surface salinity mission, the primary MWR Tb validation was for ocean scenes. The polarized (V- & H-pol) ocean brightness temperature depends on the atmospheric and oceanic environmental parameters, on the earth incident angle (EIA), and on the channel frequency. Because MWR and WindSat have different earth incident angles, a theoretical radiative transfer model [8] was used to adjust the WindSat brightness temperatures at EIA = 53° to the corresponding values of MWR odd beams (EIA = 52°) and even beams (EIA = 58°) before XCAL comparisons were performed.

Further, the design of MWR is a push-broom system with 8 antenna spot beams, which are time multiplexed into a single receiver (for each of 3 radiometer channels). This time-division multiplexing is achieved by a 1 x 8 antenna switch matrix (ASM, see Fig. 2.2). Because the losses in each path are not matched, the radiometric calibration is equivalent to 3 x 8 = 24 separate radiometers.

The V2.0 Tb algorithm employed a statistical regression using MWR thermal vacuum radiometric calibration data to find the ASM losses (b-coefficients). The scene brightness temperature (Tb) received by each MWR feed is calculated using the inverse model:

$$T_b = b_1 + b_2 T_{in} + b_3 T_{in}^2 + b_4 T_o + b_5 T_{av} \tag{3.1}$$

where T_o is the physical temperature of the internal calibration reference load of the corresponding MWR receiver, T_{av} = (*T1*+*T2*+*T3*+*T4*)/4, where *T1*, *T2*, *T3* are the physical temperatures of the 3 switch levels in the ASM and *T4* is the physical temperature of the antenna feed-horns. The quadratic term $b_3 T_{in}^2$ is an ad hoc correction for the radiometer system non-linearity, and T_{in} is the MWR antenna temperature at the antenna port of the Dicke switch, which is computed from the digital counts (Eq. 2.6).

For V5.0, the coefficients in (Eq. 3.1) were derived from the on-orbit XCAL data. Since T_{in}, T_o, T_{av} are measured, the WindsSat Tb's adjusted to the MWR EIA's were used in the equation to obtain the regression coefficients b1 through b5. The WindSat brightness temperatures include the antenna pattern correction (APC); therefore, no explicit APC correction to convert T_{ant} to Tb is necessary in this version of the calibration algorithm. All the coefficients are tabulated in Appendix-A.

After collecting several months of on-orbit data, the detailed evaluation of V5.0 revealed two major anomalies, namely; the "smear effect" and the MWR system non-linearity, which are described in the following sections.

3.2 MWR Smear Effect

While the MWR smear correction is not a part of this dissertation, it is very relevant; thus a brief discussion is given below and more details are provided in Appendix – B.

Based upon an analysis of MWR Tb's (V5.0), it was observed that the brightness temperature of all channels were anomalous at high contrast radiometric scenes (e.g., land/water crossings). The Tb transitions from land to water appear to be displaced relative to the coast-line map that caused a "smearing" of the radiometric land/water boundary, as illustrated in the left side panel of Fig. 3.1. Further, this effect can be better seen in the corresponding Tb time series of beams #1 and #7 shown in Fig. 3.2. Here the Tb for each beam has an anomalous step function change, which precedes (beam #1) and lags (beam #7)) as the beam IFOV passes over the land/water boundary. The initial evaluation suggested an antenna sidelobe issue; but subsequent analysis by CONAE [11], revealed that the cause is a cross-coupling of signals from different beams.

CONAE developed an empirical method to correct the smear effect, and the performance of this algorithm is excellent, as illustrated in Fig. 3.1 (right hand panel) and its corresponding time series (Fig. 3.2). When applying the smear correction, it can be seen that the effect is mitigated for all the beams, and the step function change was removed. After a comprehensive on-orbit evaluation, the smear correction was adopted and the subsequent counts-to-Tb algorithm was named V5.0S, where "S" stands for smear correction. These are the data which are used in this dissertation.

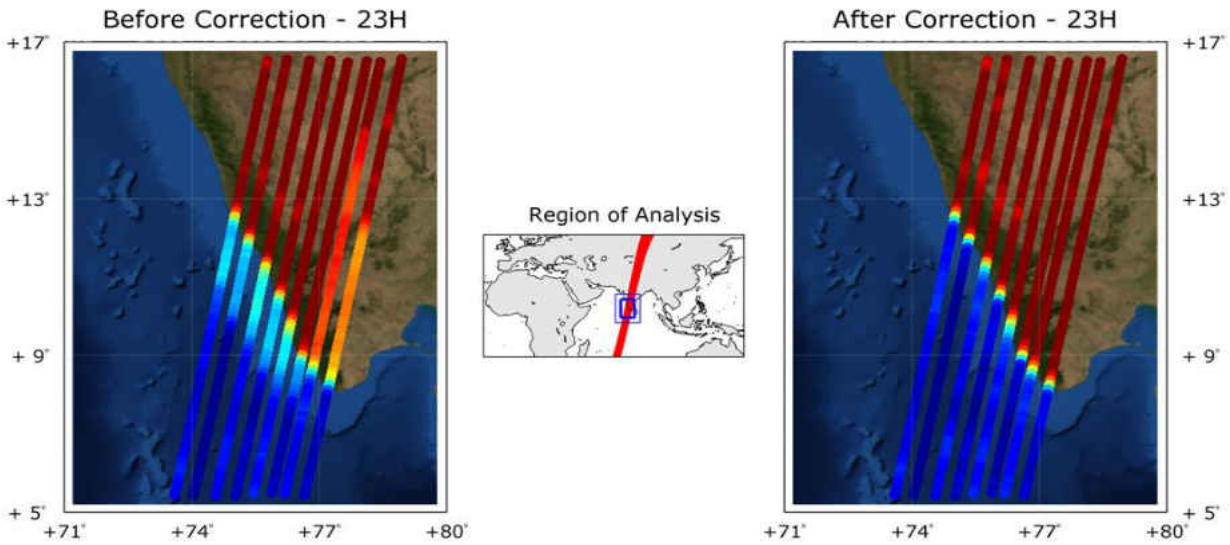

Figure 3-1 MWR Tb measurements for 8 beams of the 23 GHz H-pol channel during a descending orbital pass over the tip of India .

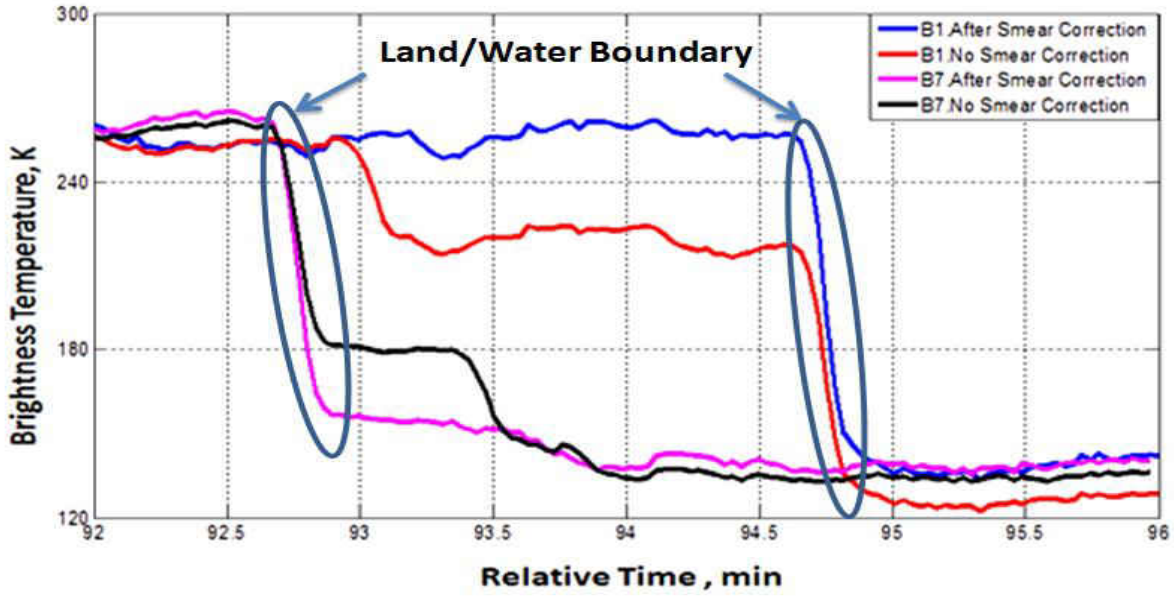

Figure 3-2 Corresponding MWR Tb time series for beam # 1 and beam # 7 of the MWR 23.8 GHz channel shown in Fig. 3.1. Red and black curves are before smear correction and blue and magenta curves are after smear correction

3.3 MWR System Non-Linearity

The MWR instrument was designed to be linear, and this was a fundamental requirement to obtain accurate brightness temperature measurements of the variable earth scene. However, based upon pre-launch calibration test of noise diode deflection (NDD), it was discovered [7] that the gain compression occurs for scene Tb's approaching 300K. Thus, an empirical second-order term was included in the counts-to-Tb algorithm to compensate for the MWR gain compression.

The starting point for the present dissertation was after the smear effects have been removed; therefore, this dissertation performed an evaluation of the MWR linearity based upon Tb V5.0S. A special emphasis was placed on verifying that the empirical non-linearity correction of Biswas [7] was not adequate to produce a linear radiometer transfer function. Specifically, a study was conducted to characterize the NDD counts (C_n - C_a) as a function of the radiometer input brightness temperature (i.e., output of the ASM, T_{in}), and the results of that study are presented below.

For an ideal linear radiometer receiver with constant gain, the simulated NDD are constant and independent of the scene brightness temperature. This is illustrated in Fig. 3.3 as simulated global images of MWR NDD for 14 orbits (~ one day) separated by ascending and descending passes. Note that the width of the MWR measurement swath is 380 km for 8 antenna beams.

However, under typical on-orbit conditions, the orbital receiver physical temperature (T_o) changes, and this produces a corresponding linear variation in the system gain. On orbit, the MWR baseplate physical temperature was controlled by an active thermal control subsystem, which resulted in a highly repeatable pattern of < 1 K peak-to-peak (Fig. 3.4). Further, this

produced a corresponding change of the NDD (system gain) as shown in the scatter diagram Fig. 3.5, where the % change in NDD ~ -1.0 %/K (increasing physical temperature of the receivers cause the NDD to decrease).

Using these results, the simulated orbital pattern of expected NDD was calculated (Fig. 3.6) and over a single day, each orbit revolution (rev) had a nearly identical physical temperature cycle. Thus, the pattern of simulated NDD was the same and did not exhibit any dependence on the radiometric scenes, i.e., same value for radiometrically hot land and radiometrically cold ocean.

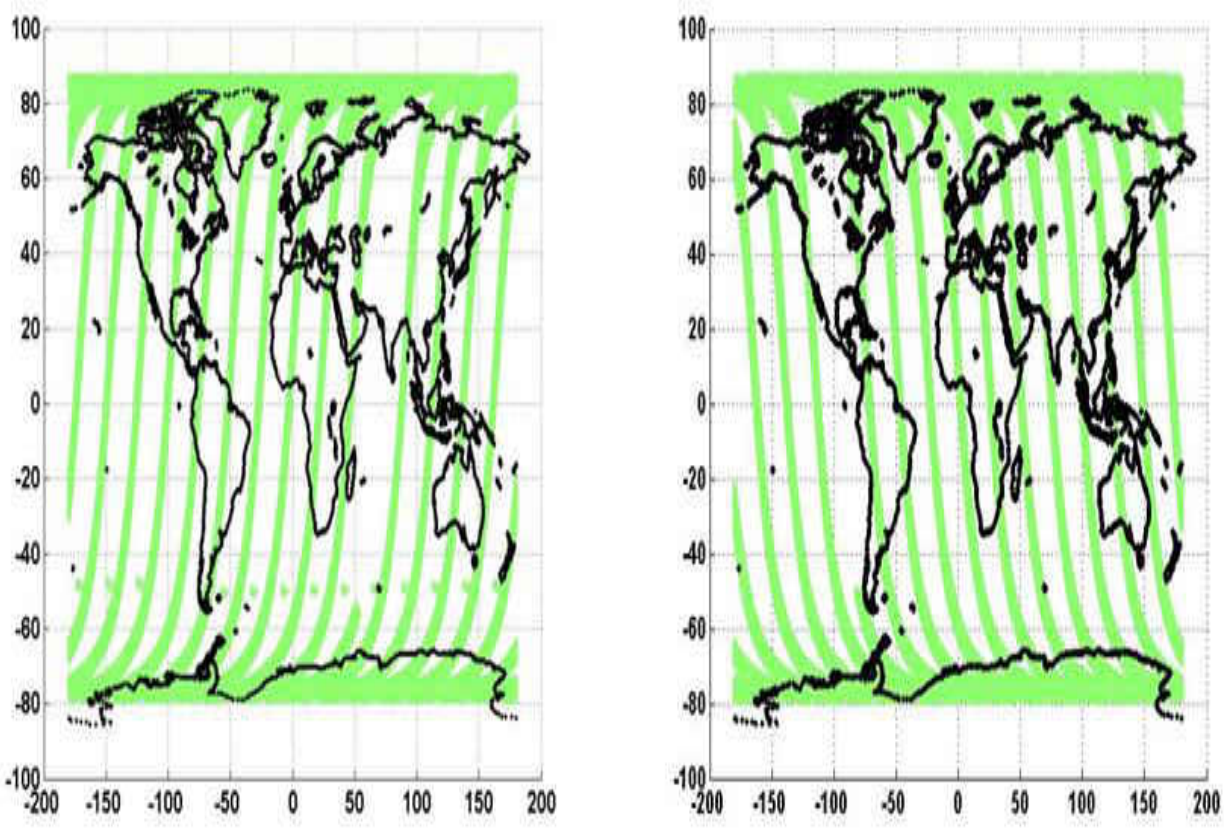

a) Descending b) Ascending

Figure 3-3 Simulated image of noise deflection counts for a linear radiometer with constant gain.

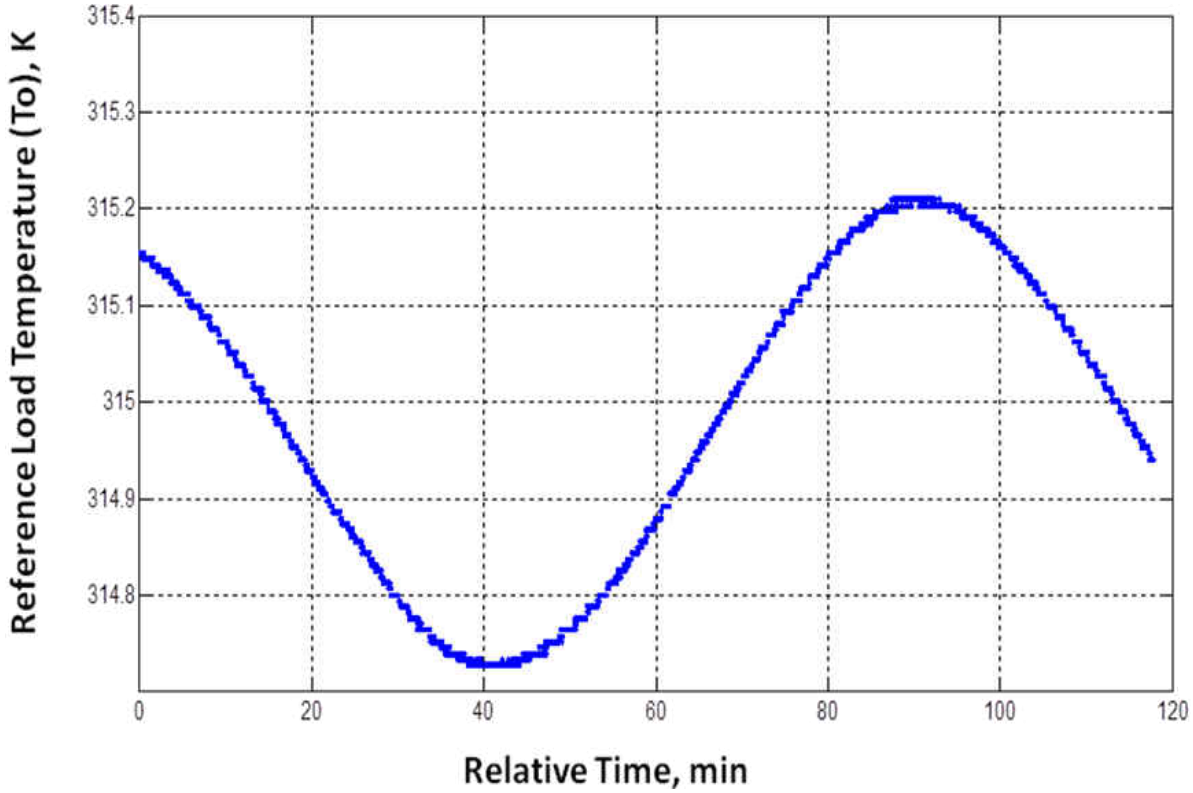

Figure 3-4 Time series of the reference load temperature (To) over a typical orbital period.

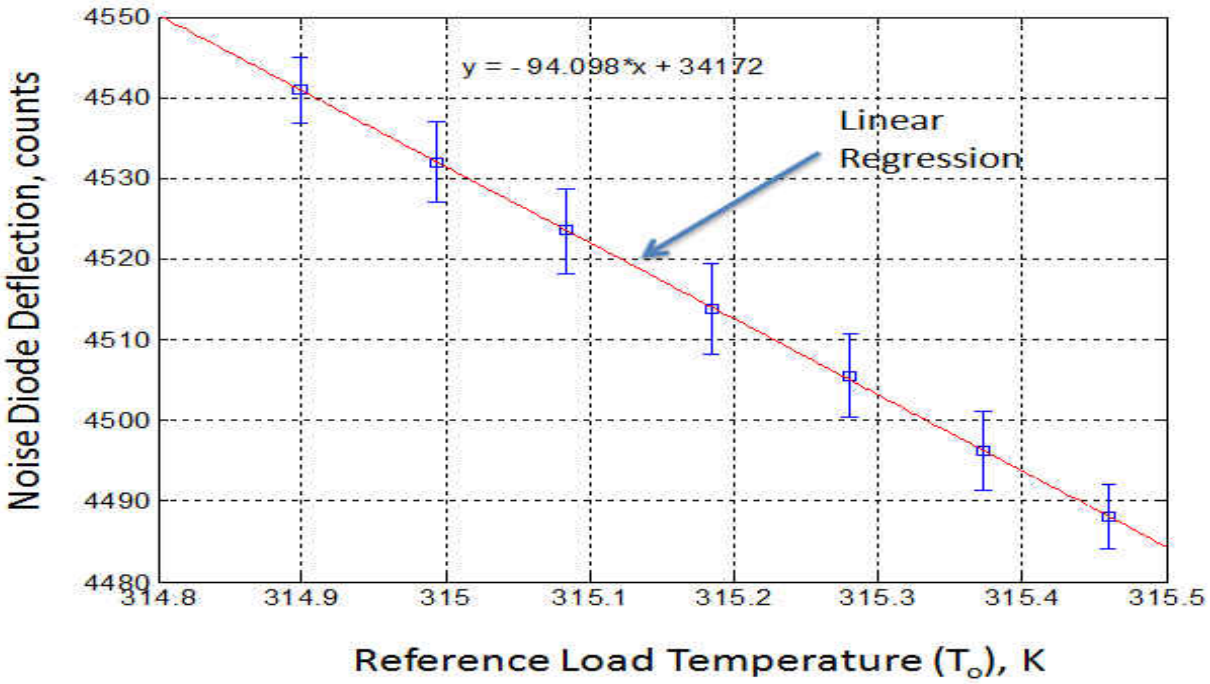

Figure 3-5 Relationship between noise diode deflection (C_n-C_a) and the baseplate physical temperature (To) – typical result for one

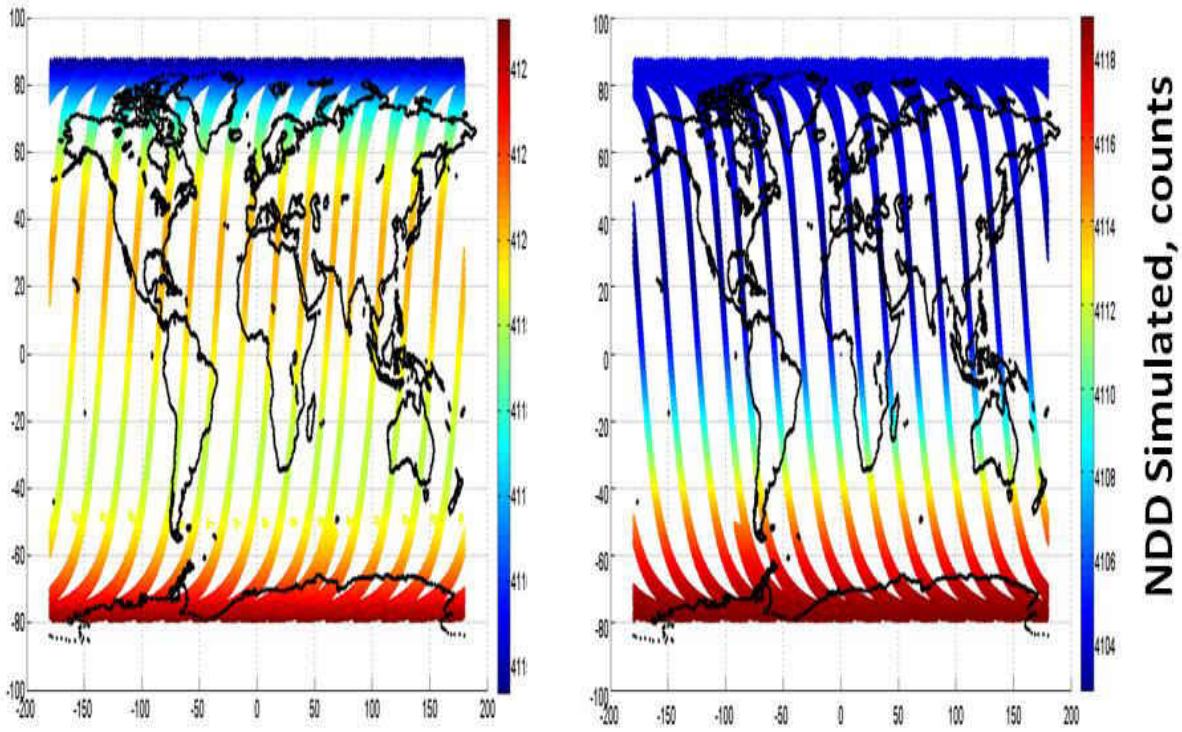

a) Descending b) Ascending

Figure 3-6 Simulated image of an expected noise deflection counts for a linear radiometer with sinusoidal physical temperature changes, where colors represent the noise diode deflection.

Next, the differential noise diode deflection image was produced by subtracting the observed pattern of MWR NDD (Fig. 3.7) from the simulated pattern (Fig. 3.6). Results are shown in Fig. 3.8, where the color bar is the differential NDD (after subtracting the mean difference that was calculated separately for ascending and descending revs). Note that the simulated and observed patterns had much similarity over oceans; but over land, there significant step-wise NDD decreases at land/water boundaries. This anomaly was observed in all MWR receivers (37V, 37H, 23H), which was correlated with the antenna scene Tb.

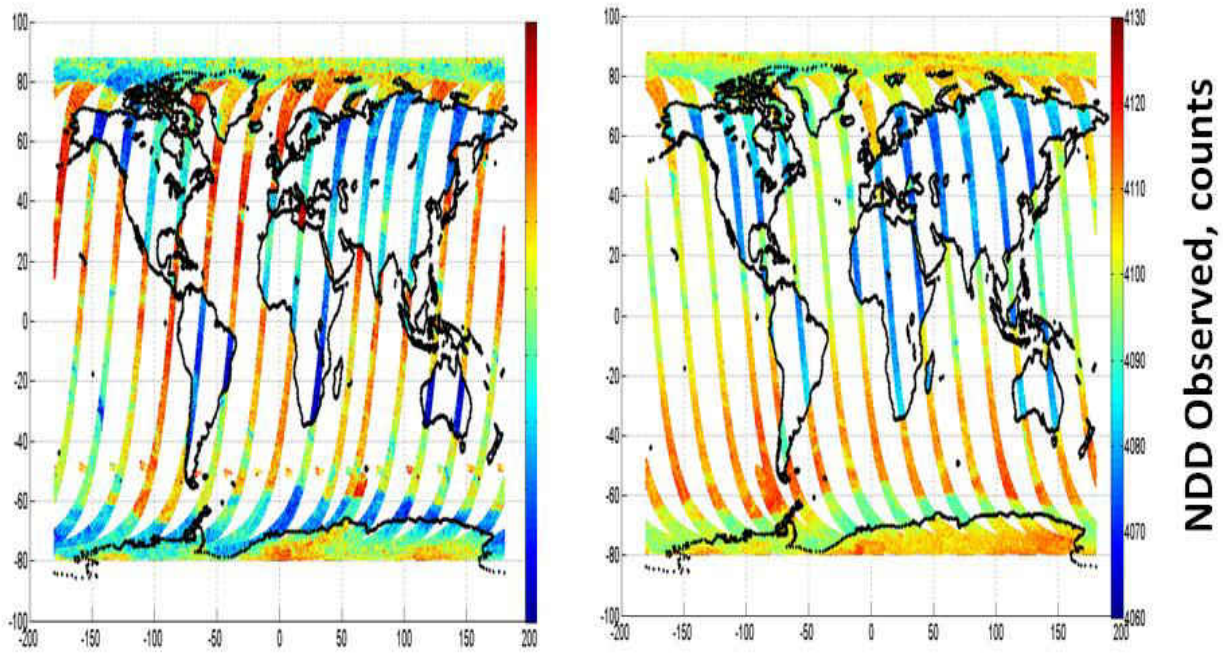

a) Descending b) Ascending

Figure 3-7 Image of observed noise deflection (Cn - Ca) for 36.5GHz H-pol. Warm colors indicate higher than average noise deflection and cool colors indicate less than average counts.

Further, to illustrate that the NDD steps occur whenever the scene changes, the noise diode deflection time series was plotted for one particular orbit, where the spacecraft is pitched-up to cause the MWR antenna to view radiometrically cold space during one portion of the orbit (see Fig. 3.9). This maneuver, known as a "Deep Space Calibration" (DSC) [9, 12], provided a wide dynamic range of scene brightness temperatures for the MWR channels. In this figure, the observed NDD for 36.5 GHz H-pol channel decreased abruptly whenever the antenna Tb transitioned from radiometrically cold to hot scenes and vice versa.

Obviously, the observed inverse correlation of the NDD with the geophysical scene Tb was anomalous and the empirical correction provided in V5.0S was not adequate. The solution for this issue is discussed next.

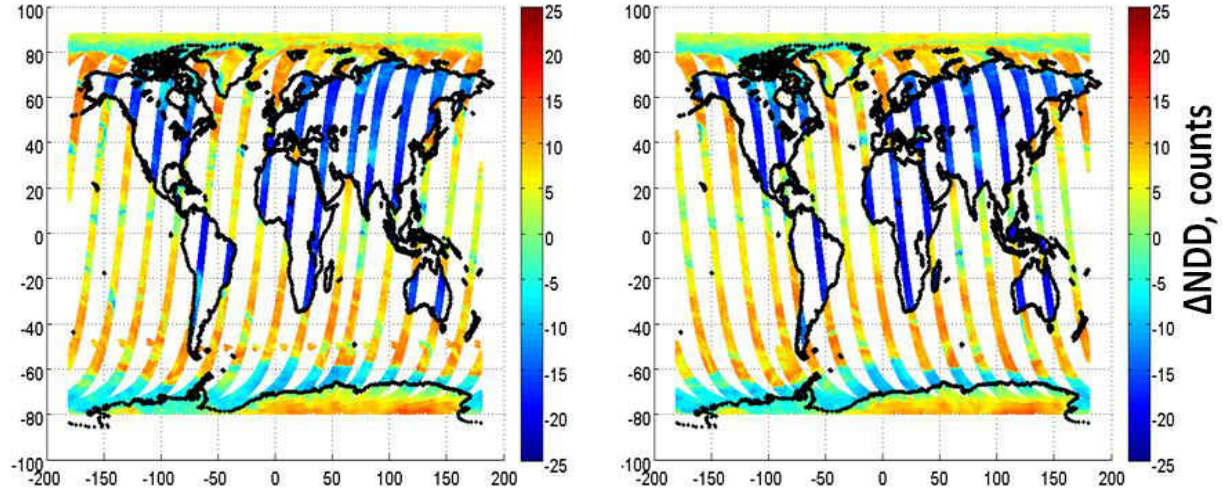

a) Descending b) Ascending

Figure 3-8 Image of the difference between observed and simulated NDD's for the 36.5 GHz H-pol channel, which exhibits a strong decrease of the NDD over land. The color scale is the differential NDD with the mean removed (separately for ascending and descending revs).

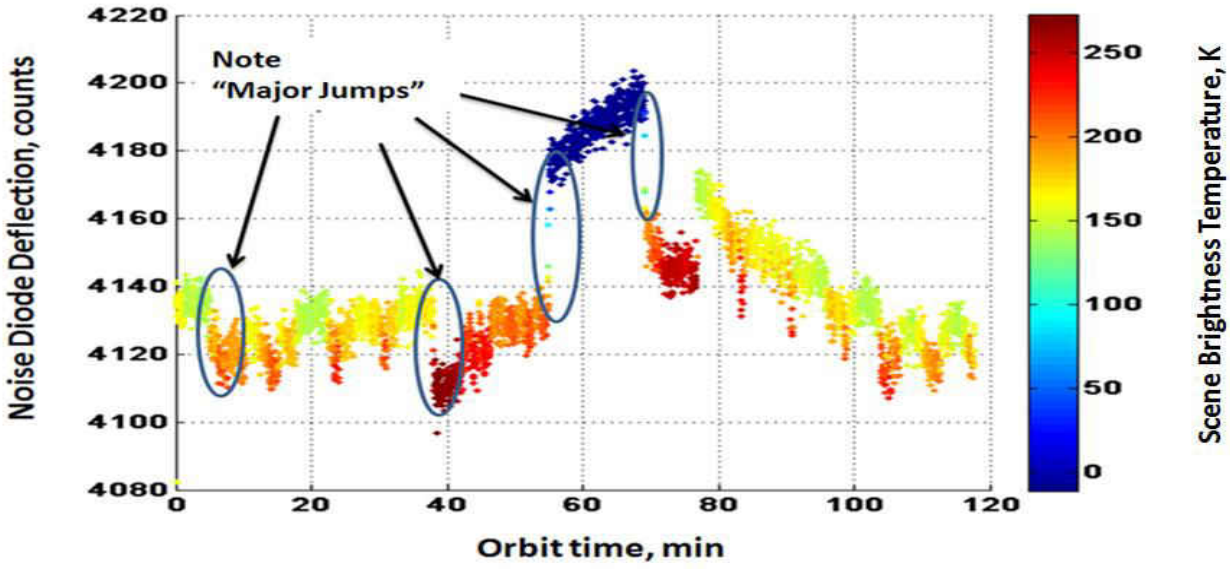

Figure 3-9 MWR noise diode deflection counts for 37 GHz V-pol channel, during a typical deep space calibration orbit. The colorbar represents the scene brightness temperature that ranges from cold space (blue) to hot land (red). Note the significant NDD jumps at rapid changes in scene temperature.

3.4 Characterization of MWR Gain Non-linearity

As described above, the changes in MWR gain (NDD) with the radiometric scene Tb was indicative of non-linear (anomalous) system response, which was most likely from the square-law detector. To characterize this effect, it was necessary to measure the total power radiometer transfer function [6] on-orbit, which presented several challenges.

First, it was necessary to remove the effect of a time variable radiometer gain that was the result of the orbital cycle of receiver physical temperature, T_o (see Fig. 3.4). In the Counts-to-Tb algorithm, the instantaneous gain was determined using the NDD; however, this was shown (section 3.3) to exhibit anomalous changes with the antenna scene Tb. Therefore, the gain normalizing procedure was developed using the reference load counts (C_o) and the measured T_o, and the instantaneous normalized reference counts ($C_{o\_norm\text{-}i}$) were:

$$C_{0\_norm_i} = C_{0_i} * \frac{< Gain >}{Gain_i} \tag{3.2}$$

where

$C_{o\text{-}i} = (To_i + <Trec>) * Gain_i$

To_i is the instantaneous reference load physical temperature in Kelvin

$<Trec>$ is the orbit average receiver noise temperature

$Gain_i$ is the instantaneous system gain

$<Gain>$ is the orbit average gain

To evaluate the effectiveness of the gain normalization procedure (Eq. 3.2), an experiment was performed to examine the reference counts before and after gain normalization. First, the time series of the reference load counts (colored curve) and reference load temperature T_o (black color) were plotted over an orbital period as shown in Fig. 3.10 (a). For ease of presentation, the means were removed to compare the patterns of these variables. The change in C_{oi} was the result to two effects, namely: 1) the change in system gain with T_o, and 2) the blackbody emission of the reference load (being proportional to T_o).

Next, the gain normalization procedure was applied to the reference counts and the corresponding time series was plotted in Fig. 3.10 (b). Before the counts normalization (Fig. 3.10 a), the reference load counts (C_o) and T_o were out of phase, and the effects of variable system gain dominated. On the other hand, after gain normalization (Fig. 3.10 b), the effects of variable gain were removed, and the peak-to-peak change of C_o was reduced by an order of magnitude. However, the reference counts were not constant because the reference load physical temperature and the blackbody emission were changing over the orbit such that:

$$\Delta C_{o\_norm} = \Delta T_o * < Gain > \tag{3.3}$$

where

$\Delta C_{o\_norm} = C_{o\_norm\text{-}i} - < C_{o\_norm} >$

$\Delta T_o = (T_{oi} + Trec) - < T_o + Trec >$

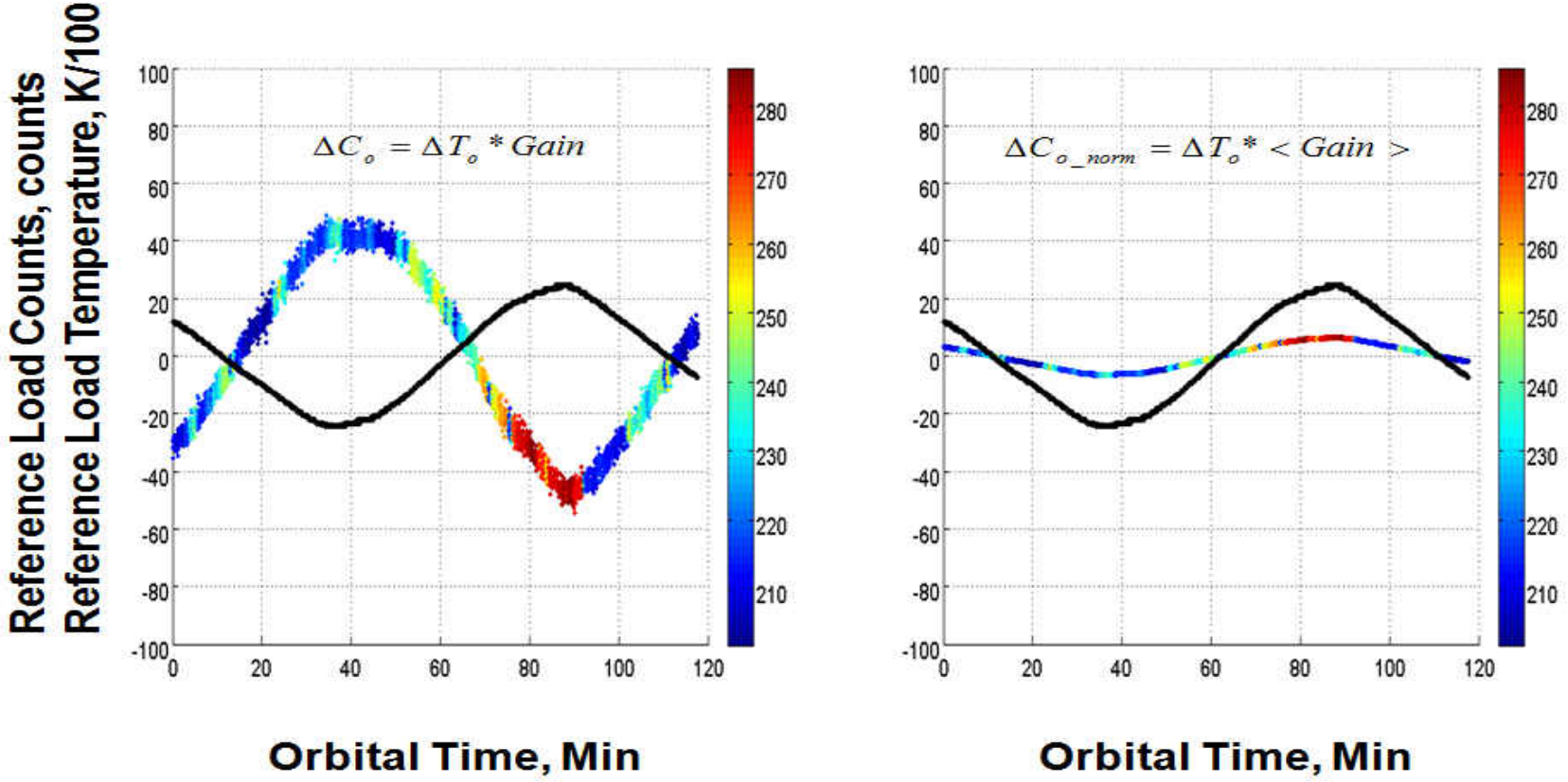

(a) (b)

Figure 3-10 Time reference load counts (multicolor) and reference load temperature (black color), a) before gain normalization, b) after gain normalization. Note that in the time series of the reference load counts, the color represents the scene brightness temperature.

Given that this procedure, worked well in removing the time-variable system gain for reference counts, it was generalized for the other MWR Rad_counts, namely: ant_counts and ant+noise_counts, which produced the "gain normalized Rad_counts" that would have been observed if the system gain was constant over the orbit. The generalized formula was:

$$C_{x\_norm} = C_{xi} \quad \frac{\left(< C_o > /(< T_o > + < T_{rec} >)\right)}{\left(C_{oi} / (T_{oi} + < T_{rec} >)\right)} \tag{3.4}$$

where C_{x_norm} are the normalized Rad_counts (i.e., ant, ant+noise, and ref) and C_{xi} are the instantaneous Rad_counts.

The next step in determining the MWR transfer function was to develop a model [13] for the system gain expressed as:

$$G_{rec} = G_o * g(T_o) * h(T_{in}) \tag{3.5}$$

where G_o is the mean of long term gain, $g(T_o)$ is the orbital gain changes due to the physical temperature, and $h(T_{in})$ is the gain compression due to variable scene brightness temperature. As a result, the instantaneous gain for a non-linear radiometer is different for each of the three Dicke states, and become:

$$G_{ant} = G_o * g(T_{ref}) * h(T_{in-ant}) \tag{3.6}$$

$$G_N = G_o * g(T_{ref}) * h(T_{in-N}) \tag{3.7}$$

$$G_{ref} = G_o * g(T_{ref}) * h(T_{in-ref}) \tag{3.8}$$

where G_{ant}, G_N and G_{ref} are the gains corresponding to the antenna, antenna + noise and reference states, and $T_{in\text{-}ant}$, $T_{in\text{-}N}$, and $T_{in\text{-}ref}$ are the receiver input temperatures, respectively.

To characterize the MWR system non-linearity, a deep-space calibration orbit was selected that included a wide range of scene Tb's including deep space (2.7 K), ocean (100 – 200 K), and land (300 K). After gain normalizing, a total power radiometer transfer function was constructed by performing a second order regression of the normalized Rad_counts versus the T_{in} for a single orbit. An example of this procedure for 37 GHz V-pol channel for one orbit is shown in Fig. 3.11, where the y-axis is the Rad_counts and the x-axis is the full dynamic range that includes $T_{in\text{-}ant}$ (Dicke switch in antenna position and noise diode is off) and $T_{in\text{-}N}$ (Dicke switch in antenna position and noise diode is on). The quadratic regression equation for this orbit is defined as:

$$Rad\_counts = -7.719*10^{-4} * T_{in}^{\ 2} + 16.61*T_{in} + 3272.9 \tag{3.9}$$

The existence of a negative quadratic term "$-7.719*10^{-4*}T_{in}^{\ 2}$" demonstrates that the system is non-linear and compressive. The normalized gain compression $h(T_{in})$ is set equal to the first derivative of (Eq. 3.9) after normalizing by the peak value, and a plot is shown in Fig. 3.12. From this figure, it can be seen that the normalized gain compression decreases with the increase of T_{in}, and the corresponding radiometer system non-linearity is about 4%.

One additional analysis was performed to demonstrate the MWR system non-linearity. In this approach the NDD (using gain normalized counts) was cross-correlated with the radiometer

input brightness temperature T_{in} in a scatter diagram (Fig. 3.13). After performing a linear regression, the NDD decreases monotonically with the increase of T_{in}, verifying that the MWR system gain is non-linear and compressive.

In conclusion, based upon the empirical on-orbit results presented herein, the MWR system is slightly non-linear (~4%), and as such accurate Tb's cannot be obtained. Therefore the development of a MWR non-linearity correction algorithm is presented in the next chapter.

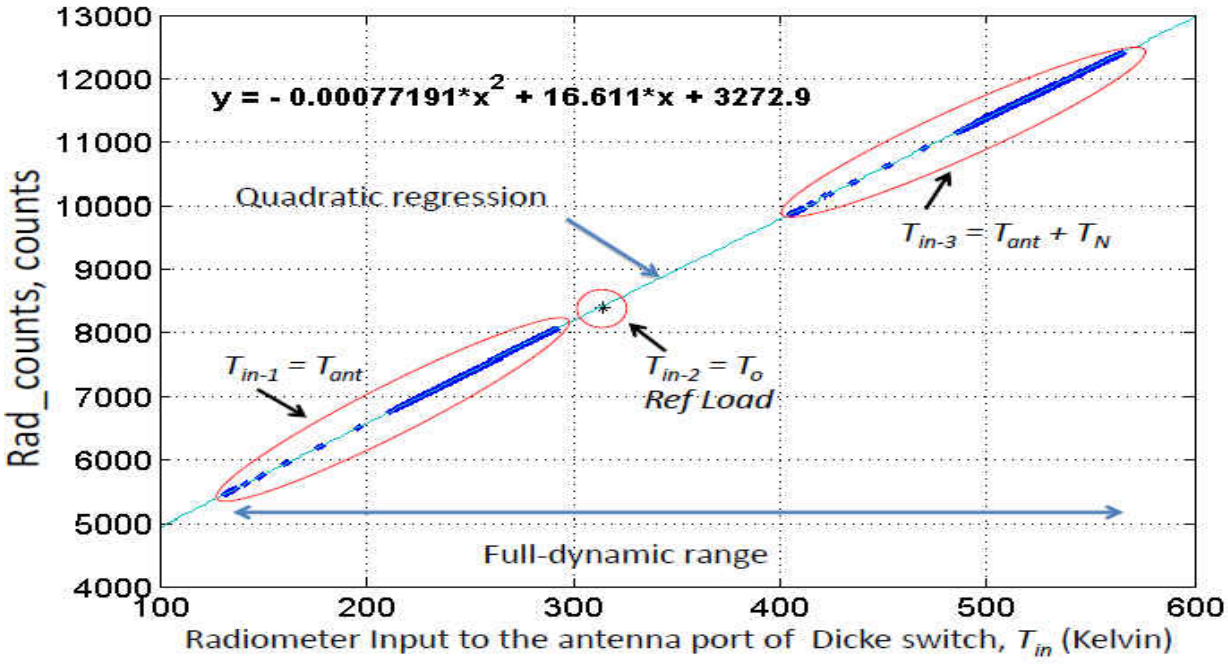

Figure 3-11 MWR Radiometer Transfer Function for 37V V5.0S (constant gain) for One Orbit

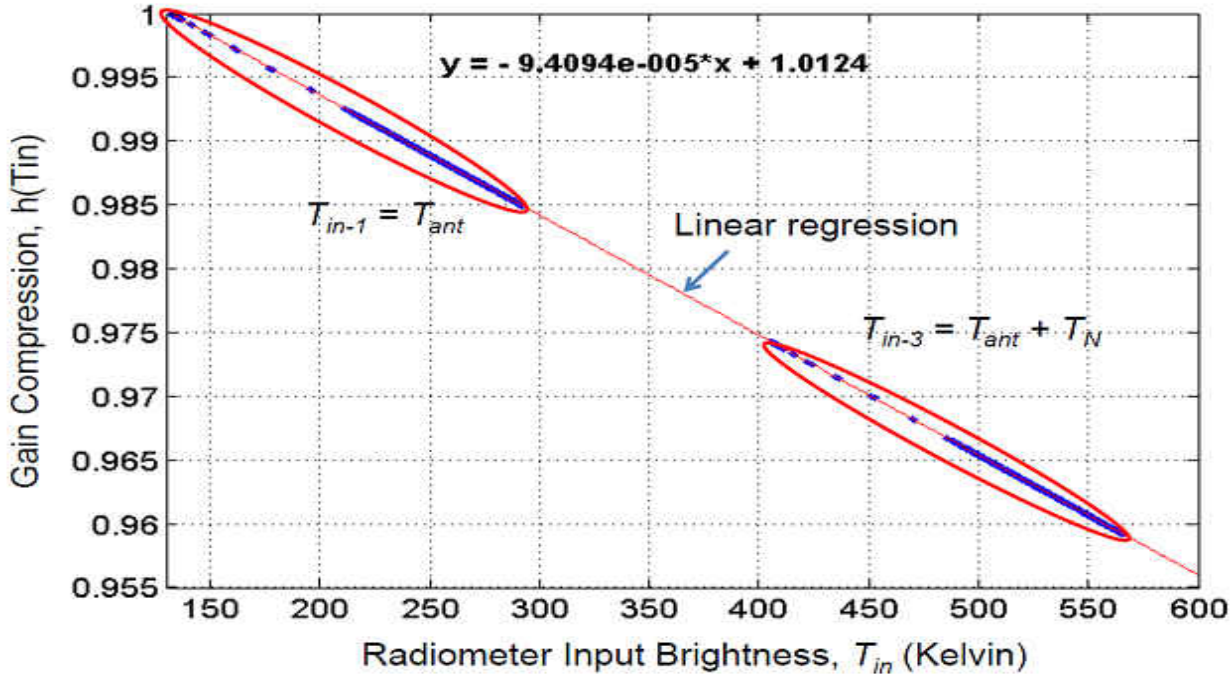

Figure 3-12 Normalized Radiometer Gain Compression "h(T_{in})".

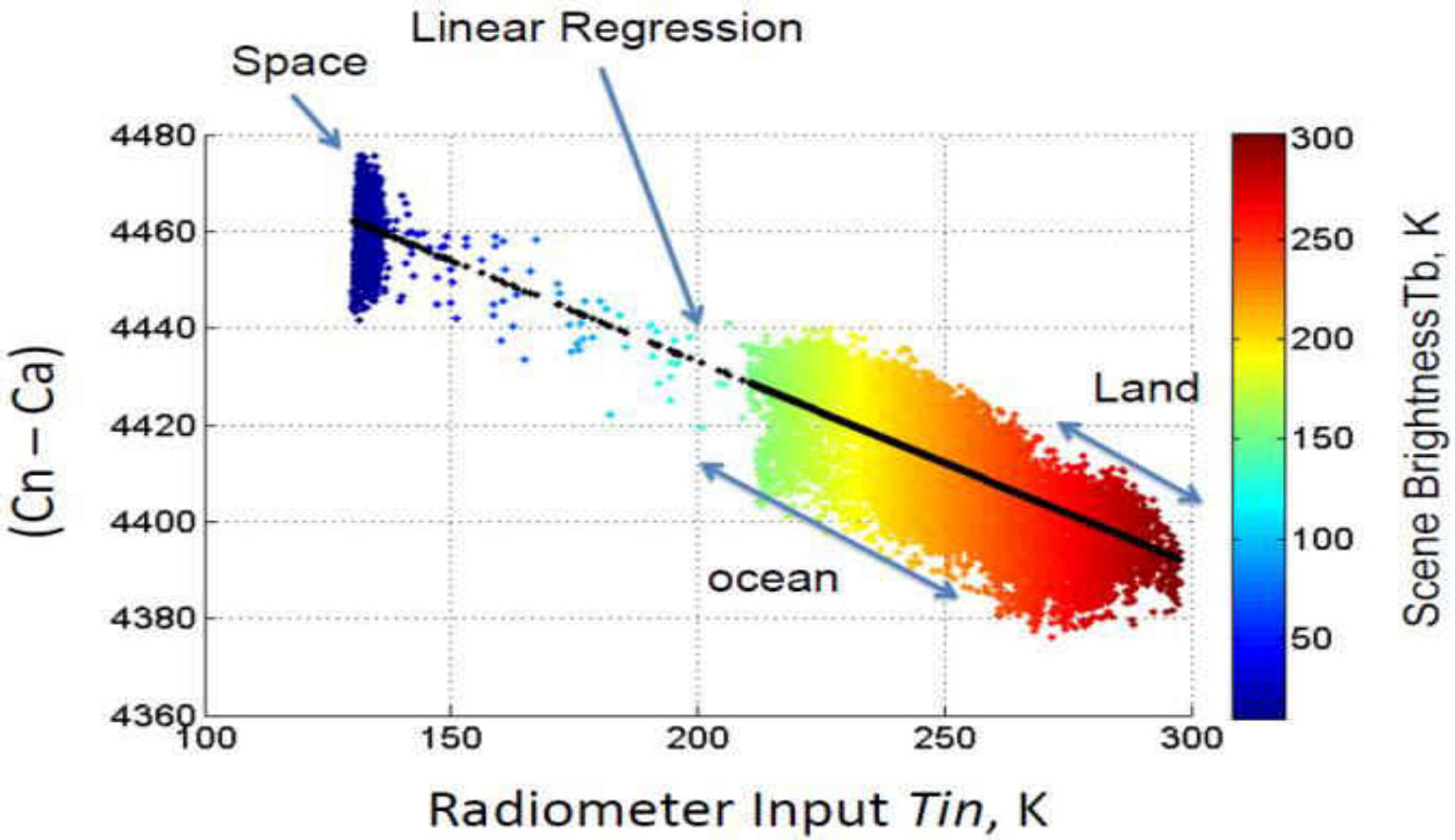

Figure 3-13 Noise diode deflection for MWR 37H radiometer after removing the time-varying component of gain change due to physical temperature. Color scale is the scene Tb.

CHAPTER 4
DEVELOPMENT OF COUNT-TO-TB ALGORITHM V6.0

The primary objective of this dissertation is to develop a new version (V6.0) of the MWR counts-to-Tb algorithm. This chapter describes the new algorithm, which corrects observed Tb anomalies for version V5.0S that includes the following new features: 1) a correction for system non-linearity, 2) a running average technique to reduce gain fluctuations, 3) a temperature correction for the noise diode injection noise, 4) and improved antenna switch matrix loss coefficients.

4.1 Radiometer System Non-Linearity Correction

As discussed in the previous chapter, the MWR transfer function was discovered to be slightly non-linear (compressive) during the on-orbit Cal/Val investigation [14]. While it is not possible to determine the root cause, it is most likely a deviation from square-law characteristic of the power detector. Regardless of the source, it is believed that the system non-linearity occurs in the receiver and is therefore common to all channels.

Initially the forward radiometer transfer function was obtained without gain normalization, and this approach proved to be unstable and ineffective in developing a procedure for consistently removing the system non-linearity for all orbits. On the other hand, by first gain-normalizing the counts, the non-linearity was successfully corrected for every orbit of the many evaluated. Thus, to establish a universal non-linearity correction procedure (rather than each orbit individually), seven “deep-space calibration orbits” that occurred during 2012 were

analyzed. These special radiometric calibration tests, which included deep space, ocean and land observations, provided a wide range of the brightness temperatures (from approximately 3 to 300 K). The analysis procedure was performed separately by channel (radiometer receiver) for each orbit and each beam; but because the nonlinearity was not orbit nor beam dependent, results for each channel were averaged. The analysis procedure for a single orbit is described next.

First, using smear corrected counts from V5.0S, the gain normalized Rad_counts (antenna - C_a, antenna + noise - C_N and reference load - C_o) were calculated using Eq. 3.2, and then the radiometer input temperature (T_{in}) was calculated using Eq. 2.6. Next the forward transfer function $Rad\_counts = f(T_{in})$ was established by performing a second-order least squares regression (see Fig. 4.1.a). It should be noted that a third order regression was also evaluated and rejected because the observed transfer function non-linearity was predominately second order. Also, because non-linear counts were used in V5.0S, the resulting T_{in} values were progressively too low. To evaluate the effect of this on the regression coefficients, an iterative procedure was used to recalculate the forward radiometer transfer function after correcting T_{in} for non-linearity. This experiment showed that there was only a minor change in the second-order term, and for simplicity this iterative approach was not followed.

To correct the radiometer system non-linearity, a procedure was developed to subtract the quadratic term from the Rad_counts. Because the eight beams of a given channel are sequentially integrated for 240 ms in the same receiver, a given beam was sampled every 1.92 s. Over this short interval, the mean radiometer gain should be effectively constant for all the beams. Furthermore, the gain-normalization procedure for Rad_counts adjusted the gain at each sampling period to be equal to the mean gain for the entire orbit; therefore, all beams should

have the same transfer function (i.e., slope and offset should be equal). Thus, the second order coefficients of the quadratic regression, derived for eight beams and seven deep space calibration orbits, were averaged and presented in Table 4.1.

Table 4-1 Mean and std of the second order coefficients for the three MWR Channels.

Channel	37V	37H	23H
Mean	$-7.46*10^{-4}$	$-6.90*10^{-4}$	$-2.17*10^{-4}$
STD	$2.35*10^{-5}$	$4.44*10^{-5}$	$8.91*10^{-6}$

Using these mean values, the instantaneous counts linearization equation for the three channels are:

for 37V

$$C_{x\_linear} = C_x - (-7.4677*10^{-4})*T_{in}^{\ 2} \tag{4.1}$$

For 37H

$$C_{x\_linear} = C_x - (-6.9064*10^{-4})*T_{in}^{\ 2} \tag{4.2}$$

for 23H

$$C_{x\_linear} = C_x - (-2.1708*10^{-4})*T_{in}^{\ 2} \tag{4.3}$$

where Cx represents antenna, antenna + noise and reference load, and Tin is the input brightness temperature to the Dicke switch (which is estimated using smear-corrected non-linear counts).

The performance of the non-linearity correction is illustrated in four different examples that follow. The first compares radiometer forward transfer functions in Fig. 4.1, where panel-a shows the transfer function before counts linearization and panel-b shows the same after counts linearization. In the left panel, the quadratic coefficient is 6.9×10^{-04}; and after the non-linearity correction (Fig. 4.1.b), the quadratic coefficient, reduced by a factor of > 500, becomes negligible.

The second example of the effectiveness of the counts linearization is presented in Fig. 4.2 as a global image of noise deflection for 37GHz V-pol for one day (~14 orbits), where panel-a is for V5.0S and panel-b is V6.0 (after linearization). Note that for V5.0S, the noise deflection counts changed abruptly at the ocean/land crossing boundaries, whenever the brightness temperature contrast was high. On the other hand, for V6.0 the noise deflection counts were independent of the scene Tb. Also note that as expected both images show slight latitudinal dependence of noise deflection due to the orbital receiver physical temperature cycle.

The third example shown in Fig. 4.3 presents a scatter diagram between the noise deflection counts and T_{in} for 37GHz V-pol for one deep space calibration orbit, where the color is the scene Tb. The left panel side (V5.0S) shows that the noise diode deflection depended on the input power; whereby increasing input T_{in} caused the deflection counts to monotonically decrease. In the right panel-b, after applying the non-linearity correction in V6.0, the deflection counts were independents of the input power.

Finally, the last example (Fig. 4.4) presents the time series of the radiometer gain, $(Cn - Ca)/Tn$, during one deep space calibration orbit. In the left panel (Fig. 4.4.a), as expected, the gain changed due to the orbital physical temperature cycle of the receiver; however

there were frequent anomalous gain jumps that are correlated with significant changes of the scene brightness temperature. Note the very large gain changes occurred when the scene changed from radiometrically hot land (red) to radiometrically cold space (blue). The performance of the MWR after non-linearity correction (V6.0) is shown in the right panel (Fig. 4.4.b). Here the gain varied cyclically over the orbit period because of the change of the receiver physical temperature; however there were no gain jumps with scene Tb changes.

.

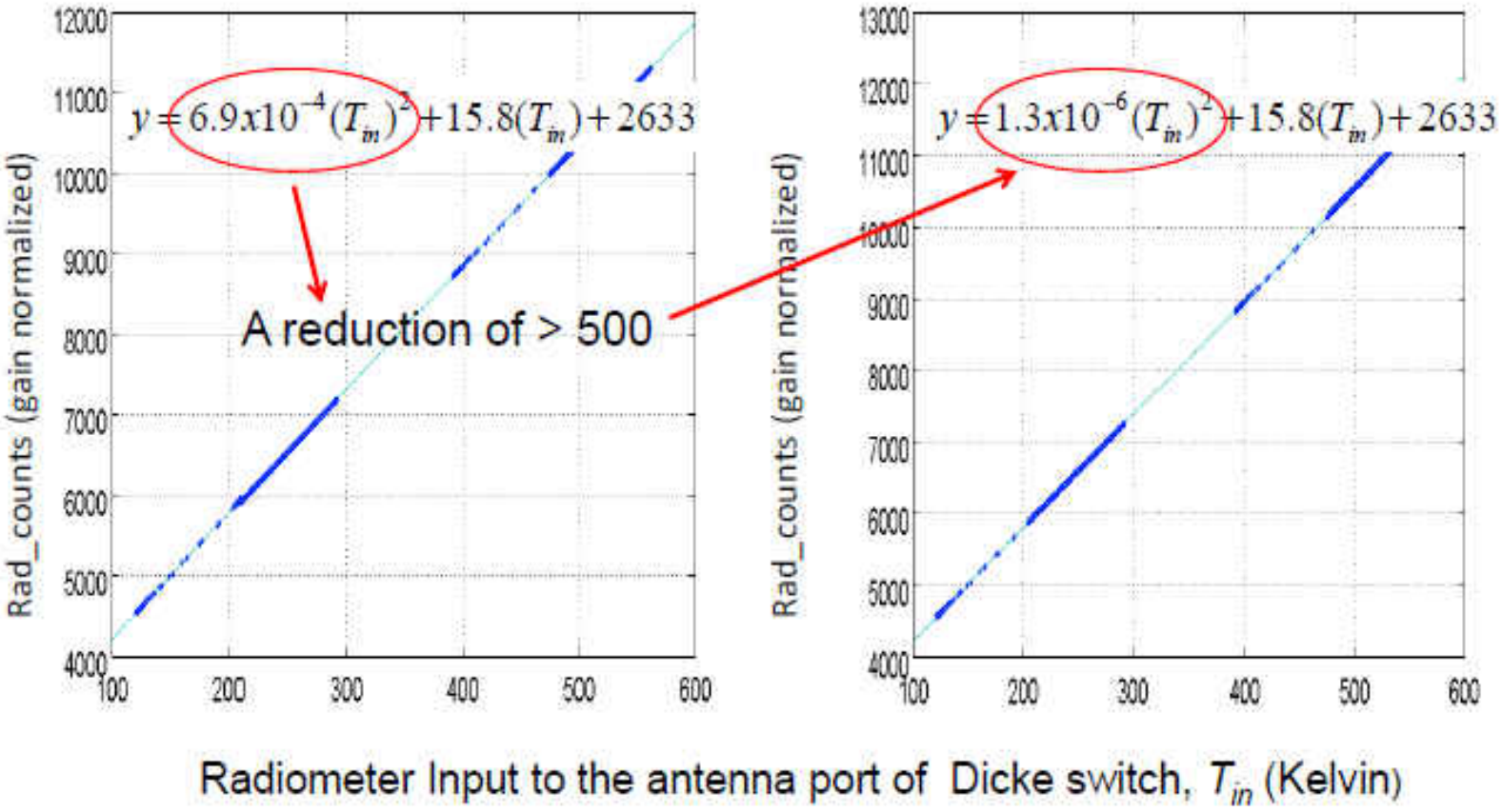

Figure 4-1 Radiometer transfer function that relates the Rad_counts to T_{in}: a) V5.0S (non-linear counts), b) V6.0S (linear counts).

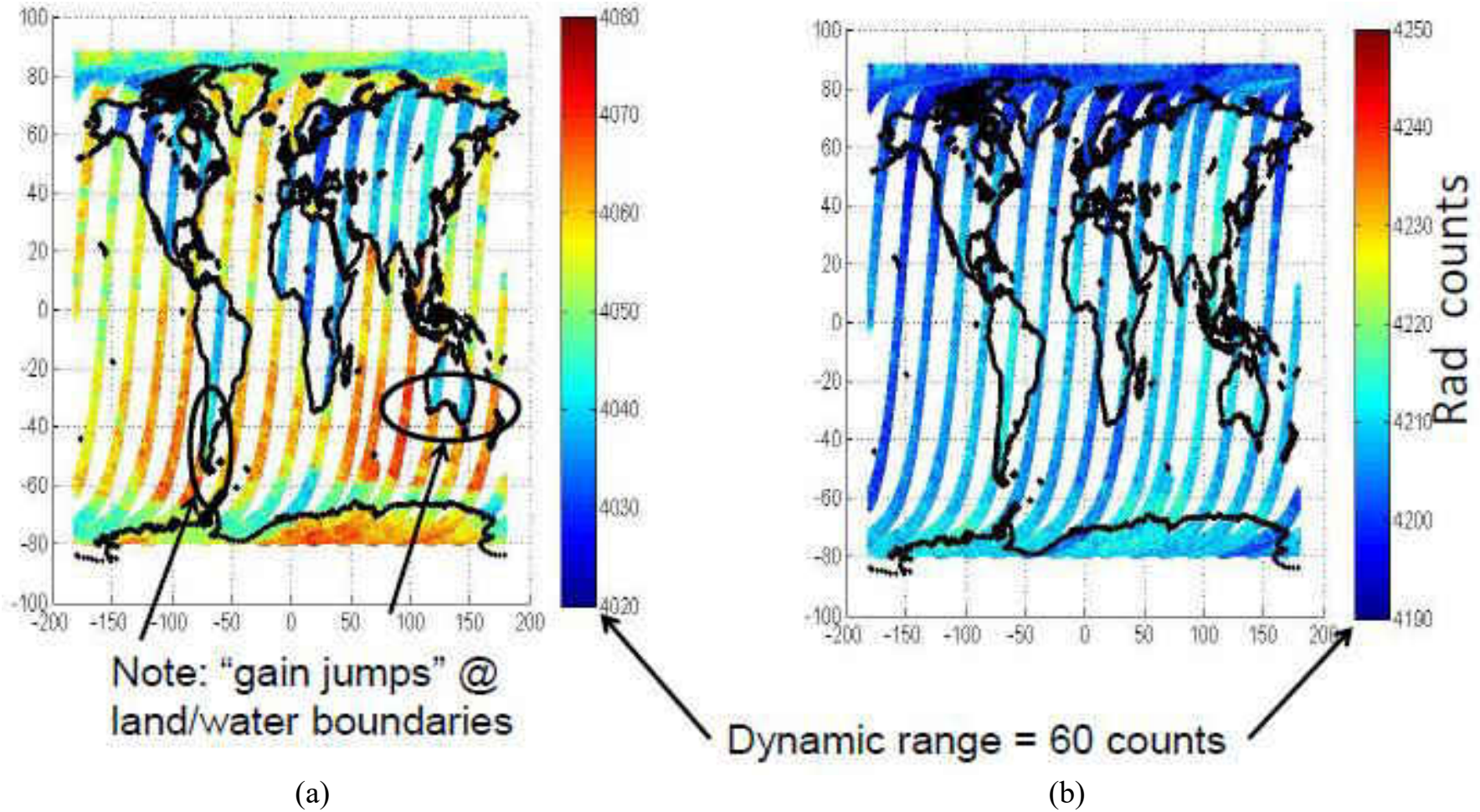

(a) (b)

Figure 4-2 On-orbit noise diode deflection (NOT gain normalized), descending passes for one day (All Beams) for 37GHz V-pol, a) non-linear counts from V5.0S, b) linear counts from V6.0. Note the color represents the noise diode deflection.

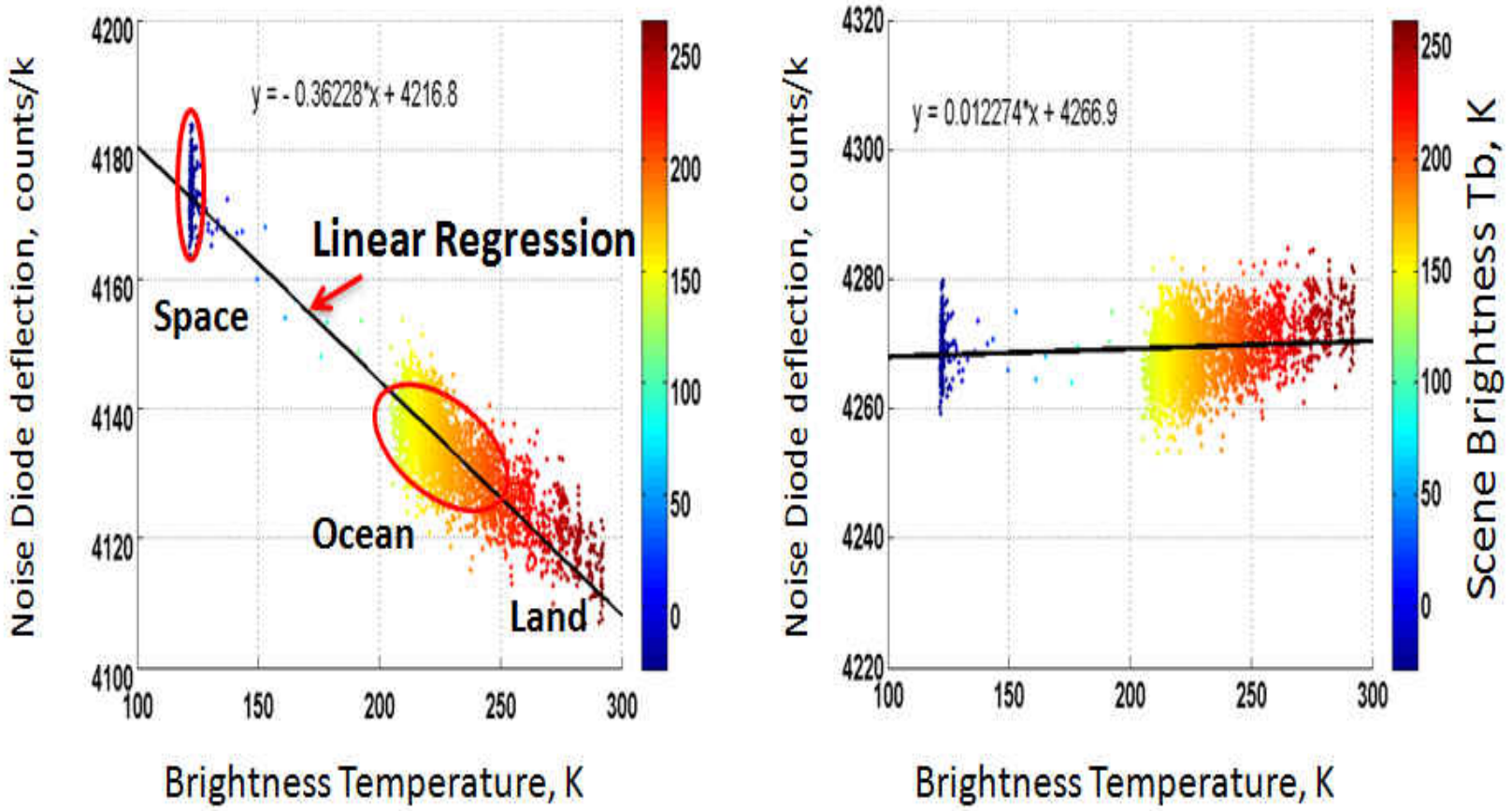

(a) (b)

Figure 4-3 Scatter diagram of the noise diode deflection vs. T_{in} for 37GHz V-pol; a) nonlinear counts from V5.0S, b) linear counts from V6.0. The color represents the scene brightness temperature, where the blue, yellow, and red colors are deep space, ocean, and land measurements respectively.

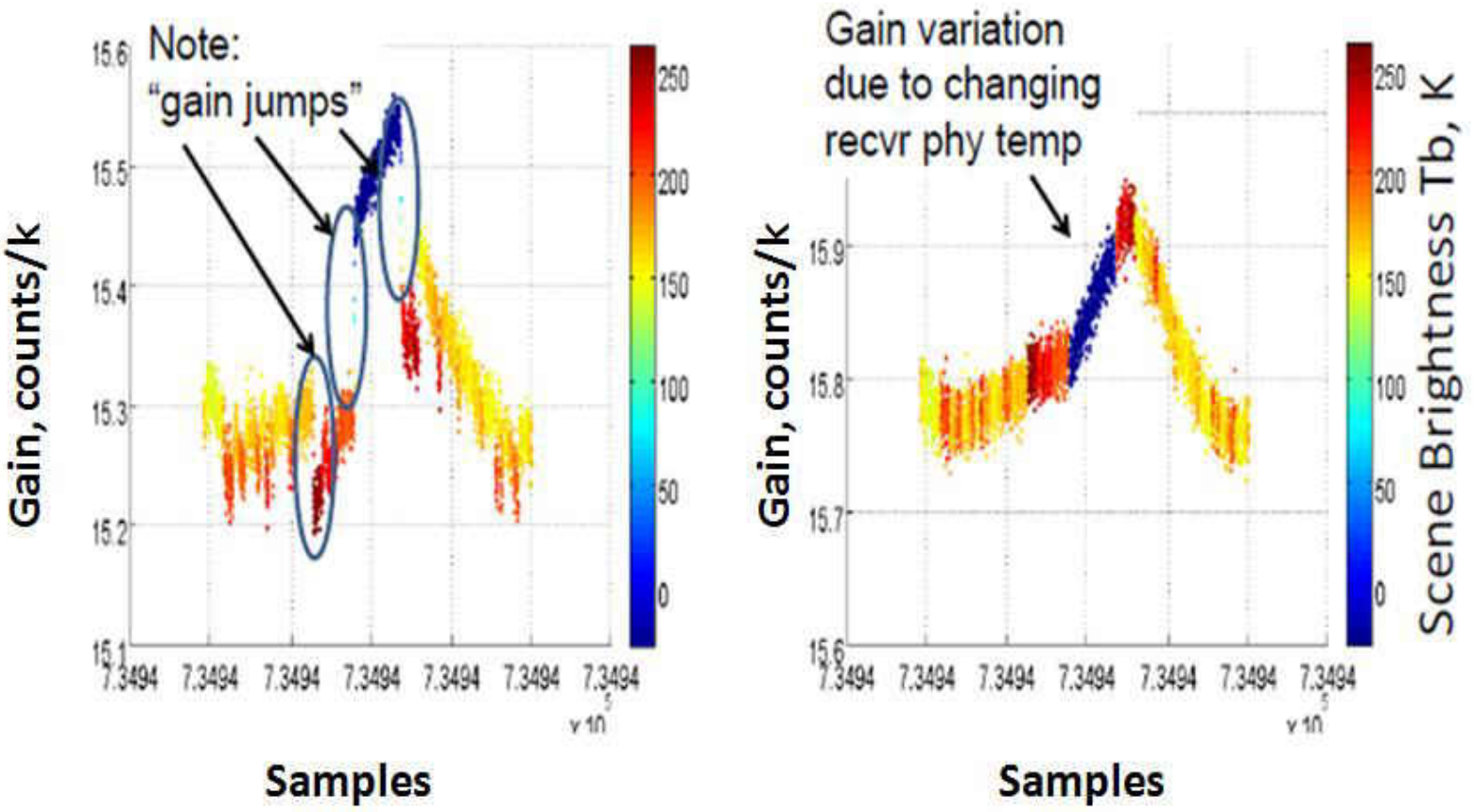

(a) (b)

Figure 4-4 Time series of the gain (*Cn*-*Ca*)/*Tn*. The color represents the scene brightness temperature for 37GHz H-pol, where the blue, yellow, and red colors are deep space, ocean, and land measurements respectively.

4.2 Running Average Technique

In the MWR, the Dicke radiometer state measurements (equations 2.2-2.4) are performed during a short period time (τ/3 = 80 ms for each state), during which the gain and offset are considered constant. By subtracting Eq. 2.2 from Eq. 2.3 and Eq. 2.4 from Eq.2.2 we can derive the radiometer's observable "R" parameter [3, 15], which, in the mean, is independent of radiometer parameters; system gain, receiver noise temperature and offset voltage:

$$R = \frac{Ca - Co}{Cn - Ca} \tag{4.4}$$

However, instantaneously the Rad_counts have independent random errors during the 3 Dicke states, which combine to yield the radiometric resolution (NEDT):

$$\Delta T = \sqrt{\frac{3}{B\tau}} * \left\{ (T_o + T_{rec})^2 + (T_{in} + T_{rec})^2 * (R-1)^2 + (T_{in} + T_n + T_{rec})^2 * R^2 \right\}^{\frac{1}{2}} \tag{4.5}$$

where *B* is bandwidth and

τ is the Tb integration time = 240 ms

The system gain changes inversely proportional to the receiver physical temperature, and to minimize this effect, the receiver baseplate temperature (T_o) is controlled on-orbit to within ± 0.5 K. In addition, Dicke radiometers mitigates the effect of radiometer receiver gain variation,

by rapidly switching the receiver input between antenna and internal reference noise sources (every 10 ms).

For the MWR receivers, the two noise references are: 1) a blackbody waveguide termination at ambient physical temperature and 2) a reverse-biased avalanche noise diode that produces an equivalent "hot" blackbody source. The Rad_counts are used in Eq. 2.5 to calculate the average system gain on each measurement period (240 ms); so that systemmatic gain changes, that occur on the sampling interval 1.92 s, will not produce Tb errors. However, since the individual counts have noise (NEDT), then the resulting calculated (estimated) gain will be corrupted with Gaussian noise. So the gain samples were passed through a recursive low-pass digital (smoothing) filter to reduce the associated gain fluctuations and provide an improved gain estimation for the calculation of T_{in}.

In the MWR counts-to-Tb algorithm V6.0, a triangular moving average is used to reduce the gain fluctuations, while maintaining the long-term gain tracking capability. The recursive filtering is defined by the equation:

$$gain\_smoothed = \sum_{j=-n}^{n} (gain_{i+j} * w_j) \tag{4.6}$$

where $j = -n,\ldots 0,\ldots,n$, and w_j are the gain weighting coefficients.

To cover the same number of samples of the smoothed gain as the original gain, the data at both ends of the vector is reflected and extended by half length of triangular window. The length of the window is selected, so that the long-term stability of the gain can be achieved while RMS noise in the gain estimation is reduced. This is determined by calculating the power

spectrum of the on-orbit gain and selecting the desired filter frequency response to remove white noise.

To perform this Fourier analysis, a time series of MWR calcuated gain for 8 beams from 15 orbits (one day) were combined to produce a series length of 441720 samples with the sampling period of 240 ms. An example of the power spectrum of the calculated gain for 37GHz V-pol is shown in Fig. 4.5. The desired signal is the low frequency portion of this spectrum, where there are 4 dominant spectral components corresponding to the fourier components of the orbital receiver temperature. The undesired signal is the high frequency white noise beyond a cutoff frequency of approximately 2.7×10^{-3} Hz, which corresponds to a digital filter window of 191 samples that has a triangular weighting applied and then a moving average taken. The corresponding triangular moving average window lengths for all channels are given in Table 4.2.

Table 4-2 Triangular moving average length for the three MWR channels.

Filter Window Length		
37V	37H	23H
191	151	191

From the normalized cumulative sum of the power spectrum of the gain (Fig. 4.6.a), it can be seen that the signal contained 90% of the white noise (dominant) and only 10% of the true signal. By applying the running average (Fig. 4.6.b), the noise contribution is reduced to 10%, and the true gain is increased to 90%.

The power spectra of the gain (green) and the smoothed gain (magenta) are illustrated in Fig. 4.7. The blue color represents the true gain, where the calculated gain and the smoothed gain

match. The 1/f value is also noted at the intersection of the black line and the red line (slope of the true gain). From this figure, it can also be noted that the white noise performance is reduced by about 20 dB while the true gain remained the same.

Figure 4.8 shows the time series of the gain (blue dots) and the smoothed gain (red line). From this figure, it can be seen that the high frequency fluctuations (white noise) are reduced, while keeping the low frequency fluctuations over an orbit (true gain).

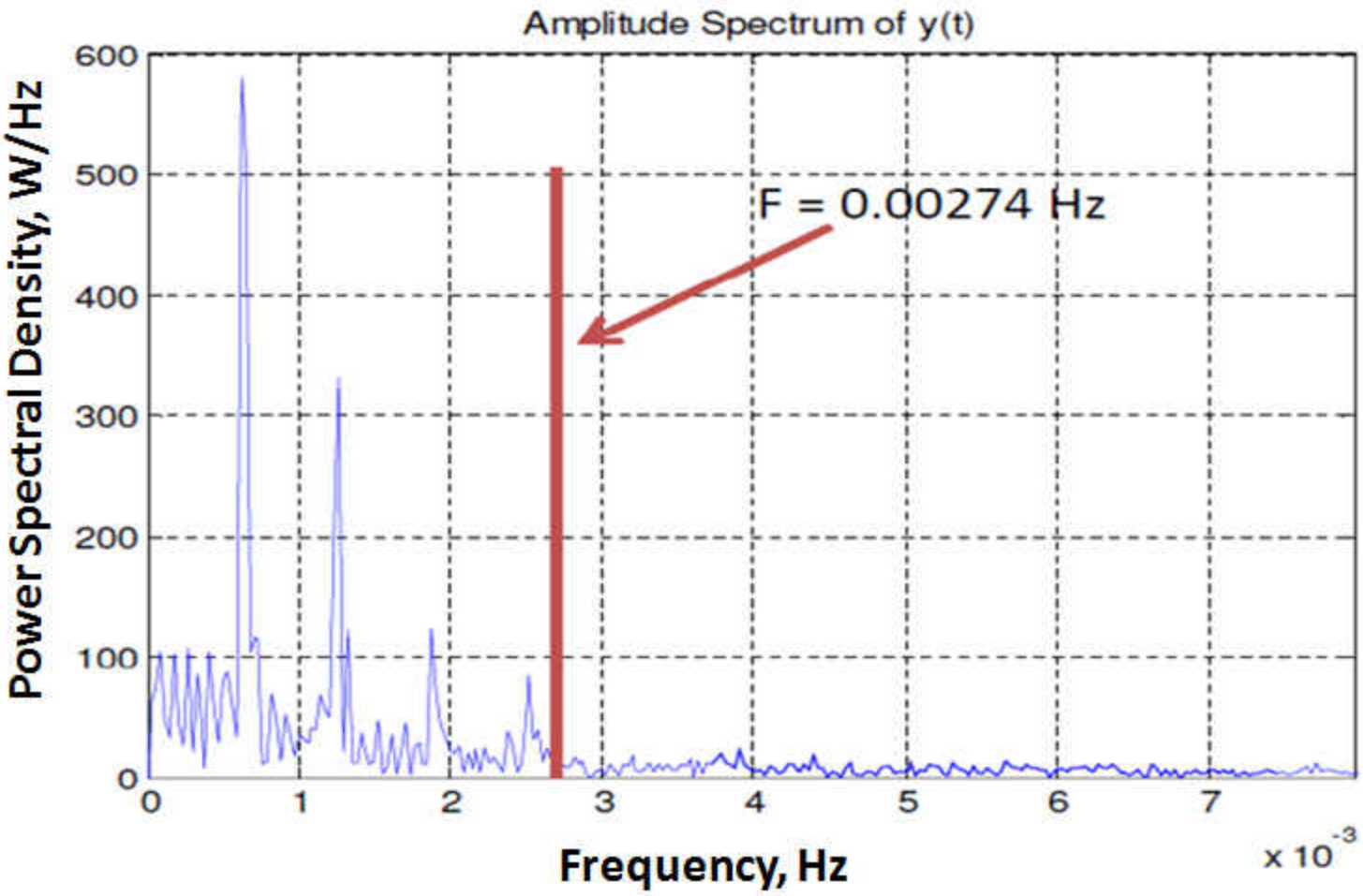

Figure 4-5 Amplitude Spectrum of the gain

.

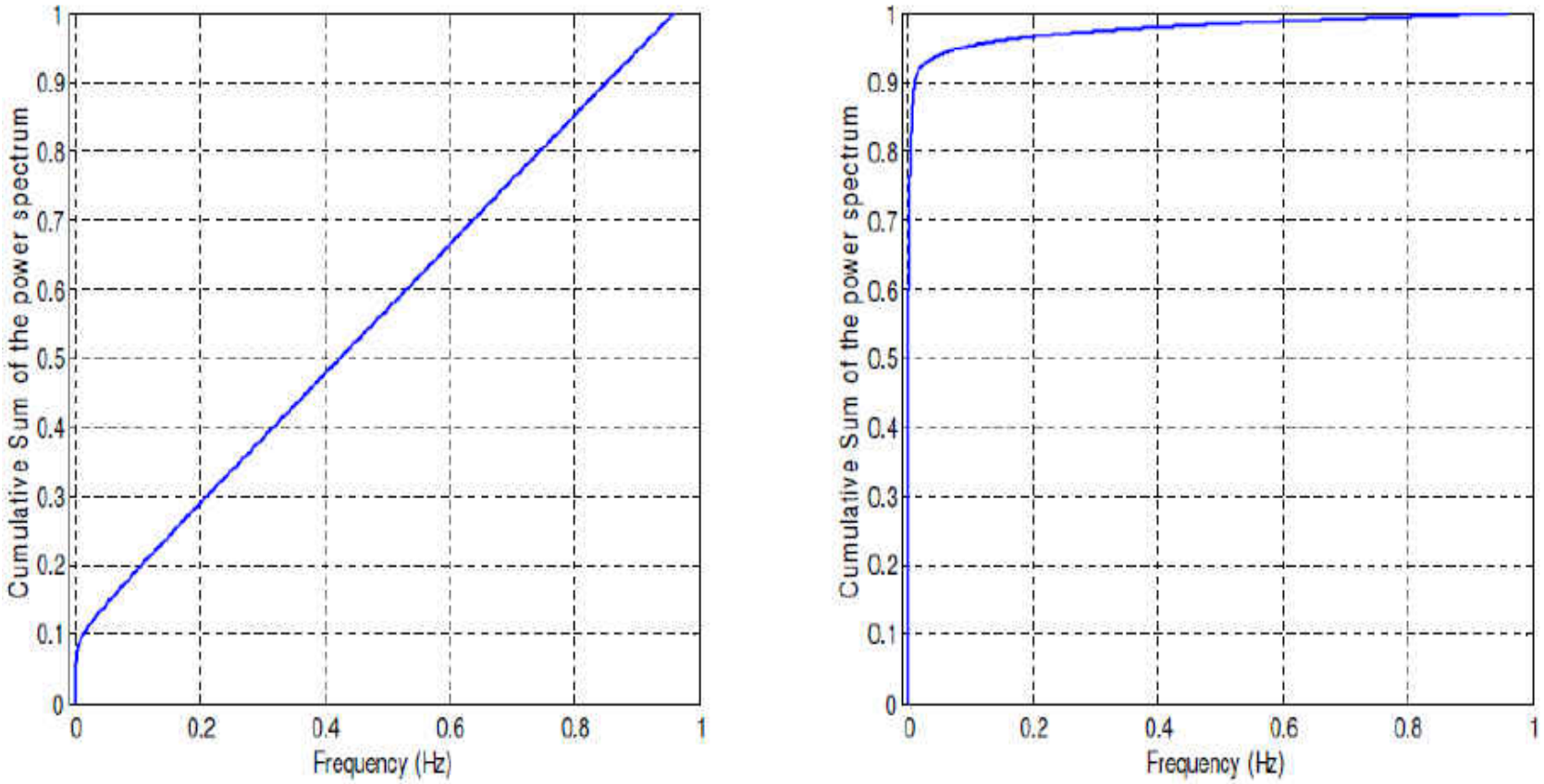

(a) (b)

Figure 4-6 Cumulative sum of the power spectrum of the gain (a) and Cumulative sum of the power spectrum of the smoothed gain (b).

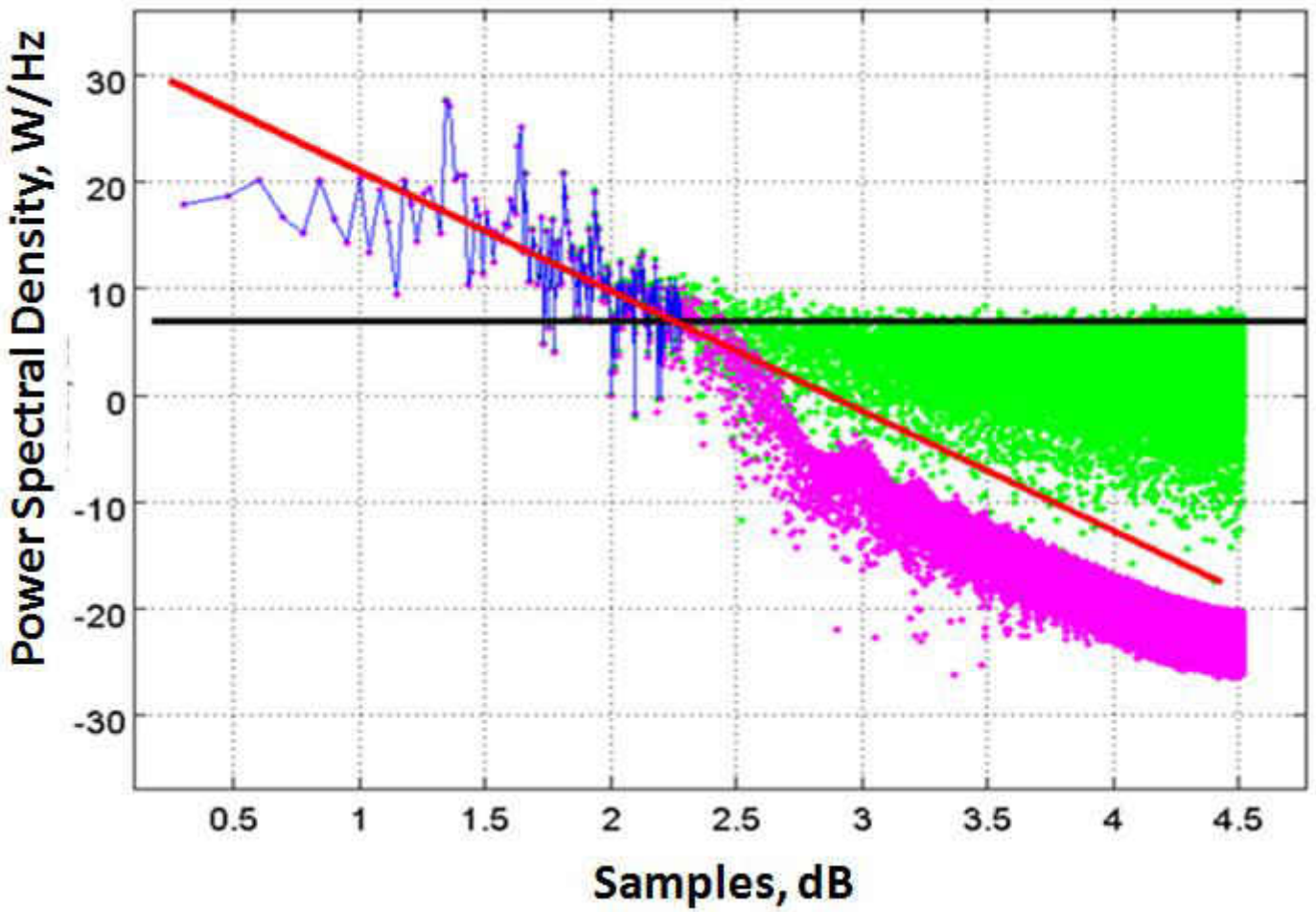

Figure 4-7 Power spectra of the gain (black), the smoothed gain (magenta), and the 191 samples of the power spectra of the gain (blue).

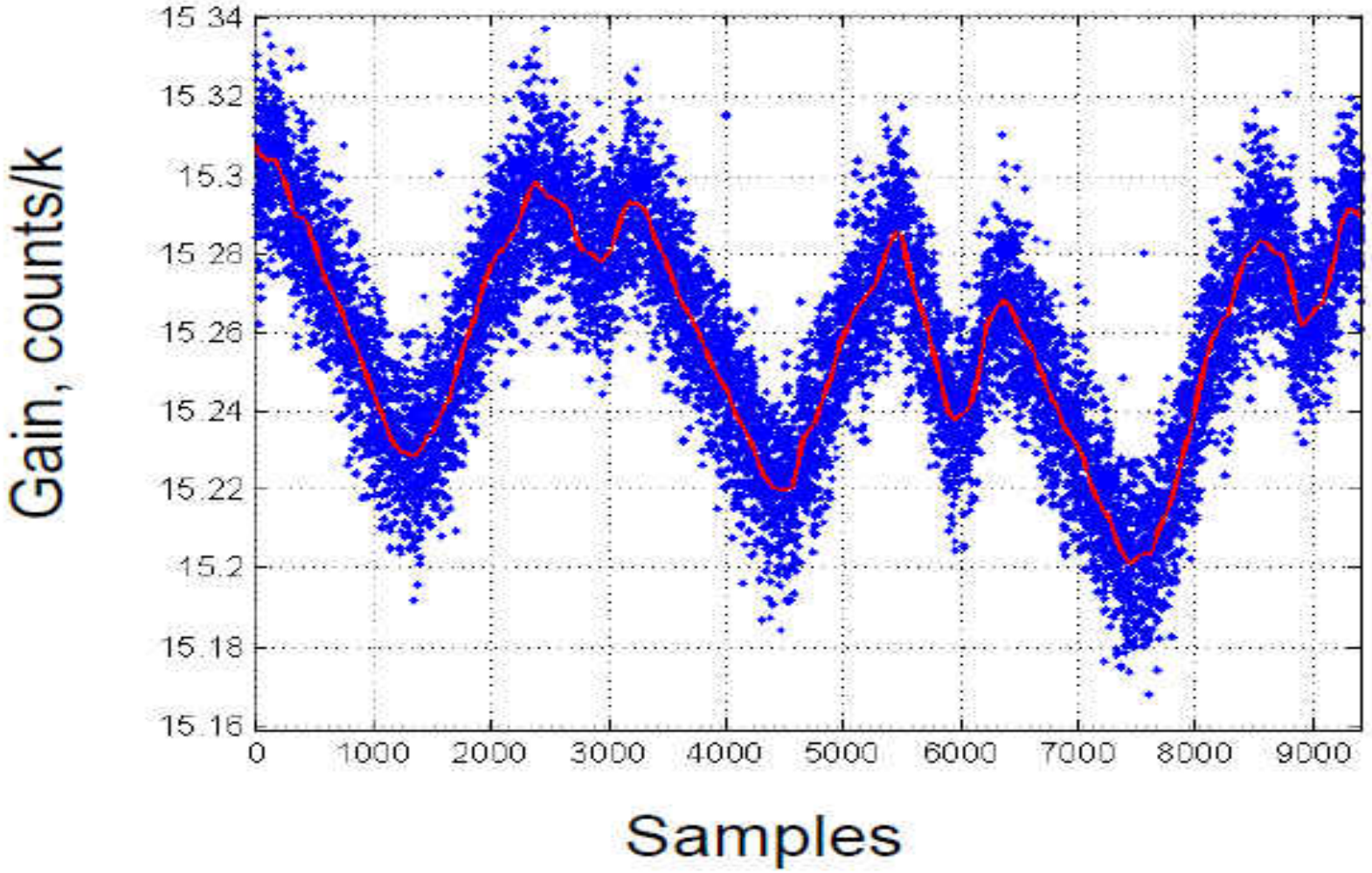

Figure 4-8 Time series of the gain (blue) and the smoothed gain (red).

4.3 Injected Noise Temperature Characterization

It is noted that the values of the injected noise temperature used in the counts to Tb algorithm versions 2.0 to 5.0S (derived by Biswas [7]) were from the pre-T/V test (see section 4.4); however, for the new version (V6.0), the noise diode injection noise (T_n), is characterized on a per orbit basis, using on-orbit data using the following procedure.

First, the rad_counts were linearized (to remove radiometer system non-linearity) and gain-normalized (to remove gain changes associated with the receiver physical temperature cycle). Next, a linear regression was performed, between the antenna counts (C_a) and the antenna temperature (T_{in}) to define the total power transfer function defined as:

$$C_a = slope * T_{in} + offset \tag{4.7}$$

Using the measured "antenna + noise" counts (C_n), the C_a was replaced by C_n and T_{in} (noise diode is off) replaced by "T_{in} + T_n" (noise diode is on). Solving for the noise diode injection noise yields:

$$T_n = (C_n - offset) / slope - T_{in} \tag{4.8}$$

A typical time series of the characterized T_n for 37 GHz V-pol for one orbit is illustrated in Fig. 4.9. It can be seen from this figure that T_n varies cyclically over an orbital period. Note that the changes of T_n over an orbit is typically 0.5 K peak-to-peak.

After collecting one year of data, the mean T_n was characterized as a function of the reference load (baseplate) physical temperature (T_o). An example of this characterization is shown in Fig. 4.9 for 37 GHz V-pol over the period Jan-Nov, 2013. After removing the outliers, a linear regression was performed to derive the injected noise temperature for 37 GHz V-pol as:

$$T_n = 0.45107 * T_o + 145.59 \tag{4.9}$$

Similar analyses were performed for 37 GHz H-pol and 23 GHz H-pol are:

for 37 GHz H-pol :

$$T_n = 0.03974 * T_o + 259.05 \tag{4.10}$$

for 23 GHz H-pol:

$$T_n = 0.14598 * T_o + 346.85 \tag{4.11}$$

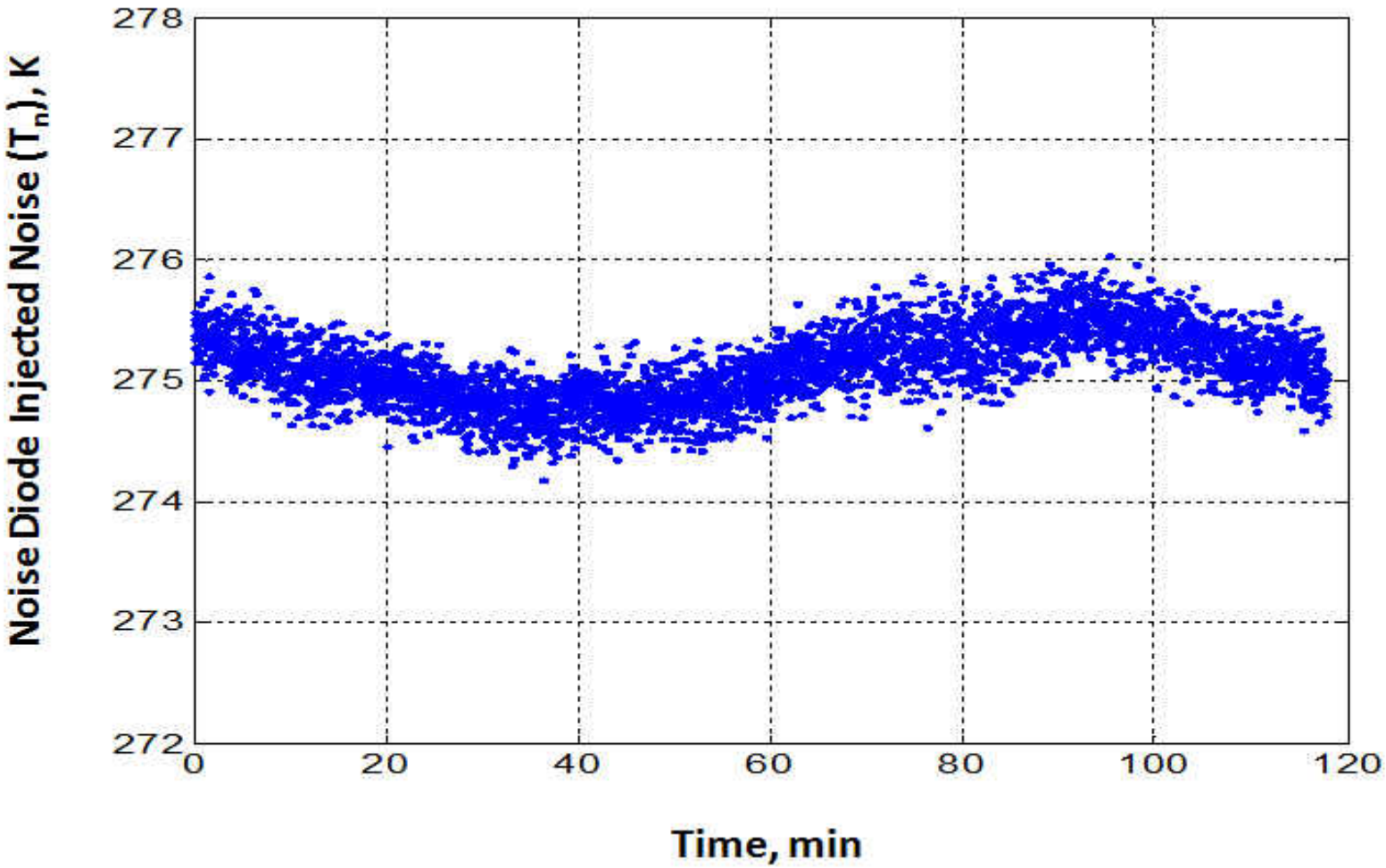

Figure 4-9 Typical time series of the noise diode injection noise characterized using on-orbit data.

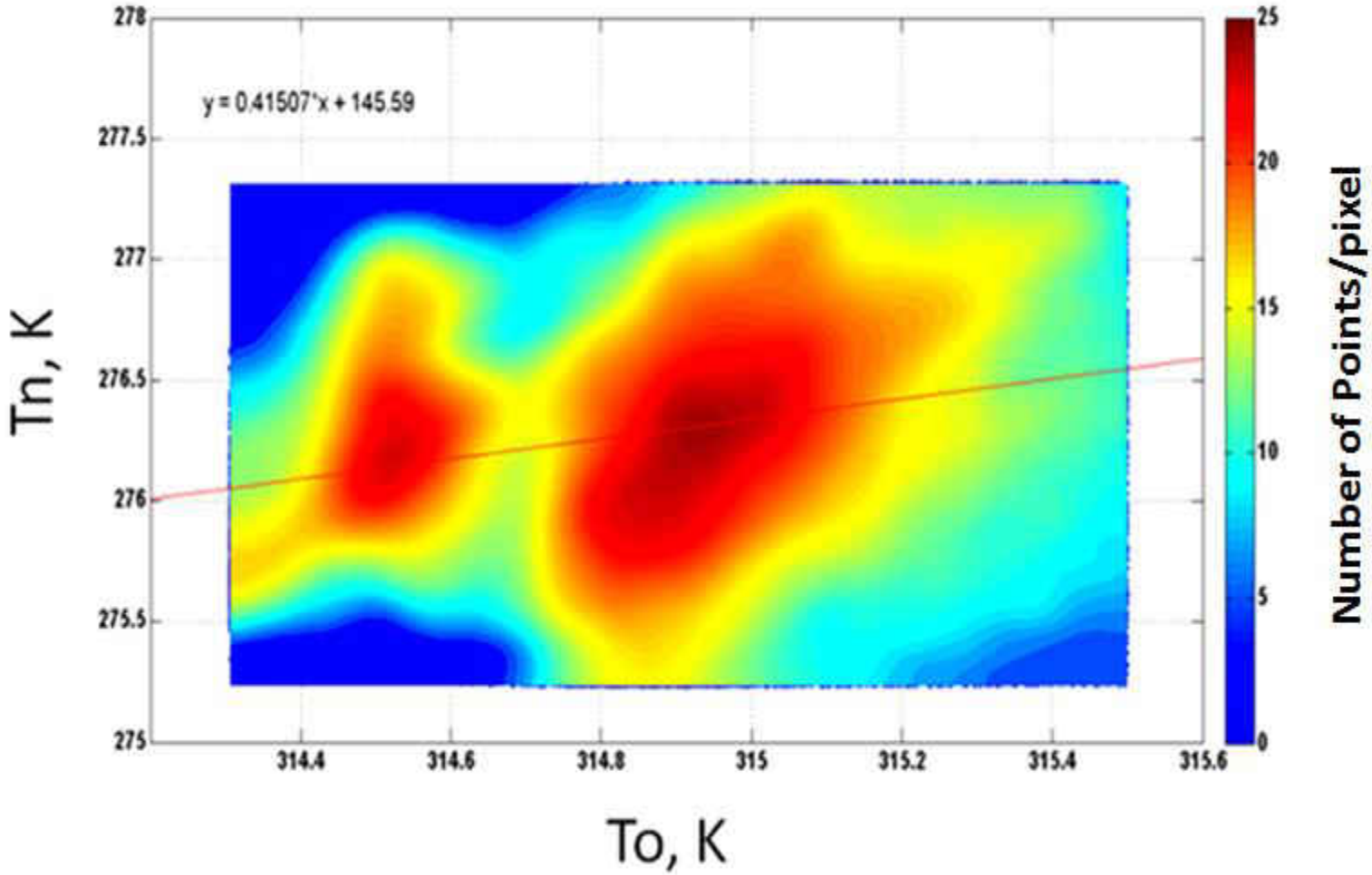

Figure 4-10 Scatter diagram between noise diode injection noise (T_n) and reference load temperature (T_o). The colors represent number of points.

4.4 Improved Antenna Switch Matrix Loss Coefficients and Injected Noise Temperature Validation

The original analysis of the pre-launch radiometric calibration tests (Biswas [7]) were performed before implementing the MWR non-linearity correction; therefore these tests were reanalyzed using linear counts with the objective of: 1) verification of the noise diode injected noise temperature, and 2) deriving improved antenna switch matrix (ASM) loss coefficients.

4.4.1 Pre Thermal Vacuum Calibration Test

The objective of the pre-T/V calibration test was to determine the injected noise temperature, T_n for the three MWR channels. During this test, the ASM's were removed and were replaced by a blackbody waveguide termination located at the calibration reference point (input to the directional coupler), as shown in Fig. 4.11. Thus, the blackbody brightness temperatre was equal to the measured physical temperature of the termination, which was sequently heated and then cooled using hot water and liquid nitrogen respectively to create the two temperature sources, hot load 'T_h' and cold load 'T_c'. After propagating through the dissipative loss of the inter-connecting test waveguide to the directional coupler input, the Tb's were modified as shown in Fig. 4.11.

During the test, the receiver was maintained at constant temperature (T_o) by the MWR thermal control subsystem, As shown in the Fig. 4.12, there was a small drift of ± 0.04 K about the mean during the interval of the test (~ 2 hours); so the resulting gain normalization of counts was negligible. After collecting counts for the hot and cold loads, the raw (non-linearized) counts

were used to estabilsh a corresponding total power radiometer transfer function as shown in Fig. 4.13a for 37 GHz V-pol, where the known brightness references were: cold load, reference, and hot load. The noise diode injected noise (T_n) in this analysis was obtained from the previous version V5.0S of MWR counts to Tb algorithm, where it was assumed to be constant (T_n = 274 for 37GHz V-pol). Finally a second-order regression was performed, and the counts were linearized (see section 3.4) by subtracting the quadratic term. For the 37 GHz V-pol the relationship is:

$$C_{x\_linear} = C_x - (-0.001121) * T_{in}^{\,2} \tag{4.10}$$

where C_x are the non-linear counts that represent: cold load (C_c), hot load (C_h), reference (C_o), cold load + noise (C_{c+n}) and hot load + noise (C_{h+n}) counts, and Tin represents the corresponding input brightness temperatures.

The effectiveness of the non-linearity correction was assessed in two ways. The first is shown in Fig. 4.13.b, where the radiometer transfer function is confirmed to be linear, when using the linearized rad_counts. Based upon the quadratic polynomial fit, the non-linearity (second order term) is reduced to a negligible value (4.0492×10^{-8}).

The second method of assessing the effectiveness of the non-linearity correction is concerning the measurment of the noise diode injected noise temperature at the hot and cold end of the brightness temperature scale. For this analysis, we use a linear total power transfer function (slope and offset) for V5.0S (non-linear counts) and V6.0 (linearized counts) to

calculate the brighness temperature for the "cold load + noise" (T_{c+n}) and "hot load + noise" (T_{c+n}) given as:

$$T_{c+n} = (C_{c+n} - offset) / slope \tag{4.11}$$

$$T_{h+n} = (C_{h+n} - offset) / slope \tag{4.12}$$

By subtracting these equations, the noise diode injection noise T_n is:

for the cold load

$$(T_n)_{cold} = T_{c+n} \quad T_c \tag{4.13}$$

for the hot load

$$(T_n)_{hot} = T_{h+n} \quad T_h \tag{4.14}$$

The time series of T_n are shown for V5.0S in Fig. 1.15a and V6.0 shown in Fig. 4.15.b. In Fig. 4.15.a, because of the radiometer system non-linearity, T_n = 265 K for the hot load, while T_n = 272 K for the cold load. Obviously this is anomalous because the noise diode injected noise temperature is constant.

In Fig. 4.15b, after the non-linearity correction, the T_n for both test are ~273 K, as it was expected. Thus, it is concluded that the T_n in V6.0 does not depends on the scene Tb's and depends only on the noise doide physical temperature. Because the pre-T/V calibration test was conducted only at one reference load temperature, it is not possible to extrapolate the results to other physical temperatures experienced on-orbit. Thus, in the new version of counts to Tb algorithm V6.0, we decided to use the T_n values determined on an orbit by orbit basis as presented in sectiom 4.3., Eq. 4.8.

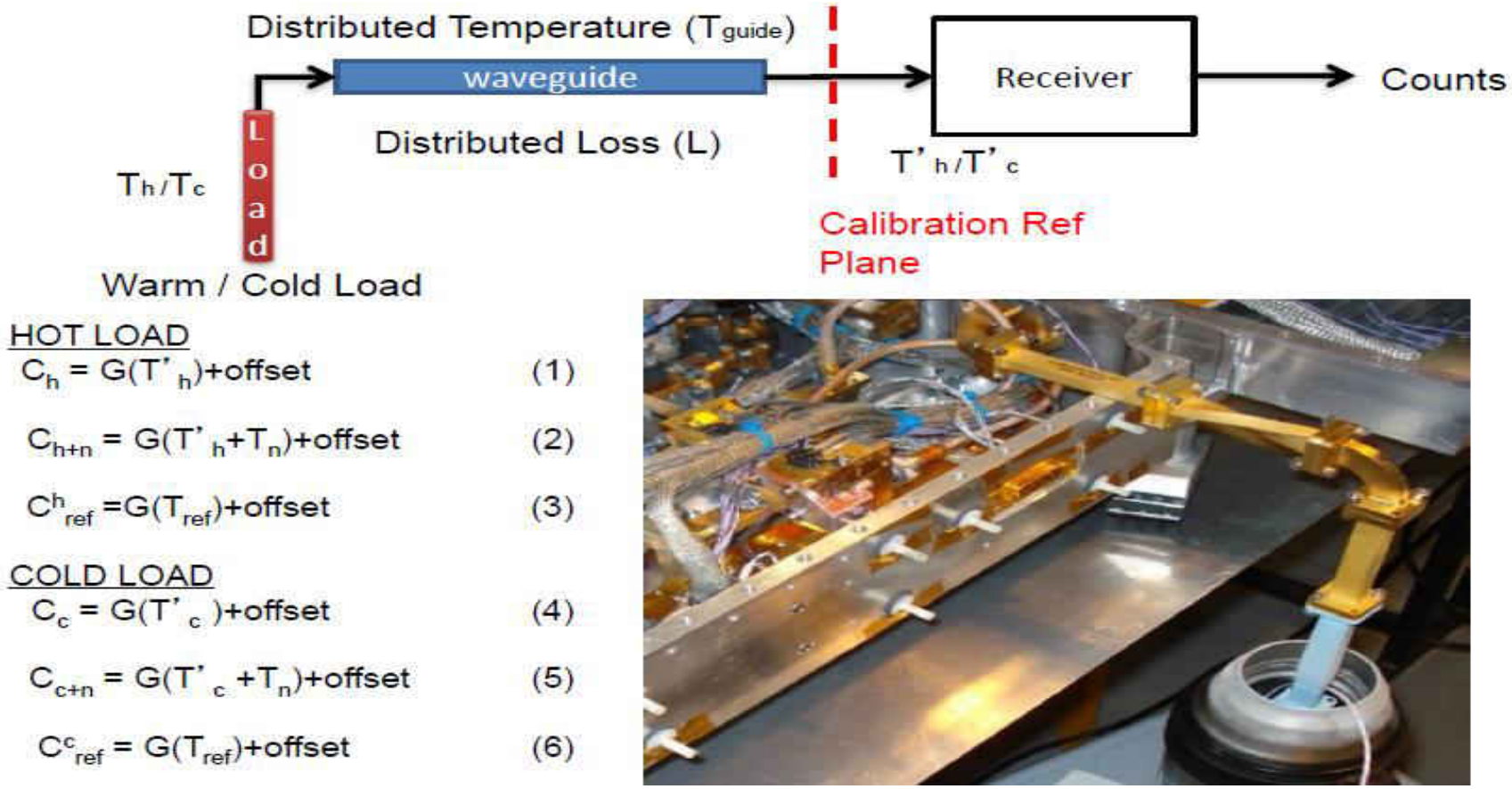

Figure 4-11 Pre-T/V calibration test. The matched termination (blue in the bottom picture) is heated and cooled to create T_h and T_c. The temperatures are measured using a platinum temperature sensor attached to the termination. The receiver and the termination are connected through the calibration waveguide. The equations are the three Dicke state for HOT and COLD cases.

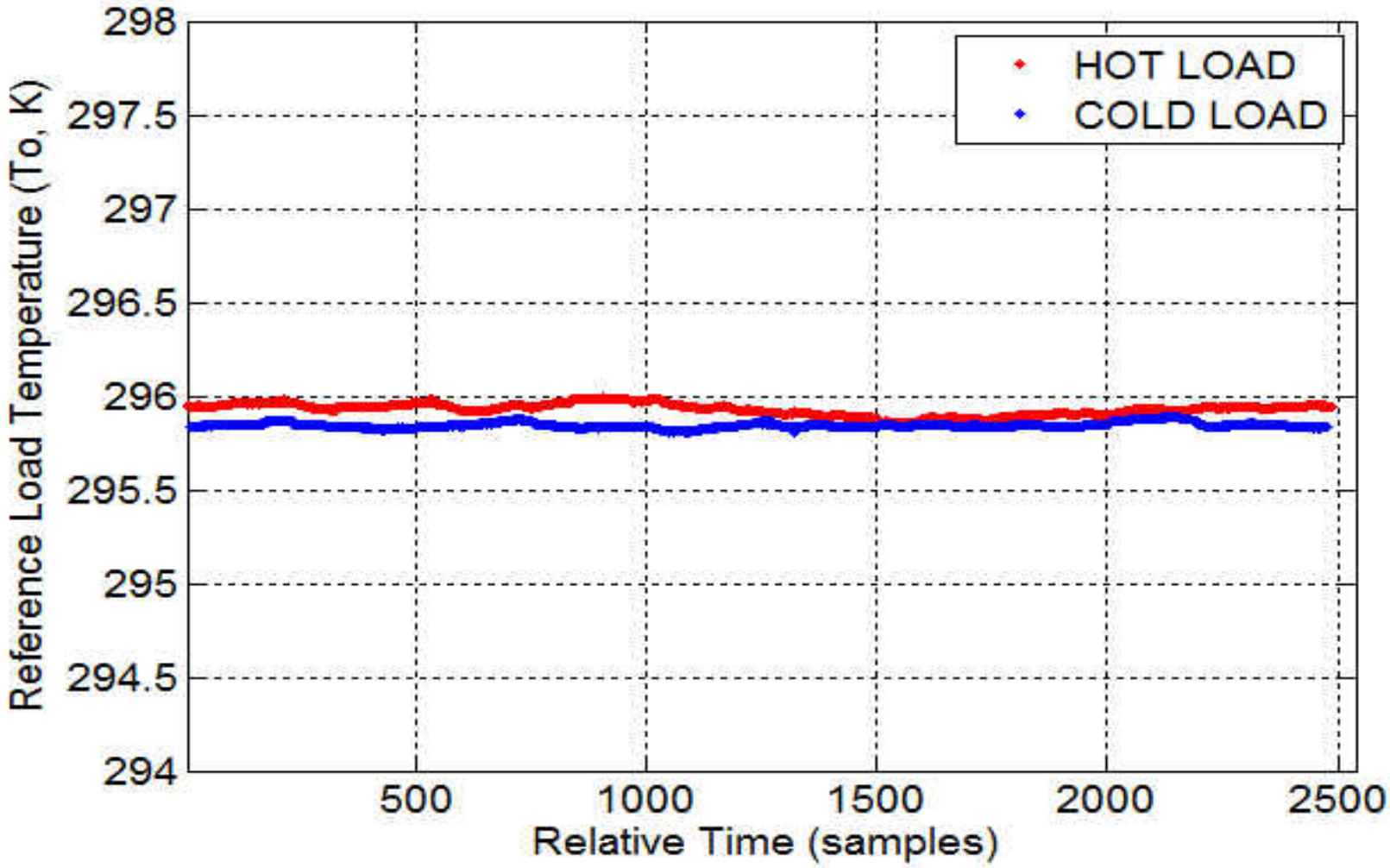

Figure 4-12 Time series of the reference load temperature for hot load (red dots) and cold load (blue dots) tests for 37GHz V-pol.

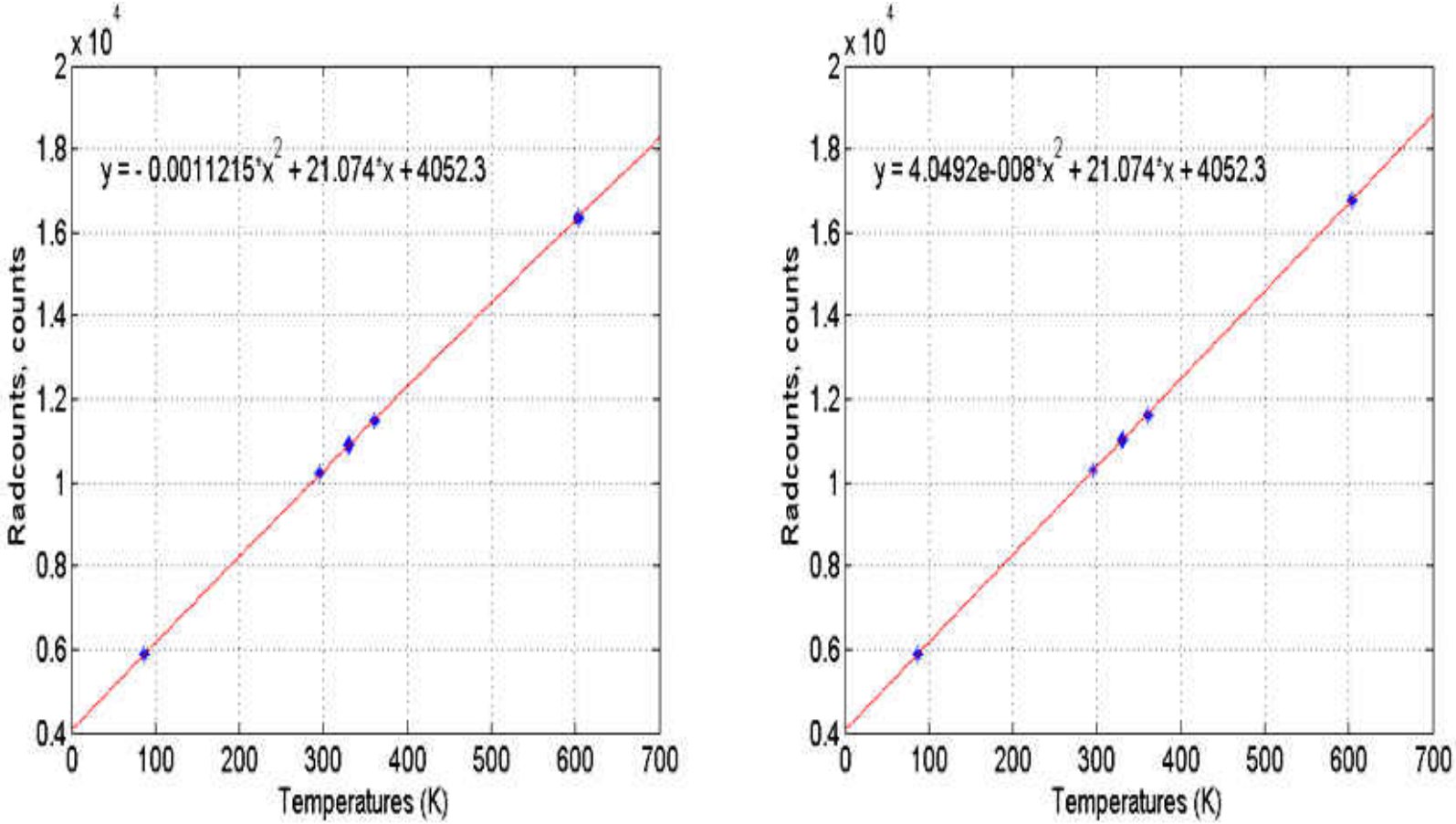

(a) (b)

Figure 4-13 Radiometer transfer function: a) before non-linearity correction, b) after non-linearity correction

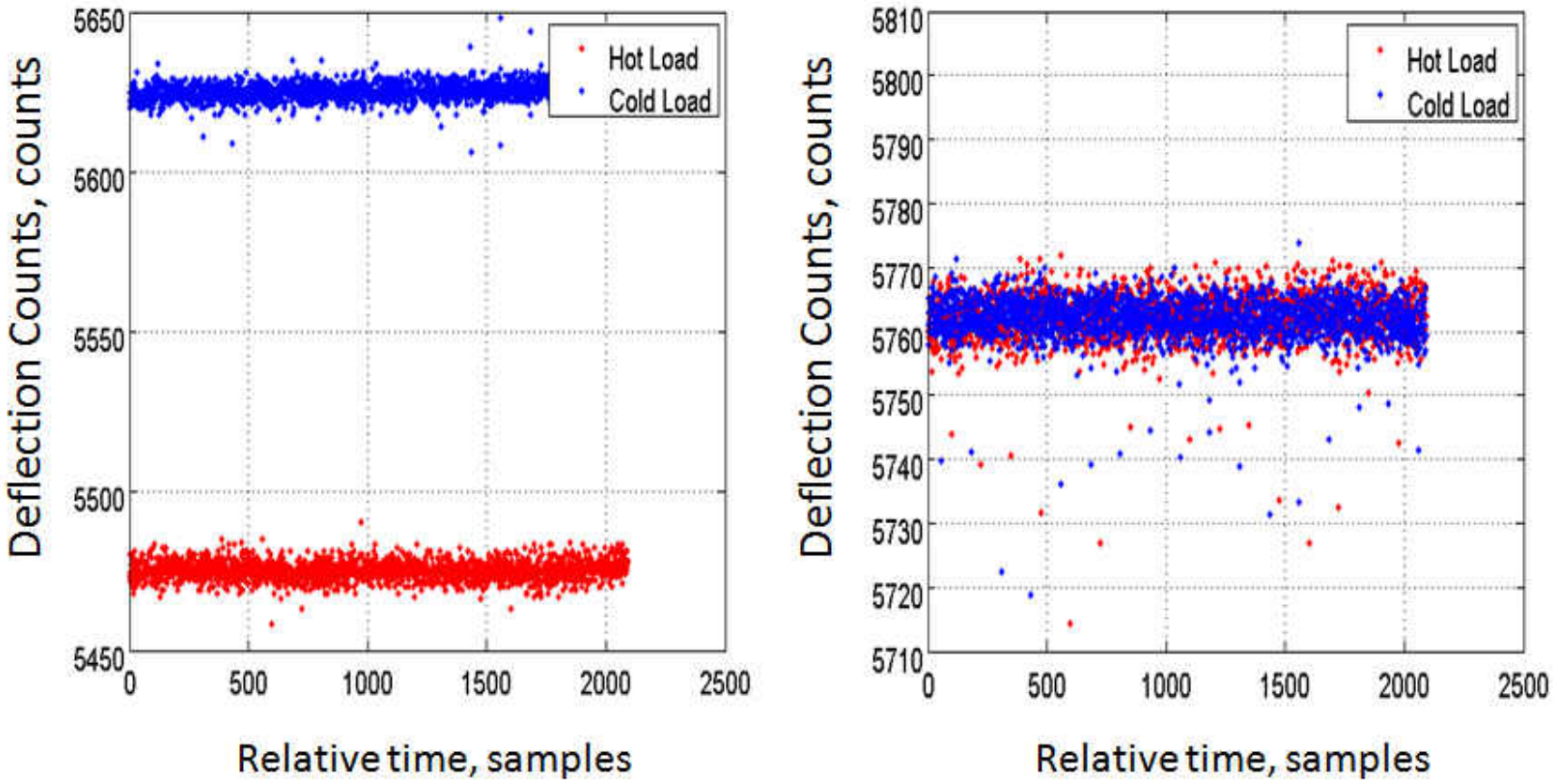

(a) (b)

Figure 4-14 Noise diode deflection (deflection counts) for 37GHz V-pol for: a) V5.0S using non-linear counts, b) V6.0 using linear counts.

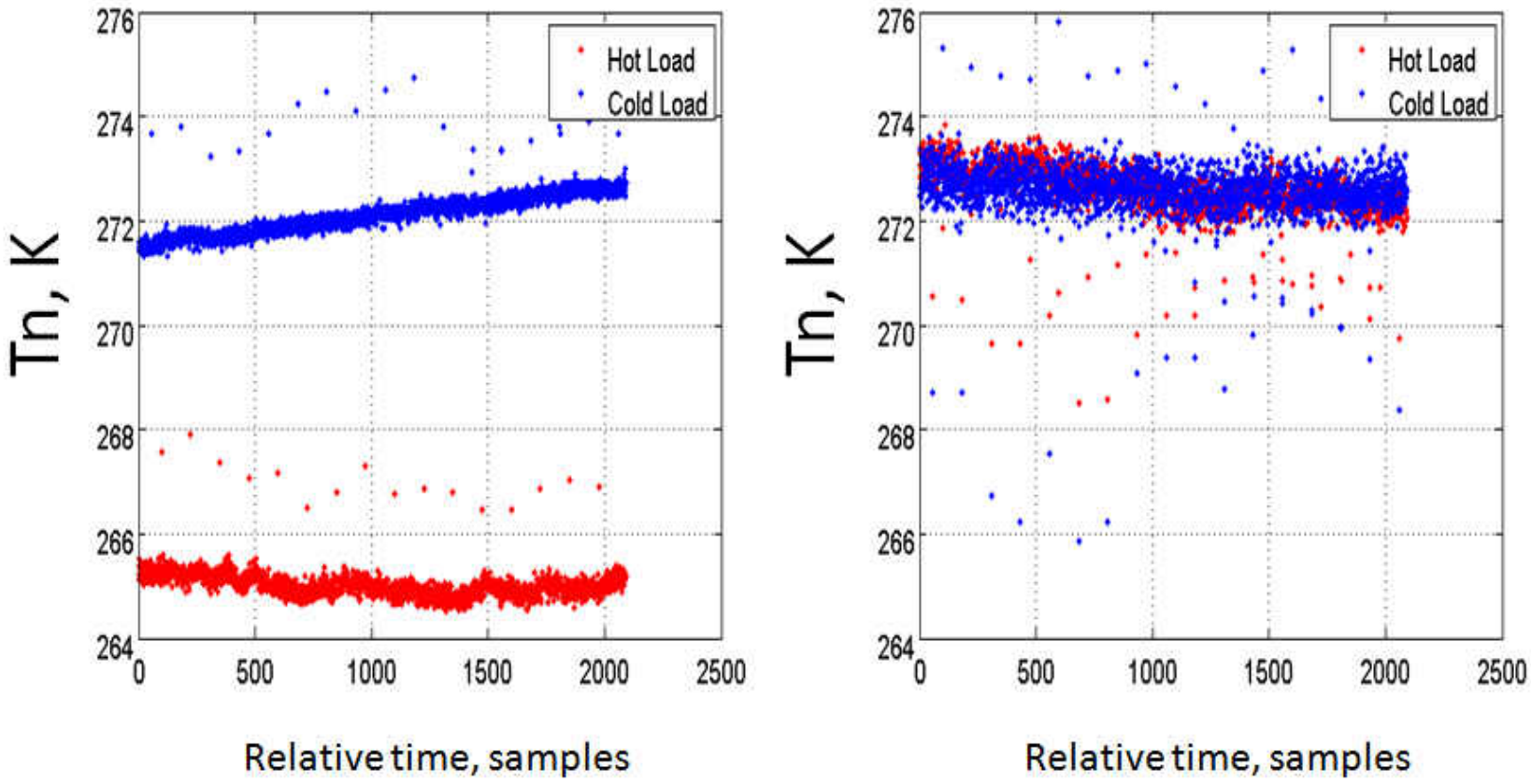

Figure 4-15 Noise diode injection noise for 37GHz V-pol : a) V5.0S using non-linear counts, b) V6.0 using linear counts.

4.4.2 Thermal Vacuum Calibration Test

The primary objective of the pre-launch MWR Thermal Vacuum (T/V) Calibration Test was to perform MWR radiometric calibration under simulated on-orbit conditions and thereby develop a forward radiometer transfer function that related apparent brightness temperature input at the antenna feed aperture to Rad_counts in the instrument science data output. A necessary part of this objective was to empirically derive the antenna switch matrix losses coefficients. Also, there were important secondary objectives; to validate the performance of the instrument's thermal control over the expected range of on-orbit temperatures and to verify engineering telemetry, which includes physical temperature measurements of the key radiometer components.

The 4-day T/V test was conducted in September, 2009 in CONAE's environmental test facility Teófilo Tabanera Space Center or CETT (Centro Espacial Teófilo Tabanera) in Córdoba, Argentina. During this test, the MWR's antenna reflectors were removed and replaced by broadband microwave absorber targets (Fig 4.16.a). As a result, the microwave thermal emission (apparent brightness temperature) from these blackbody targets were captured by the feeds and resulted in known Tb's that were equal to the corresponding target physical temperatures. Five precision temperature sensors were mounted on the targets to measure the temperature in different locations (one at the center and 4 at the corners) as shown in Fig. 4.16.c. To simulate the on-orbit thermal environment, the MWR instrument was placed inside an aluminum box (MWR coffin) that was covered with infrared absorbing paint as illustrated in Fig. 4.16.a. Then, the MWR coffin was put inside the T/V chamber, which was heated by infrared heaters and cooled by liquid nitrogen (Fig. 4.16.b).

An example of the temperatures for the T/V calibration test is shown in Fig. 4.17, where the black trace represents the average of the measured blackbody target temperature from the five sensors. With the assumption of unity target emissivity, the brightness temperature (Tap_{meas}) was captured by the feed horns, and the received Tb signal from each feed was sequentially routed inside the antenna switch matrix to the receiver. Because of dissipative losses of the feed horn and switch matrix components, leakage through the switches, and reflections at the feed horn apertures, the received Tb signal at the radiometer input was modified. Thus, the brightness temperature (T_{in}) at the antenna port input of the Dicke switch was calculated using linear counts and is represented by the trace of magenta color, and the blue traces represent the physical temperatures T_1, T_2, T_3, and T_4 for SW#1, SW#2, SW#3, and feed horn respectively, which appear in the MWR science data output. To compute the brightness temperature at the feed horn, the inverse radiative transfer model was used [7]:

$$T_{ap}=[T_{in}-(b_2*T_o+b_3*T_1+b_4*T_2+b_5*T_3+b_6*T_4)]/b_1 \quad (4.15)$$

where $b_1, b_2, b_3, b_4, b_5, and\ b_6$ are the antenna switch matrix (ASM) loss coefficients.

In this dissertation, the ASM loss coefficients were empirically derived. First, *Tap* in Eq.4.15 was replaced by the measured target apparent brightness, Tap_{meas}; and then a multi-variate linear regression analysis was performed using temperatures $(T_{in}, T_o, T_1, T_2, T_3, and\ T_4)$ to derive the ASM loss coefficients. Next, the apparent temperature was calculated using Eq.4.15, and the result is shown as the red trace in Fig. 4.17. The computed apparent temperature matched the measured apparent temperature during the entire time period of T/V test with a small residue,

which means that the output of the regression model is an excellent estimator for the ASM loss coefficients.

Figure 4-16 TV calibration test. a) MWR instrument with blackbody target and MWR coffin (aluminum box), b) MWR coffin inside TV chamber, c) blackbody target with the five temperature sensors.

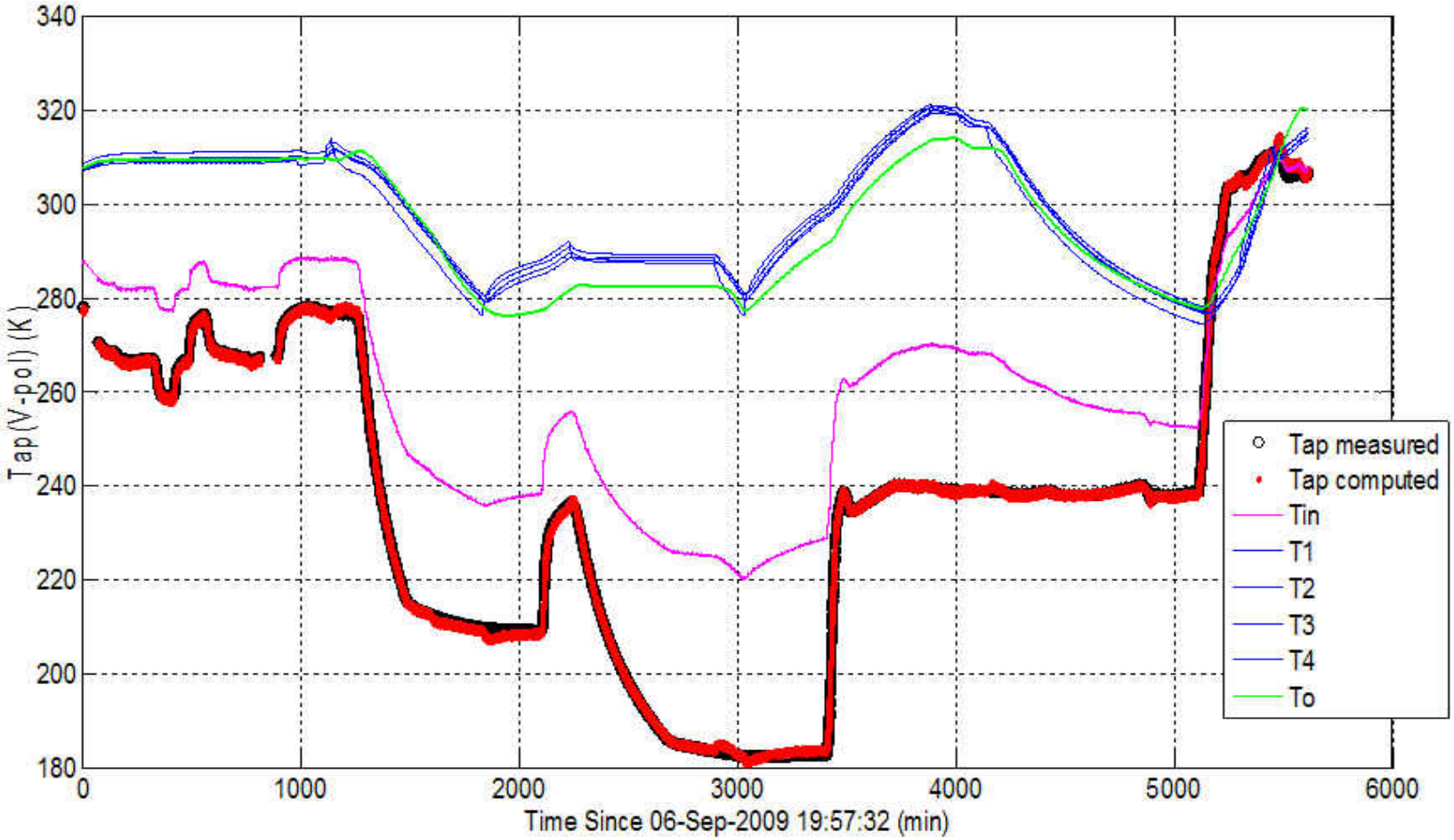

Figure 4-17 Time series of the measured apparent temperature (black circle), computed apparent temperature (red dots), calculated T_{in} using linear counts (magenta color), temperature of the switches and the feed horn (blue colors), and reference load temperature T_o (green color)

Another objective of the T/V calibration test was to characterize noise diode injection noise (T_n). For this analysis, two plateaus where T_o was stable were selected. The first plateau occurred during the time period between 200 and 800 minutes, and the second plateau was between 2400 and 2900 minutes. For each plateau, the transfer function that relates the gain-normalized and linearized Rad_counts to the T_{in} was established. Then, a linear regression was performed to retrieve the slope, which is the radiometer system gain. To calculate T_n, Eq. 2.5 is used:

$$T_n = \frac{C_n - C_a}{gain} \tag{4.15}$$

By subtracting antenna counts from antenna + noise counts, the noise diode injected noise temperature was estimated. Since, over these plateaus the receiver physical temperature was constant, the gain was expected to be stable and any changes are attributed to variations of the T_n. The results, of this analysis over the two plateaus, are shown in Fig.4.18, where the magenta and green colors corresponds the first and second plateau respectively. From this figure it is estimated that there is a small physical temperature dependence of the noise diode injected temperature of about 0.4K.

As a conclusion of this chapter, it should be noted that all MWR pre-launch calibration tests were conducted without reflectors, and it was assumed that the feed-horns capture only the signal coming from the absorbers with no spill over. Therefore, it was necessary to perform the post-launch calibration to derive the Antenna Pattern Correction (APC) coefficients, as will be discussed in the next chapter.

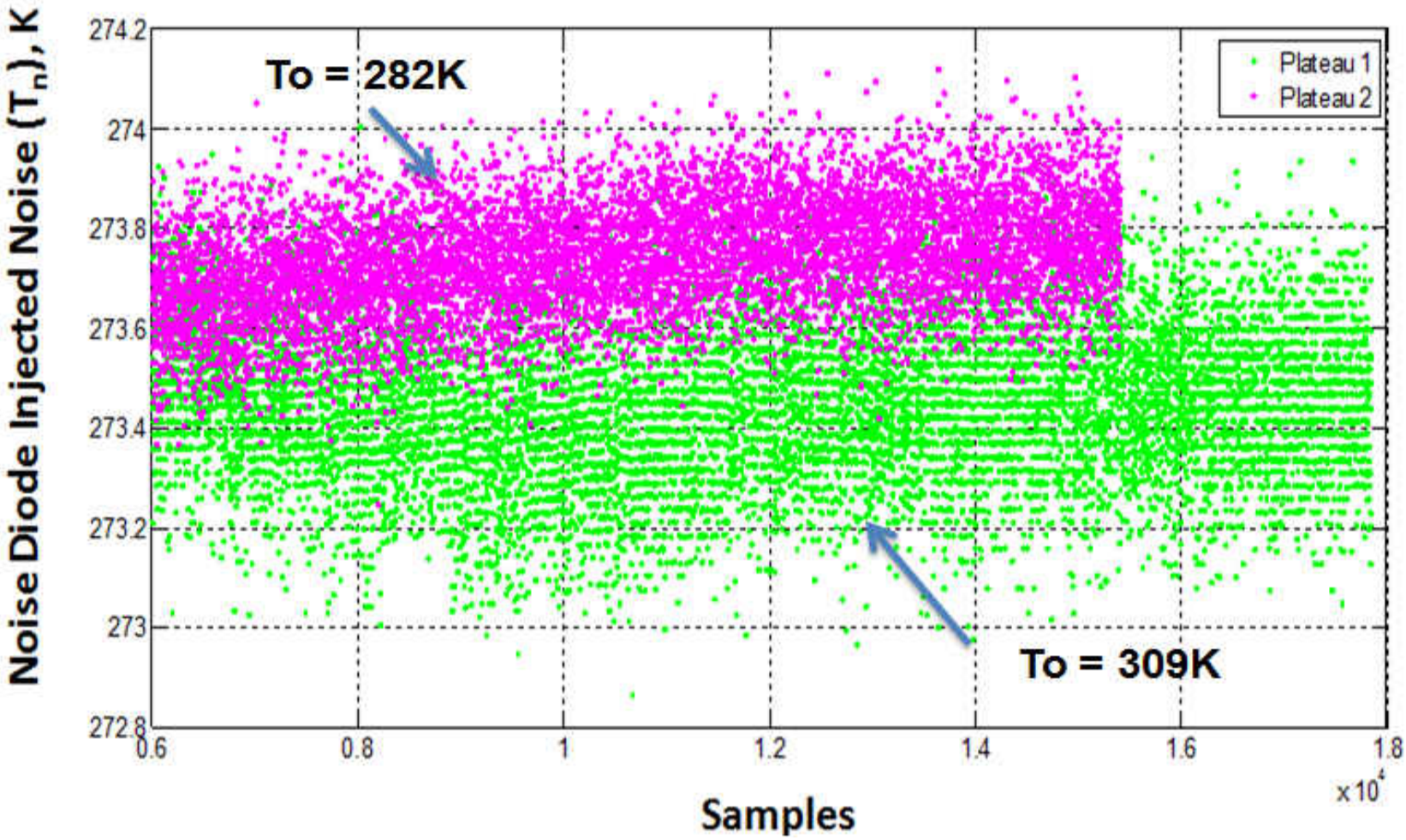

Figure 4-18 Tine series of the noise diode injection noise (Tn) during two different plateaus. The characterization of each plateau were performed separately

CHAPTER 5
MICROWAVE RADIOMETER POST LAUNCH CALIBRATION VALIDATION

After a successful reanalysis pre-launch radiometric calibration tests, there remained several possible sources of Tb biases in the V6.0 computed brightness temperature. For example, the T/V calibration test was performed without the reflectors being present, and it was assumed that the emissivity of the absorber target was unity and that the feed-horns captured only the blackbody emission coming from them without spill-over. On-orbit, the MWR's aluminum reflectors were assumed to be non-emissive, but certainly there were feed spill-over and antenna pattern (main beam efficiency) considerations that must be taken into account. Thus, post-launch radiometric calibration was necessary to complete the MWR V6.0 counts to Tb algorithm, specifically in developing an antenna pattern correction algorithm and the removal of other calibration biases.

Finally, the quantitative evaluation (validation) of V6.0 Tb's was performed by the analysis of special Deep Space Calibration tests and by the inter-satellite radiometric calibration (XCAL) with the WindSat satellite radiometer. Results are presented that demonstrate that V6.0 fully meets the requirements for the MWR Tb's product L1B.

5.1 Dataset for MWR XCAL

5.1.1 WindSat Comparison

The Naval Research Laboratory's WindSat (WS) satellite radiometer [12], on board the United States Air Force's Coriolis satellite, is an excellent choice for the radiometric calibration

standard for the MWR XCAL. First, WS is a well calibrated radiometer that has been used in a number of inter-satellite radiometric calibrations for NASA's Precipitation Measurements Program [8]. Second, the 3 MWR channels (23 GHz H-pol and 37 GHz V- & H-pol) are subset of the WindSat frequencies, which is highly desirable for XCAL. Finally, both the AQ/SAC-D and Coriolis satellites fly in sun-synchronous orbit with similar inclination angles and have the same equatorial crossing time that frequently results in both radiometers viewing the same earth scene at nearly the same time.

Before the AQ launch, a simulation was performed to evaluate the feasibility of using WS to perform XCAL of MWR. In his thesis, Kahn [10] used Satellite Tool Kit (STK) [16] to evaluate temporal and spatial collocation between MWR and WindSat and an example of his results are shown in Fig. 5. 1. Because the satellites fly at different altitudes, their orbits drift into and out of phase (time coincidence and spatial collocation) with a period of approximately 45 hours. Thus, the overlapping swaths vary on a daily basis according to the orbits relative phasing, which results in an average of ~ 60% of MWR observations being collocated with WindSat within a temporal window of ±1hr.

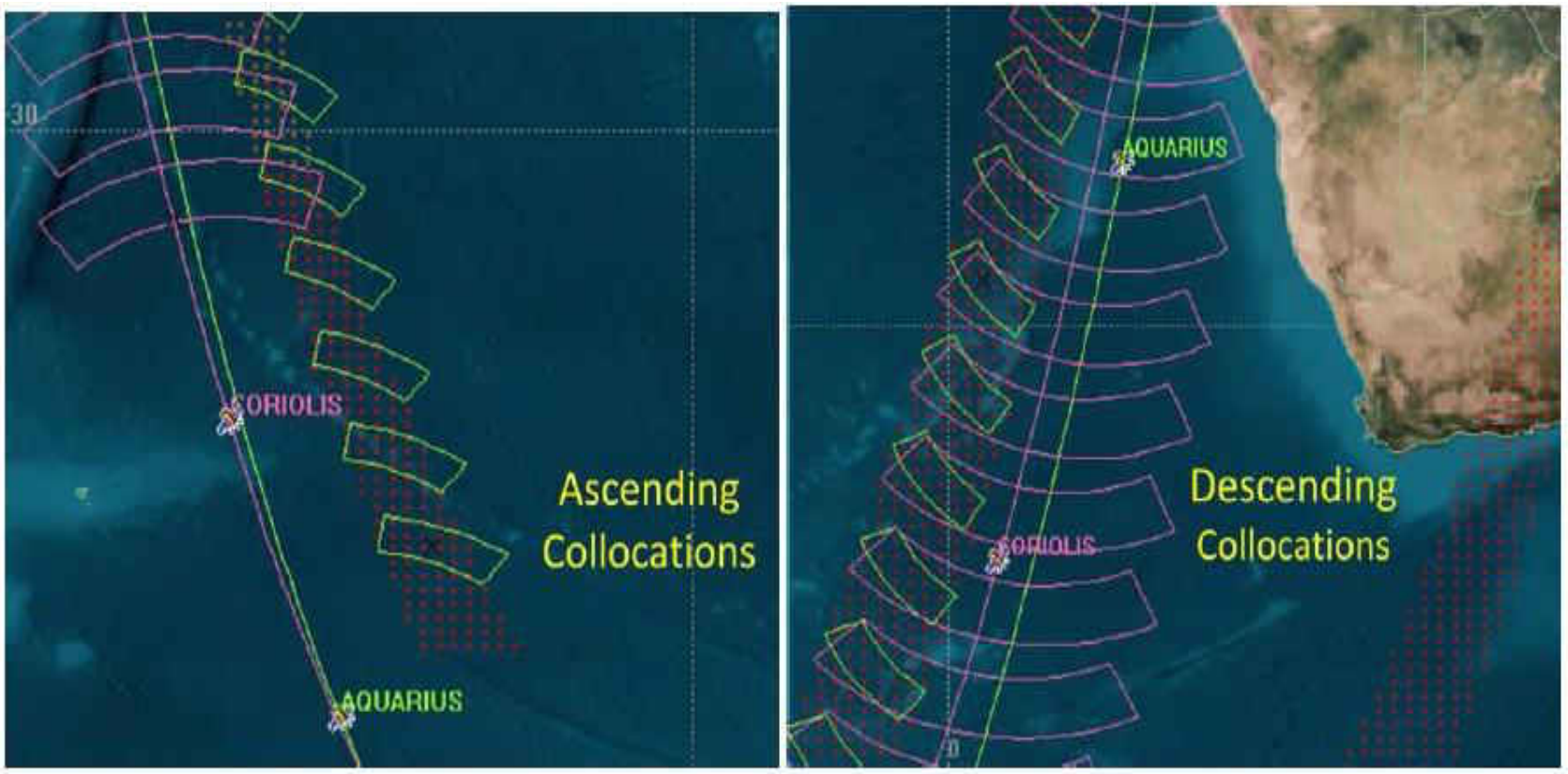

(a) (b)

Figure 5-1Satellite Tool Kit (STK) simulation collocations between MWR (green) and WindSat (magenta) for ascending (a) and descending (b) passes. The red color dots are the collocated 0.5º resolution boxes [10].

5.1.2 MWR Dataset

MWR's science data were multiplexed with other instruments on board of AQ/SAC-D satellite and captured twice/day by the CONAE ground station. These data were sorted and processed by CONAE to provide an earth-located MWR dataset of engineering data (physical temperatures, raw radiometer counts, IFOV center latitude and longitude, time, etc.) known as L1A [4, 7]. Next, these MWR data were used as input to the V6.0 counts-to-Tb algorithm (supplied by CFRSL) to produce the L1B Tb dataset, which included MWR smear and non-linearity correction discussed in Chapter 3. These MWR Tb's were binned into 1° boxes over oceans and collocated with WS and environmental data from a NOAA numerical weather model for use in the CAL/VAL process.

5.1.3 GDAS Data

GDAS (Global Data Assimilation System) is one of the operational, global, numerical weather analyses produced by the National Weather Service's National Centers for Environmental Prediction (NCEP). The GDAS data are produced every six hours at 00, 06, 12, and 18 UTC on a 1º latitude/longitude grid, which results in a matrix (181 x 360). A subset of GDAS environmental parameters are the input to the CFRSL XCAL RTM, namely: sea surface temperature, 10 meters wind speed, atmospheric (height) profiles of pressure, temperature, specific humidity and cloud liquid water at 21 levels between pressures of 1000 mb and 100 mb. The RTM outputs theoretical Tb's for both MWR and WS for CAL/VAL purposes discussed below.

5.2 Post Launch MWR Antenna Pattern Correction and Radiometric Calibration

As mentioned above, there were neither tests nor analysis to correct for the effect of the MWR antenna pattern and other radiometric biases on the antenna temperature. Therefore, a post launch calibration using inter-satellite radiometric comparison technique, developed by Central Florida Remote Sensing Lab (CFRSL) [8], was used in this dissertation to provide the APC and remove other radiometric biases.

To correct for the APC and other radiometric biases, a scatter diagram is performed between The WS Tb's and MWR antenna temperature T_a, then a linear regression was applied to retrieve the coefficients (slope and offset). By tuning up The MWR Tb to match the WS Tb, we performed the APC and removed the undesired power captured by the feedhorns. Because the WindSat frequencies correspond to the MWR channels (23 GHz and 37 GHz), and WS and MWR have different EIA (EIA for WS is 53°, whereas the MWR beam EIA's are 52° and 58° respectively for odd and even beams), it was necessary to match the corresponding MWR EIA's using simulated radiative transfer model (RTM) values calculated using collocated GDAS geophysical parameters. Therefore, the adjusted WS Tb (WS_{adj}) is expressed as:

$$WS_{adj} = WS_{obs} + \left(MWR_{sim} - WS_{sim}\right) \tag{5.1}$$

where WS_{obs} is the WS observed Tb, MWR_{sim} is MWR simulated Tb (at 52° or 58°), and WS_{sim} is WS simulated Tb (at 53°). Note that the second term in the Eq. 5.1 is the expected difference between the WS and MWR Tb's, due to different EIA's.

In the counts-to-Tb algorithm V6.0, the brightness temperatures are computed based upon the inverse transfer function (see Chapter-4). Unfortunately, this results in antenna

temperatures that are biased because of uncorrected antenna pattern effects and other radiometric calibration errors. Fortunately, the simultaneous and collocated Tb's provided in the WS sensor data record (SDR) are the true scene apparent brightness. Thus, the linear regression between observed MWR Tb's and adjusted WS Tb's (to account for EIA differences) provides the necessary MWR APC, which also removes MWR inter-beam radiometric biases. This procedure was performed separately for each channel and each beam, and an example for 37V for beam #1 is shown in Fig. 5.2.

In this analysis, 20 days of XCAL ocean Tb's (September through December, 2012) were combined with MWR Tb's from the deep space calibration measurements. Previous analysis of the WindSat deep space calibrations [9] demonstrates that the observed WS Tb's were nearly identical to theoretical values; therefore the corresponding WS space measurements in this figure were assumed equal to 2.73 K. Thus, space and clear sky ocean measurements were combined to perform the scatter diagram and linear regression, which converts MWR antenna temperature T_a into co-polarized brightness temperature Tb at the antenna boresight. This characterization of the APC removes the effect of unwanted radiation that is captured in antenna paternal outside of the main beam (spill over). This can be achieved using the following linear equation that relates T_a and Tb [6]:

$$T_b = \left(T_a - T_{spillover}\right) * \frac{1}{\eta_{MB}} \tag{5.2}$$

where η_{MB} is the main beam efficiency and defined as

$$\eta_{MB} = \frac{1}{Slope} \tag{5.3}$$

and $T_{spillover}$ is the brightness temperature contribution for side lobes outside the main beam and defined as:

$$T_{spillover} = -\eta_{MB} * offset \tag{5.4}$$

Figure 5.2 shows a comparison between MWR observed Tb and WS adjusted Tb for 37V for beam # 1. Before correction (Fig.5.2.a), the slope and the offset of the linear regression are 0.92329 and 0.40928, respectively. Note that the WS Tb includes the APC correction. This means that the slope and the offset values are due to the APC and other radiometric biases related to the MWR Tb's. After correcting the MWR observed Tb using Eq. 5.2, the slope and the offset of the linear regression which is applied only on clear sky ocean and space data (excluding land) became 0.99952 and 0.091 respectively. This demonstrates that the APC and other radiometric biases were removed successfully by forcing the MWR observed Tb to match the WS adjusted Tb. Note that the red color in Fig 5.2.b represents the land measurements of MWR observed Tb and WS observed Tb. No adjustments of the Tb observations over land are made because the incidence angle dependence of Tb is negligible. By holding the ocean and space observation plot and performing a scatter diagram of the land measurements of both instruments, we can see that the linear regression over space and ocean points is a good fit for the land measurements. Despite the fact that MWR and WindSat share some similarities, the spatial coverage causes the differences in Tb over land between the two sensors. The WindSat has a mean spatial resolution of ~15 km, whereas MWR has a mean spatial resolution of ~50 km (~ 3 times the WindSat footprint). This causes the MWR and WindSat observations to be inconsistent, especially for complex terrain and heterogeneous landscapes. It is expected that the

higher biases will be over large water bodies, such as coastal areas, Amazon River, and Great Lakes.

Counts-to-Tb algorithm V6.0 Matlab code and ASM coefficients are giving in Appendices C and D respectively.

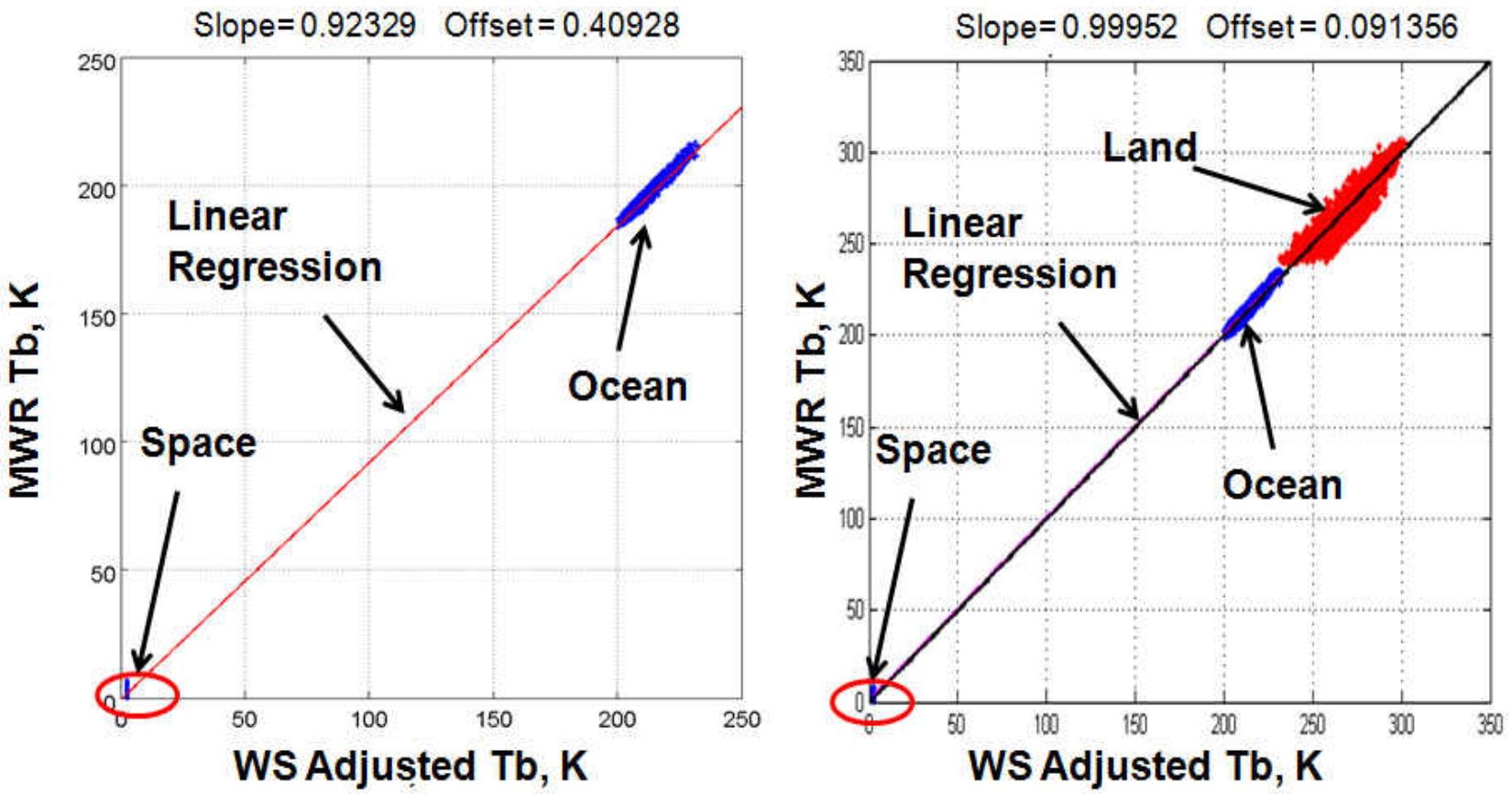

(a) **(b)**

Figure 5-2 A comparison of MWR observed Tb (V6.0) and WS adjusted Tb for 37V beam # 1 : a) before correction, b) after correction**.**

5.3 Post-Launch Validation

5.3.1 Deep Space Calibration

A “deep space calibration” (DSC) maneuver for satellite microwave radiometers is a special on-orbit test, whereby the spacecraft is reoriented from the nominal earth-pointing mode to cause the microwave sensor antenna to view space. Space presents a known brightness temperature scene that is non-polarized, homogenous and isotropic black body radiance of 2.73 K for a wide range of microwave frequencies up to ~ 100 GHz. As such, space makes an excellent target for radiometric calibration at the low-end of the brightness temperature scale, and the CFRSL has considerable experience in analysis of DSC starting with the WindSat satellite radiometer in 2004 [9, 12] and continuing through the present.

During the year of 2012, Aquarius/SAC-D performed several pitch maneuvers for the calibration purposes of the L-band AQ radiometer. MWR also benefited from these maneuvers to obtain Tb measurements on all three channels and 8 beams/channel at the cold end of the Tb scale. Results from 7 DSC revs were used in the post-launch Cal/Val campaign as discussed in Chapter 4, and this section concentrates on validation of MWR V6.0 Tb at the cold end.

A cartoon of the DSC maneuver is shown in Fig. 5.3. In normal science mode, the satellite flies clockwise around the Earth, and slowly rotates in pitch (360°/orbit) to maintain earth pointing for AQ and MWR to observe the earth brightness temperatures. At phase -1, the satellite pitch changes from a normal nadir-pointing attitude until 180º pitch-up attitude is achieved (phase-2). Between phase-2 & -3, the pitch remained constant for ~ 10 min where the main reflectors were viewing the space, and then the pitch reverses (ramps down) to the nominal 0º pitch attitude. The entire DSC occurs in less than one-half an orbit (~ 30 – 45 minutes).

For the MWR frequencies, space is a uniform distributed target of a brightness temperature 2.73K. Since the black body radiance is homogeneous and isotropic, the brightness temperature is constant regardless of where the antenna beam is pointing. Given this fact, all 8 antenna beams should see the same T_{ap} during the entire time that the antenna views space. Thus, a comparison of V5.0S and V6.0 during DSC is indicative of inter-beam radiometric biases that may result because of improper characterization of the ASM losses and/or antenna pattern effects. A comprehensive analysis of the MWR DSC is beyond the scope of this dissertation; however, several important results are presented as shown in Fig. 5.4 (and Appendix-F).

Considering the left side panel of this figure (Fig.5.4.a), where the y-axis is Tb and the x-axis is samples (relative time), at approximately 1150 samples the spacecraft has pitched-up to cause the forward-looking Ka-band beams to leave the earth, and between 1200 and 1300 samples the Tb are relatively stable, while the beams view space. Between 1300 and 1350, the spacecraft reached its maximum pitch, and the Tb's monotonically increase a few Kelvin as the antenna sidelobes progressively illuminate the "hot earth". After 1350 the spacecraft pitch reverses and the Tb time series is symmetric to the "pitch-up" portion of the DSC. From these Tb time series plots, it is obvious that the MWR V5.0S radiometric calibration is seriously flawed and the radiometric biases range from -30 to -45 K. Further inter-beam radiometric biases are ~ ± 10 K.

On the other hand, in the right hand side panel of Fig. 5.4.b, during the period of 1200 to 1300 samples MWR Tb's results for V6.0 are in excellent agreement with the expected scene Tb of 2.7 K. After this time all beams exhibit very similar patterns as the sidelobes intercept the radiometric hot earth, but unlike V5.0S, here all beams have small inter-beam biases < 1 K.

Overall V6.0 has no apparent deficiencies at the cold end of the scene brightness temperatures, which implies no APC problems nor issues with the ASM loss coefficients.

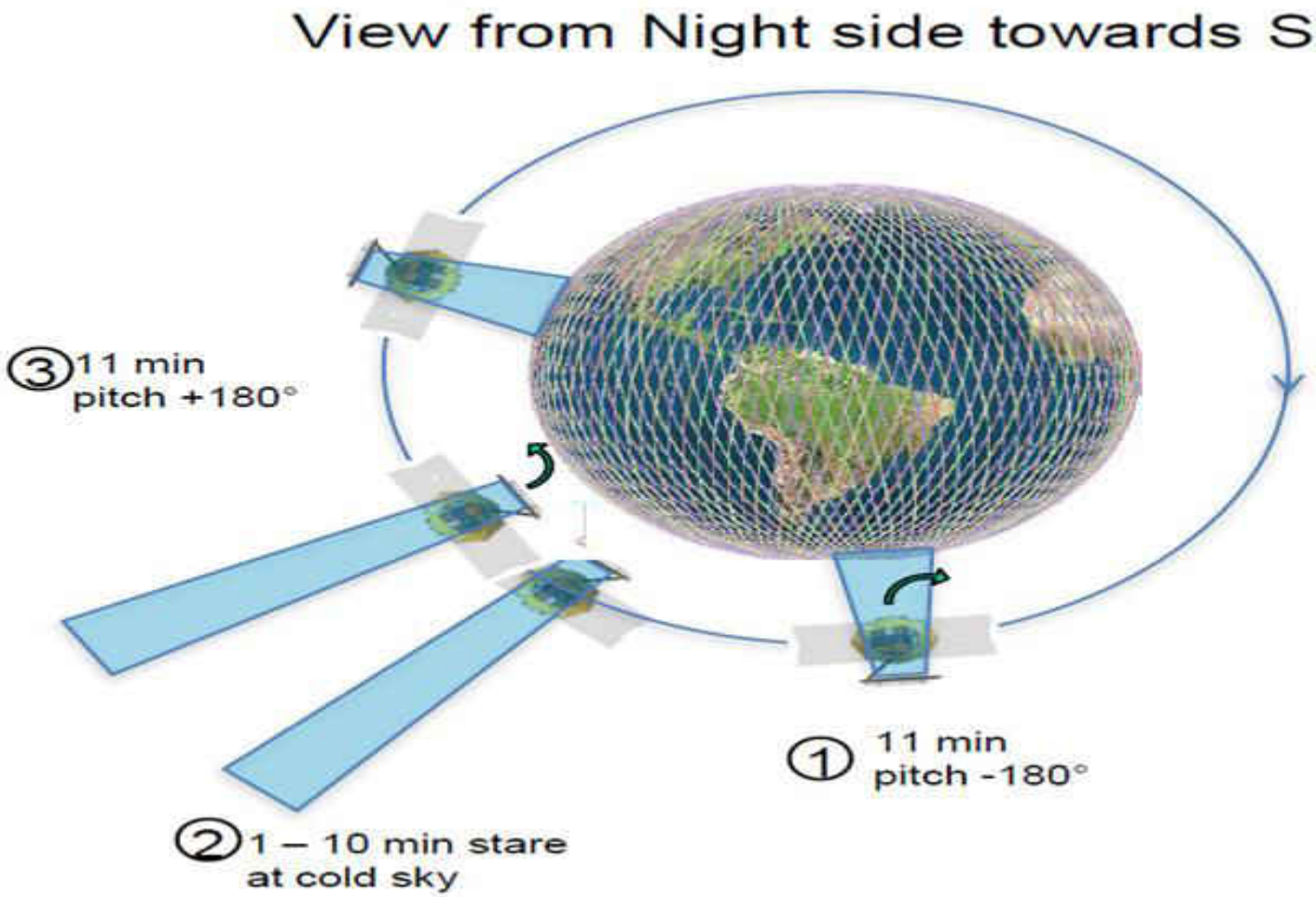

Figure 5-3 Cold Sky Calibration

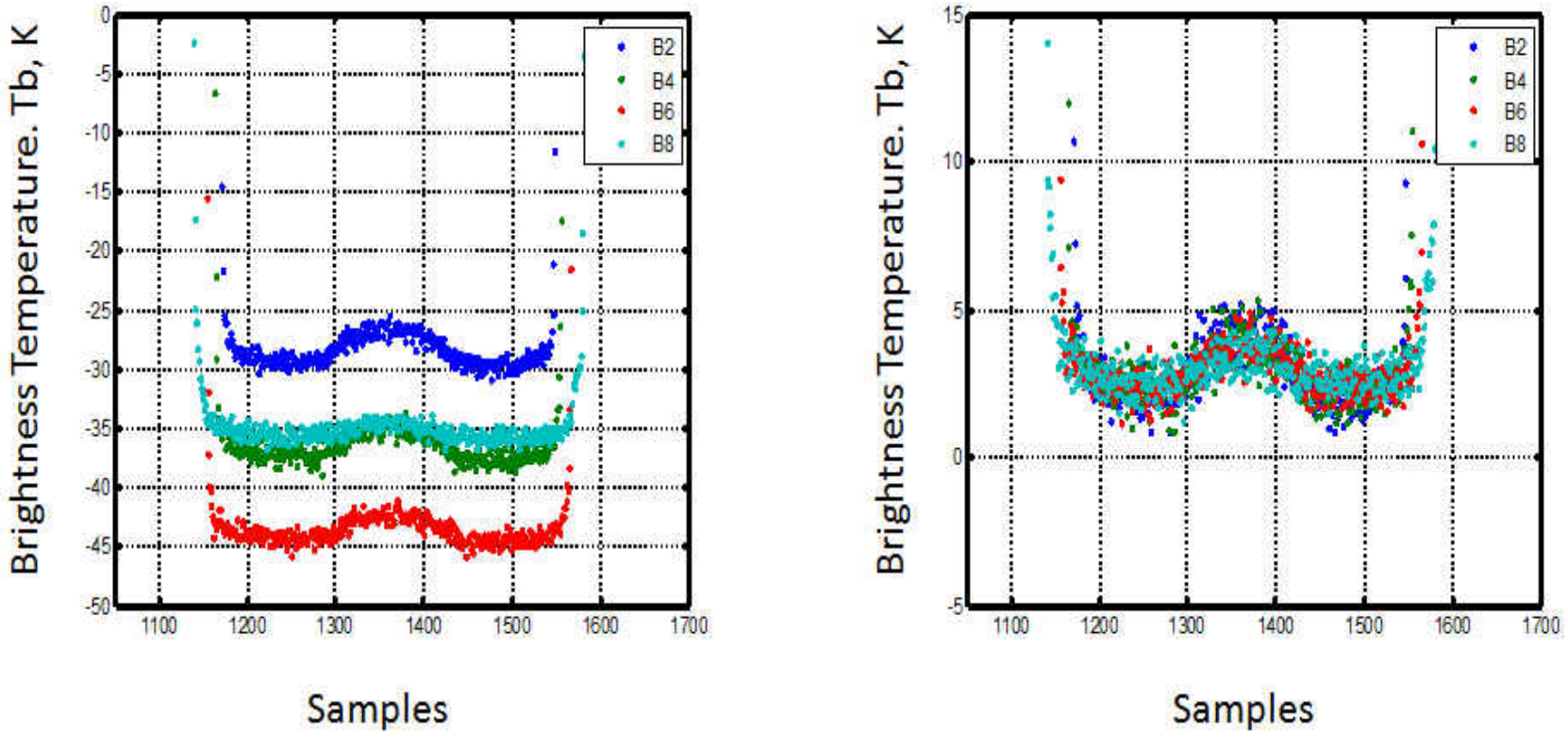

(a) (b)

Figure 5-4 37V, cold sky calibration brightness temperature measurements for even beams for a) V5.0S, b) V6.0

5.3.2 V6.0 Counts to Tb Validation

The final validation of the MWR V6.0 counts to Tb was performed using the inter-satellite radiometric comparison (XCAL) between MWR and WS Tb's over ocean. The specified Tb stability for MWR is ± 1 K under all on-orbit ocean scene conditions that includes both random and systematic variations, and this is the standard for mission success that is levied upon the MWR.

To perform the XCAL between MWR and WindSat (WS), a match-up dataset was created using the steps illustrated in the flow diagram in Fig. 5.5. In this process, WS is the radiometric calibration standard, which has been full vetted in other NASA XCAL activities [8] and has been shown to be stable to < ± 0.1 – ± 0.2 K over 1 year. In this dissertation, MWR is the "target satellite radiometer" to be calibrated relative to WS. The MWR XCAL was performed every 5 days for the period of ~ 2 years. In each 5 day period 24 radiometer beams were compared to WS and Tb biases were estimated.

The first step in the XCAL process is to grid the data (MWR and WS data) in a 1^{o} resolution box. Because the environmental files from GDAS are generated at 00, 06, 12, and 18 hours Greenwich Mean Time (GMT), the closest file within ± 3hrs of the grid time is chosen for collocation with MWR and WS. Next, we perform a spatial and temporal collocation between MWR, WS and GDAS within ± one-hour time window over the 1^{o} boxes. A typical example of this spatial/temporal collocation for one day between MWR and WS is shown in Fig. 5.6, which results in ~ 60% of MWR measurements being collocated with WS.

Next, for each 1° box, we calculate the theoretical (expected Tb differences) between two satellites with perfect radiometric calibration. This is accomplished by running theoretical ocean Tb calculations (RTM) using the environmental parameters from GDAS and the respective

radiometer parameter information (frequency, polarization and incidence angle) from both instruments. After obtaining theoretical Tb's for WS and even and odd MWR beams, we calculate the theoretical difference for the 24 beam sets of MWR.

Next, we average all Tb's for each MWR channel/beam and also average WS Tb's within the 1° box. We run conservative filters to eliminate non-homogeneous clear-sky ocean scenes, and then after filtering, calculate the observed Tb differences.

Finally, the last step is to calculate the "double difference" of the single differences. This step is important because it eliminates several "common mode" error sources and results in a very robust Tb bias estimate that is mostly independent of the radiometer properties and the ocean scene brightness. An example of the WS/MWR XCAL results has been reported by Santos-Garcia [17].

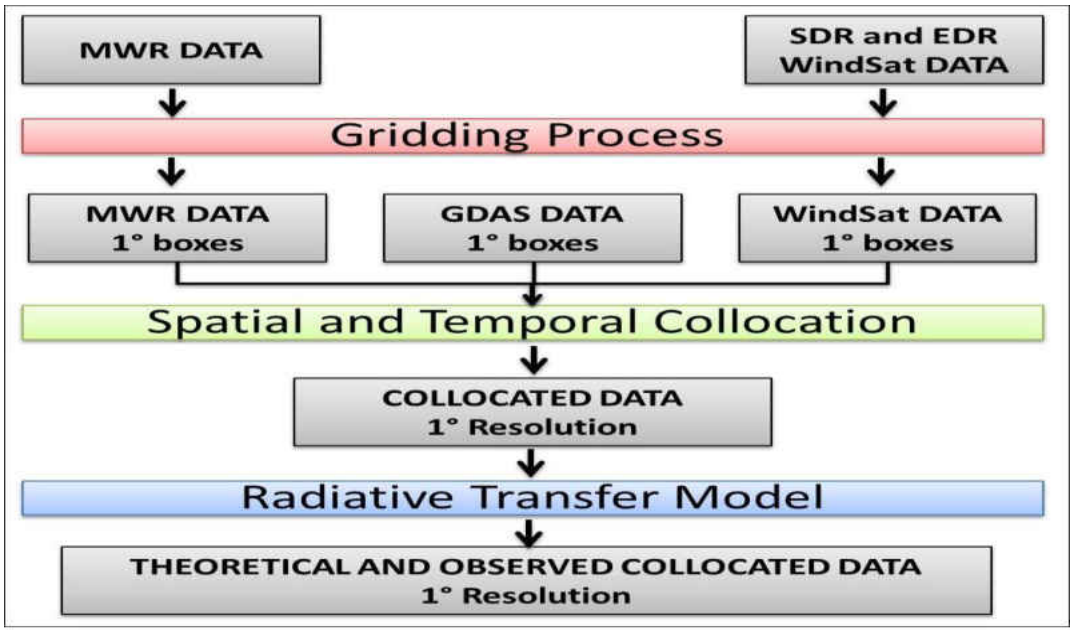

Figure 5-5 Flow diagram of CFRSL XCAL approach.

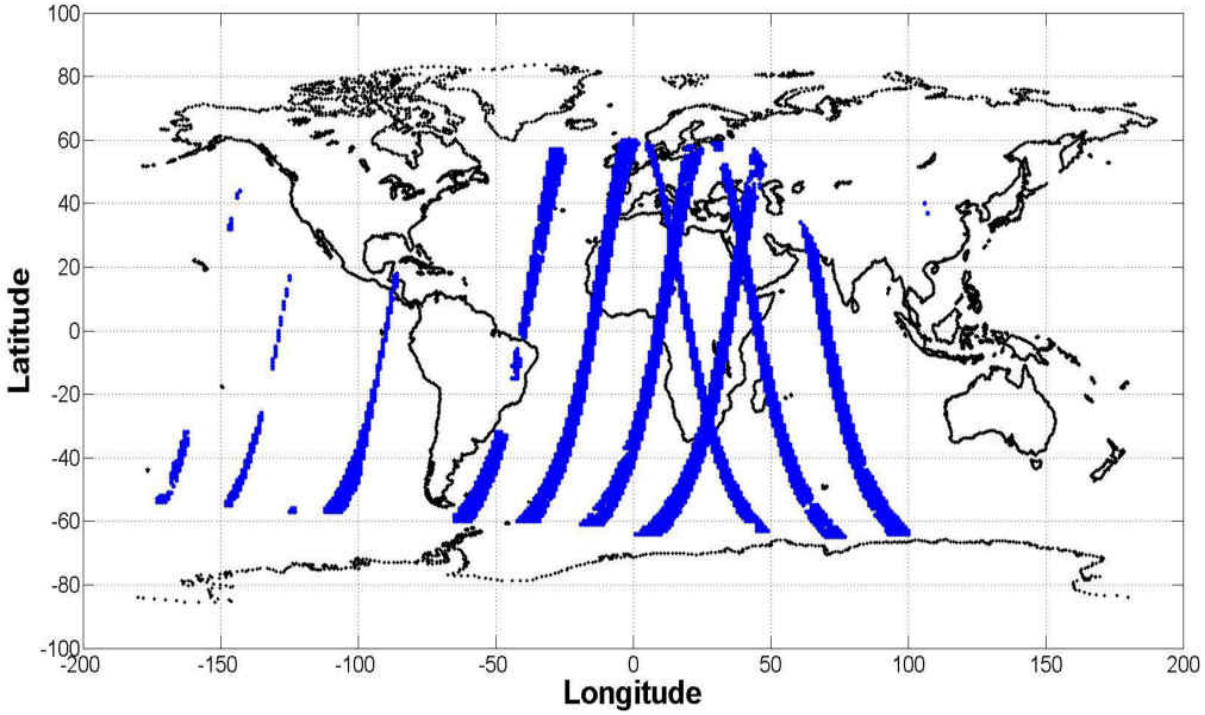

Figure 5-6 MWR and WindSat temporal and spatial collocation within ±1 hour window and a 1° x 1° Lat/Lng box.

In this dissertation, MWR (V6.0) and WS XCAL data from 2012 and 2013 were used to validate the MWR Tb. Based upon thousands of 1° boxes, a five-day average double difference radiometric bias was calculated by MWR channel and beam, to verify the results of the MWR counts-to-Tb algorithm (V6.0).

Figure 5.7 shows the results of the five day average double difference for the 8 beams for 37 GHz V-pol for the year of 2012, and similar results for the other MWR channels are presented in Appendix-E. Because WS is a very well calibrated instrument, any bias in the Fig. 5.7 is related to MWR Tb's error. Starting Jan 2012 until March 2012, it can be seen that all the beam has a bias close to -1K, which after all the beams became stable except beam # 7, which has more fluctuation. The results of the double difference technique of 2012 demonstrate that the MWR calibration (V6.0) meets the ±1K specification for the 37GHz V-pol channel for all the beams. Note that the bars of this figure present the standard deviation of the double difference.

Figure 5.8 presents the five day average double difference for all the beams for 37 GHz V-pol for time period of Jan-Nov of 2013. From this figure, it can be seen that the even beams have the same pattern, which is expected. At the beginning of the year, the even beams biases were close to zero, after which they start increasing until they reach their max (~ 1K), then they start decreasing. Beam #1 & #3 look also stable during the entire year with a bias less than one, and they have the same pattern, which is also expected. Beam #7 has more fluctuations, but kept the specification of ±1K bias. However, beam #5 has an anomalous ~ -1.5K drift. The mean and standard deviation of figures 5.7 & 5.8 are presented in tables 5.1, 5.2, 5.3, and 5.4.

Another useful evaluation is to display the DD bias as a function of latitude and time (5 day steps). In this manner, seasonal variations may appear differently in ascending (latitudes 0° – 180°) and descending (180° - 360°). Figures 5.9 & 5.10 show five day average in 5° Lat Zones

for 37 GHz V-pol for odd and even beams separately. Thus in this analysis, the even (and odd) beams were averaged in latitude bins that separated ascending and descending orbit segments, which ranged from 0° - 360º , where 0º, 180º, and 360º correspond the south, north, and south poles respectively. Next, the data were averaged every five days every 5º latitude. The colors in this image represent the MWR biases. From these figures, we can conclude that there are no observable anomalies and that the V6.0 Tb calibration meets the ± 1 K spec. Again similar results for the two other MWR channels are presented in Appendix-E.

In addition, the validation of Tb V6.0 over land are presented in Appendix-G

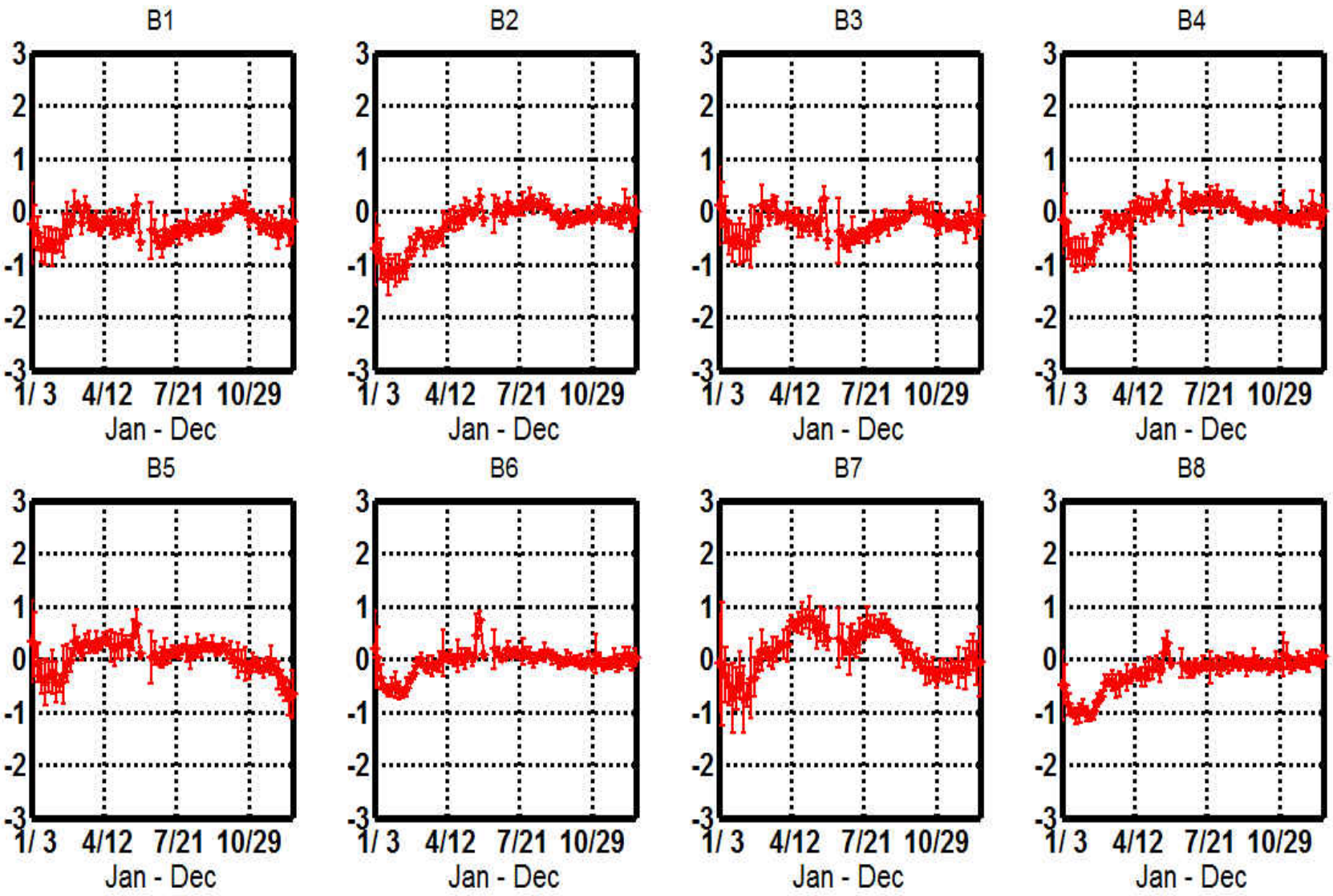

Figure 5-7 37 GHz V-pol five day average double difference for 8 beams, from 2012.

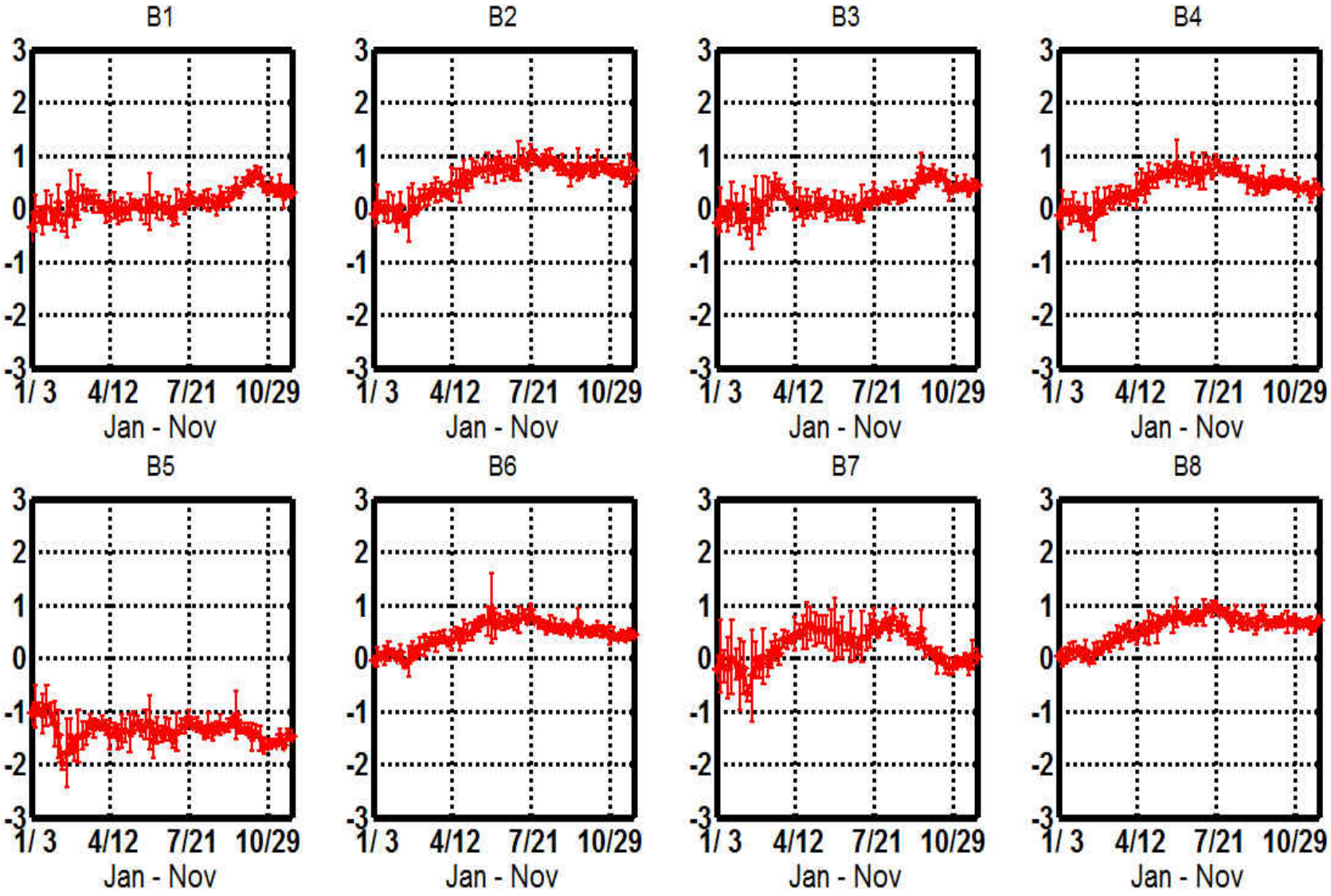

Figure 5-8 37 GHz V-pol five day average double difference for 8 beams, from 2013.

Table 5-1 Monthly average of double differences per beam for year 2012

Beam	Jan	Feb	Mar	Apr	May	Jun	Jul	Aug	Sep	Oct	Nov	Dec
1	-0.492	-0.467	-0.038	-0.247	-0.169	-0.497	-0.442	-0.292	-0.193	0.047	-0.227	-0.314
2	-0.970	-0.966	-0.511	-0.237	0.034	-0.030	0.067	0.158	-0.112	-0.124	-0.048	-0.044
3	-0.290	-0.491	0.042	-0.167	-0.171	-0.502	-0.453	-0.237	-0.068	-0.052	-0.199	-0.186
4	-0.582	-0.674	-0.182	-0.058	0.140	0.123	0.184	0.215	-0.032	-0.079	-0.094	-0.035
5	-0.136	-0.265	0.274	0.302	0.340	0.047	0.115	0.175	0.215	-0.040	-0.106	-0.477
6	-0.350	-0.485	-0.097	0.039	0.211	0.107	0.108	0.069	0.000	-0.064	-0.039	-0.009
7	-0.398	-0.434	0.150	0.581	0.646	0.317	0.434	0.615	0.207	-0.198	-0.203	-0.068
8	-0.857	-0.922	-0.445	-0.303	-0.046	-0.147	-0.149	-0.089	-0.089	-0.111	-0.033	-0.011

Table 5-2 Standard deviation of the double differences per beam for each month of 2012

Beam	Jan	Feb	Mar	Apr	May	Jun	Jul	Aug	Sep	Oct	Nov	Dec
1	0.369	0.330	0.228	0.175	0.242	0.304	0.189	0.159	0.170	0.170	0.153	0.249
2	0.381	0.281	0.149	0.216	0.177	0.217	0.145	0.134	0.140	0.097	0.146	0.229
3	0.454	0.389	0.221	0.187	0.284	0.316	0.155	0.185	0.167	0.200	0.147	0.227
4	0.432	0.281	0.126	0.342	0.201	0.215	0.151	0.152	0.123	0.110	0.169	0.206
5	0.496	0.376	0.178	0.210	0.263	0.258	0.142	0.183	0.109	0.232	0.165	0.325
6	0.420	0.191	0.128	0.224	0.334	0.183	0.128	0.123	0.106	0.100	0.173	0.154
7	0.663	0.504	0.236	0.291	0.290	0.340	0.311	0.162	0.211	0.213	0.211	0.367
8	0.341	0.182	0.164	0.164	0.266	0.158	0.145	0.140	0.130	0.110	0.206	0.143

Table 5-3 Monthly average of double differences per beam for year 2013

Beam #	Jan	Feb	Mar	Apr	May	Jun	Jul	Aug	Sep	Oct	Nov
1	-0.144	-0.011	0.161	-0.022	0.060	-0.001	0.092	0.139	0.292	0.530	0.345
2	-0.024	-0.028	0.270	0.447	0.712	0.760	0.896	0.876	0.711	0.773	0.691
3	-0.093	-0.082	0.270	0.076	0.080	-0.003	0.137	0.262	0.491	0.523	0.423
4	-0.055	-0.061	0.205	0.384	0.686	0.668	0.746	0.686	0.471	0.480	0.362
5	-1.008	-1.571	-1.359	-1.376	-1.271	-1.422	-1.295	-1.325	-1.261	-1.492	-1.542
6	0.039	0.043	0.287	0.394	0.665	0.663	0.755	0.600	0.558	0.497	0.427
7	-0.129	-0.234	0.104	0.457	0.574	0.318	0.470	0.635	0.317	-0.053	-0.044
8	0.074	0.116	0.364	0.494	0.697	0.750	0.893	0.732	0.673	0.683	0.640

Table 5-4 Standard deviation of the double differences per beam for each month of 2013

Beam	Jan	Feb	Mar	Apr	May	Jun	Jul	Aug	Sep	Oct	Nov
1	0.273	0.350	0.224	0.201	0.243	0.181	0.206	0.156	0.155	0.157	0.152
2	0.238	0.299	0.170	0.235	0.179	0.180	0.207	0.147	0.139	0.146	0.161
3	0.297	0.395	0.288	0.235	0.195	0.180	0.201	0.144	0.193	0.180	0.115
4	0.230	0.280	0.176	0.240	0.228	0.186	0.184	0.147	0.147	0.105	0.125
5	0.280	0.452	0.255	0.216	0.273	0.207	0.204	0.157	0.164	0.191	0.117
6	0.132	0.176	0.147	0.158	0.316	0.142	0.140	0.111	0.114	0.099	0.085
7	0.462	0.528	0.302	0.252	0.332	0.293	0.274	0.165	0.198	0.178	0.158
8	0.137	0.148	0.162	0.174	0.187	0.106	0.124	0.147	0.122	0.120	0.097

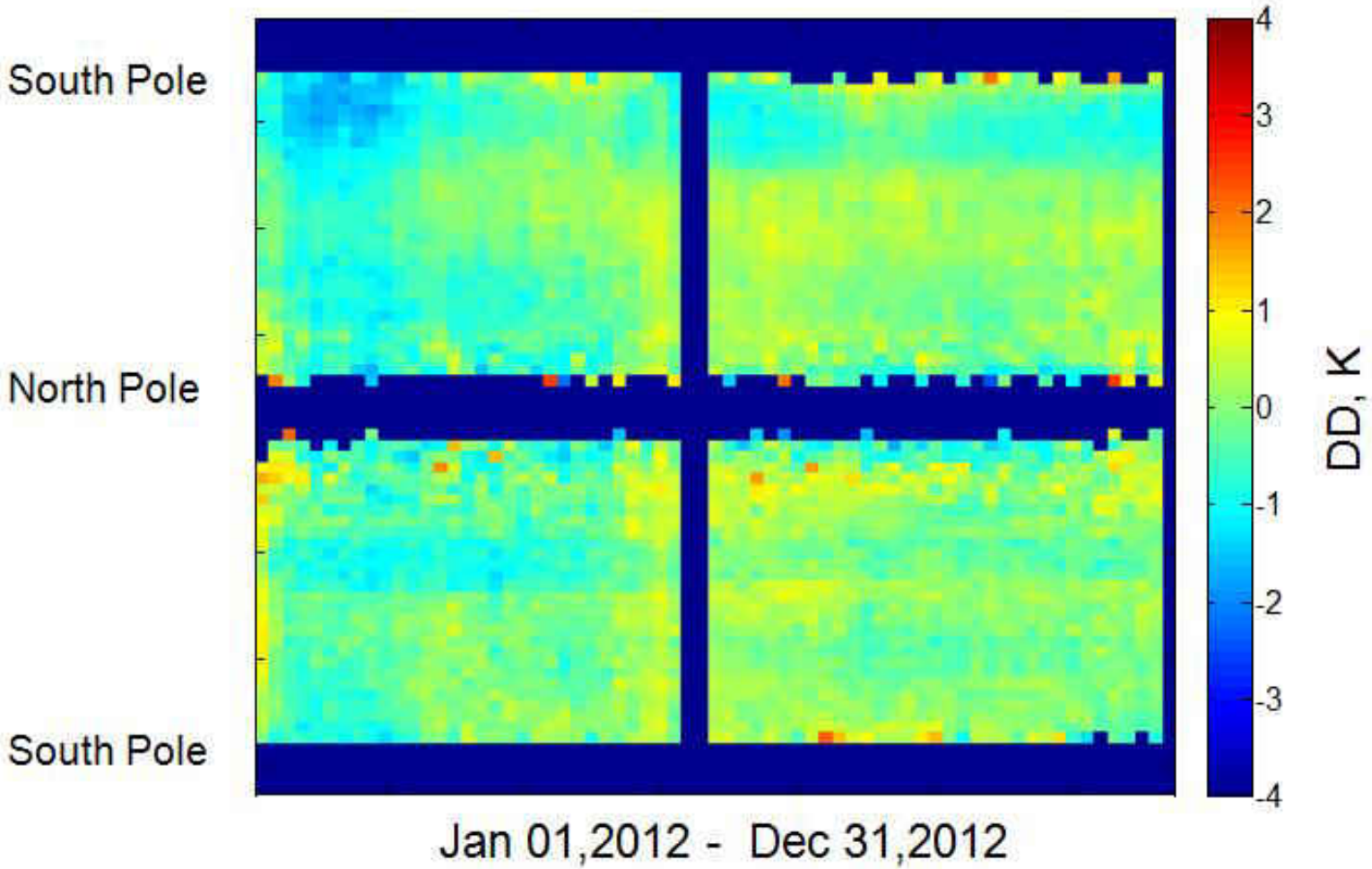

Figure 5-9 Five days Average in 5° Lat Zones for 37 GHz V-pol, even beams for the year of 2012. The colors represent the DD.

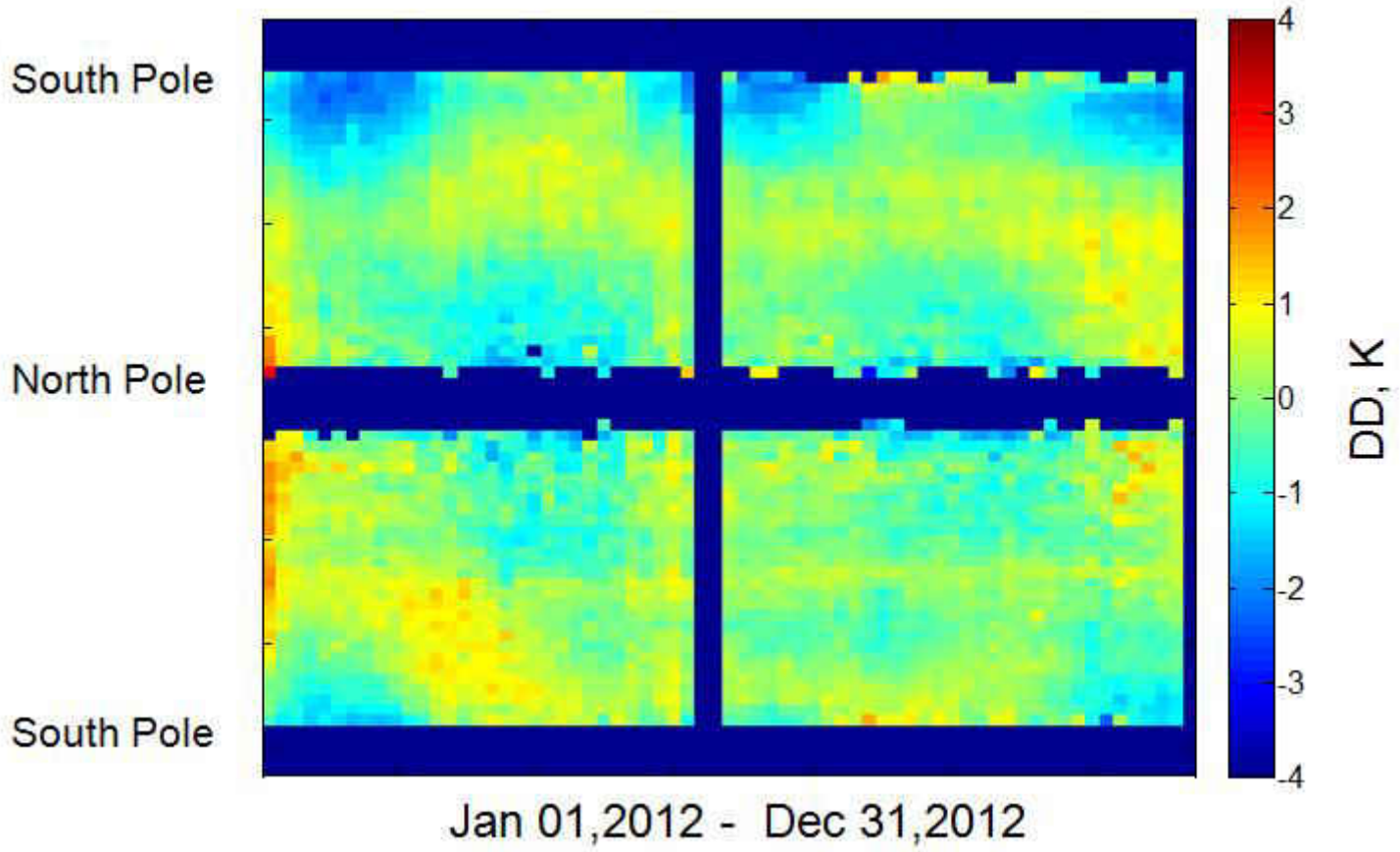

Figure 5-10 Five days Average in 5° Lat Zones for 37 GHz V-pol, odd beams for the year of 2012. The colors represent the DD.

CHAPTER 6
CONCLUSION AND FUTURE WORK

6.1 Conclusion

The main objective of this dissertation is the development of a new MWR counts-to-Tb algorithm (V6.0), which corrects all known anomalies and deficiencies observed in the previous version V5.0S. Also, this includes the validation of the Tb's generated using V6.0, based upon more than two years of on-orbit measurements, to determine the accuracy and stability of the MWR radiometric calibration individually for all 24 channel/beam combinations for the duration of on-orbit operations (~ 2.5 years).

The research started with the on-orbit evaluation of V5.0S using the inter-satellite radiometric calibration (XCAL) with the WindSat satellite radiometer. For this evaluation, which started approximately 6 months after launch, MWR and WindSat observations of clear sky ocean scenes were collocated in 1° latitude/longitude boxes and within a ± 1 hr time window for comparison. The MWR channels were a subset of the WindSat channels, which matched the center frequency and polarizations; but there were significant differences in the earth incidence angles (EIA's).

Therefore, before comparing the observed radiances of these two radiometers, it was necessary to make allowances for the different EIA's used in the measurements. For this purpose, an ocean radiative transfer model (RTM) was run (using environmental parameters from NOAA NCEP Global Data Assimilation System) for both MWR and WS; and theoretical differences for the ocean Tb's at different EIA's were produced. Next, the average difference (for the 1° box) between the observed Tb's were calculated; and then, the radiometric bias was set equal to the double difference of the single differences (observed minus simulated).

Statistics were calculated on the XCAL set of 1° box biases that were sorted by channels and beams and time (5 day averaged time series). Based upon this and other on-orbit measurements, the following V5.0S conclusions were reached: 1) the counts to Tb algorithm exhibited a compressive non-linearity, which yielded a variable radiometric bias that was a function of the scene brightness temperature, 2) there was significant drift in the radiometric calibration over monthly periods, and 3) there were large inter-beam biases, with significant time variability.

The V6.0 counts to Tb algorithm developed a rad_counts linearization procedure, which removed the V5.0S radiometer system non-linearity. Afterwards, all pre-launch radiometric calibration testing was revisited and the analysis performed using linear counts. This resulted in an improved forward radiometer transfer function that significantly reduced the test residuals (measured minus modeled Tb's). Next on-orbit XCAL comparisons with WindSat were used to develop a robust antenna pattern correction algorithm for V6.0. Finally the new V6.0 algorithm was extensively evaluated using about 2.5 years of WindSat XCAL. Based upon this and other on-orbit measurements (e.g., deep space calibration), the following conclusions were reached: 1) all known anomalies for V5.0S were eliminated, 2) the stability of radiometric calibration was improved, but calibration drift for a given beam was not eliminated, 3) there were smaller inter-beam biases, but there remained systematic calibration drifts (±1 K to ± 2 K) over yearly periods, and 4) the dependence of radiometric biases on scene brightness was removed and there were no indications of the nonlinearity exhibited in V5.0S.

6.2 Future Work

6.2.1 MWR Anomalies

For the next counts-to-Tb algorithm, there are several changes recommended, which address minor irregularities that were discovered based upon T/V calibration test and on-orbit measurements.

Careful analysis of the T/V calibration test led to the discovery of an inconsistent behavior of the noise diode deflection for 37 GHz V-pol for 2 of 8 beams. Since the MWR receiver is a time shared between the 8 beams, the noise diode deflection for all the beams should be the same. However, the time series of the noise diode deflection during the T/V calibration test (Fig 6.1.a), shows that the beams #2 & #4 have an offset of 11 and 15 counts respectively (corresponds to ~ 0.5 K). The cause is unknown, but the ad hoc fix is to subtract 11 and 15 counts respectively from these beams. After this adjustment is performed, all beams are grouped within a few counts, which are negligible differences. It is recommended that the next version V7.0 includes this fix.

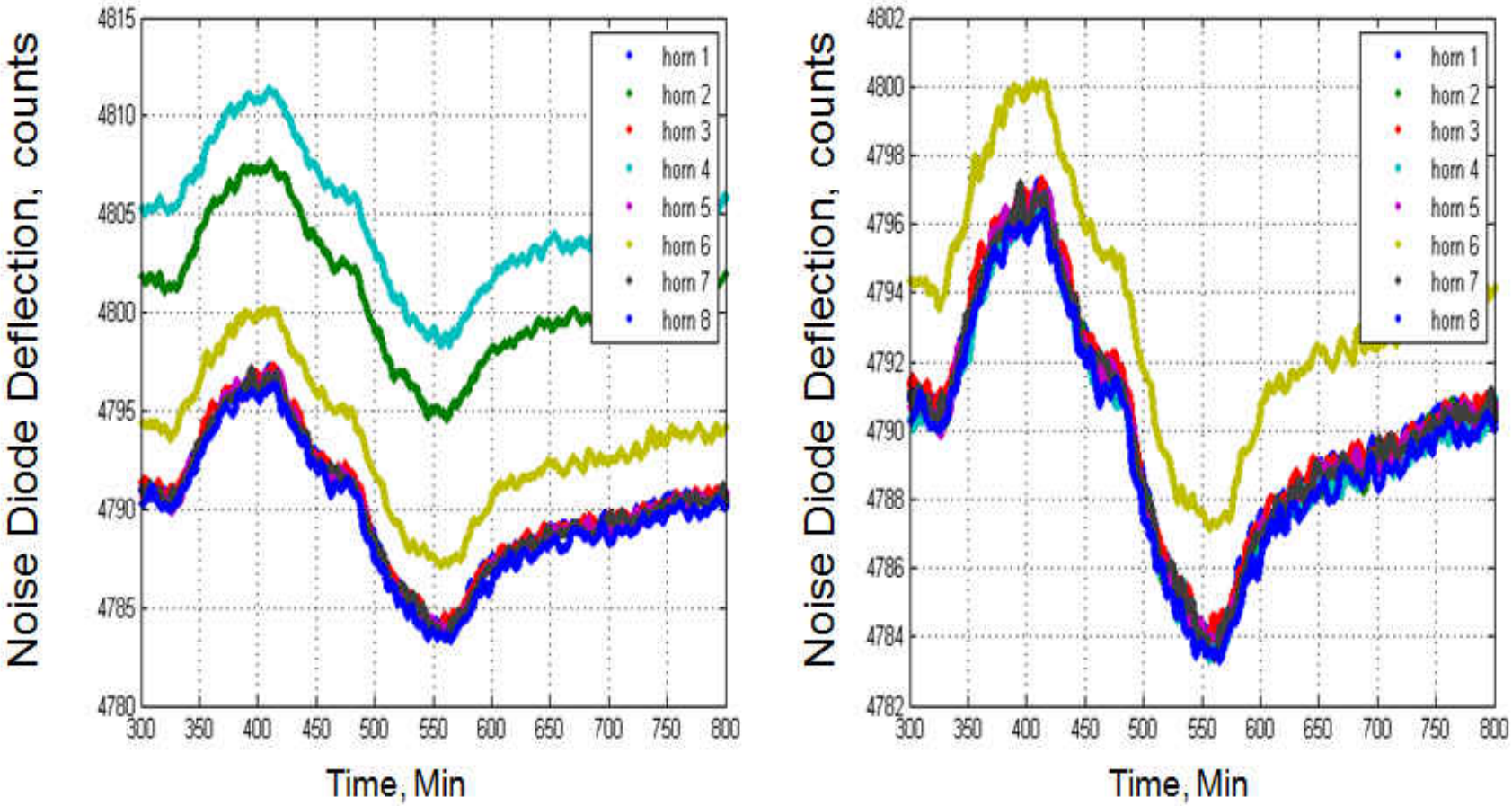

Figure 6-1 Time series of the noise diode deflection for 37GHz V-pol during the TV calibration test for a) before adjusting the noise diode deflection for beam # 2&4, a) after adjusting the noise diode deflection for beam # 2&4. The time is since 06-sep-2009 19:57:32

.

6.2.2 Development of MWR Tb Dataset V7

Since the XCAL DD biases discussed in Chapter 5 are believed to be almost entirely caused by changes in the MWR radiometric calibration, it is recommended that the next generation counts to Tb algorithm V7.0 be normalized to WindSat to remove the slowly changing XCAL 5 day double difference biases of V6.0. To limit the changes to the slowly changing mean values, a triangular moving average will be applied on the 5 day average of the DD time series to smooth the correction. An example of the time series and the smoothed data are presented in Fig 6.2 for 23GHz for 8 beams, where the red color is the time series of the DD, and the black color is the smoothed data. The results of this correction (after normalizing to WindSat) are shown in Fig. 6.3 as a new time series of the 5 day average DD. From this figure, we can see that this technique is very effective in removing the slowly changing biases, and it totally eliminates inter-beam biases for all channels.

Results for channel 37GHz H-pol are presented in Appendix-H.

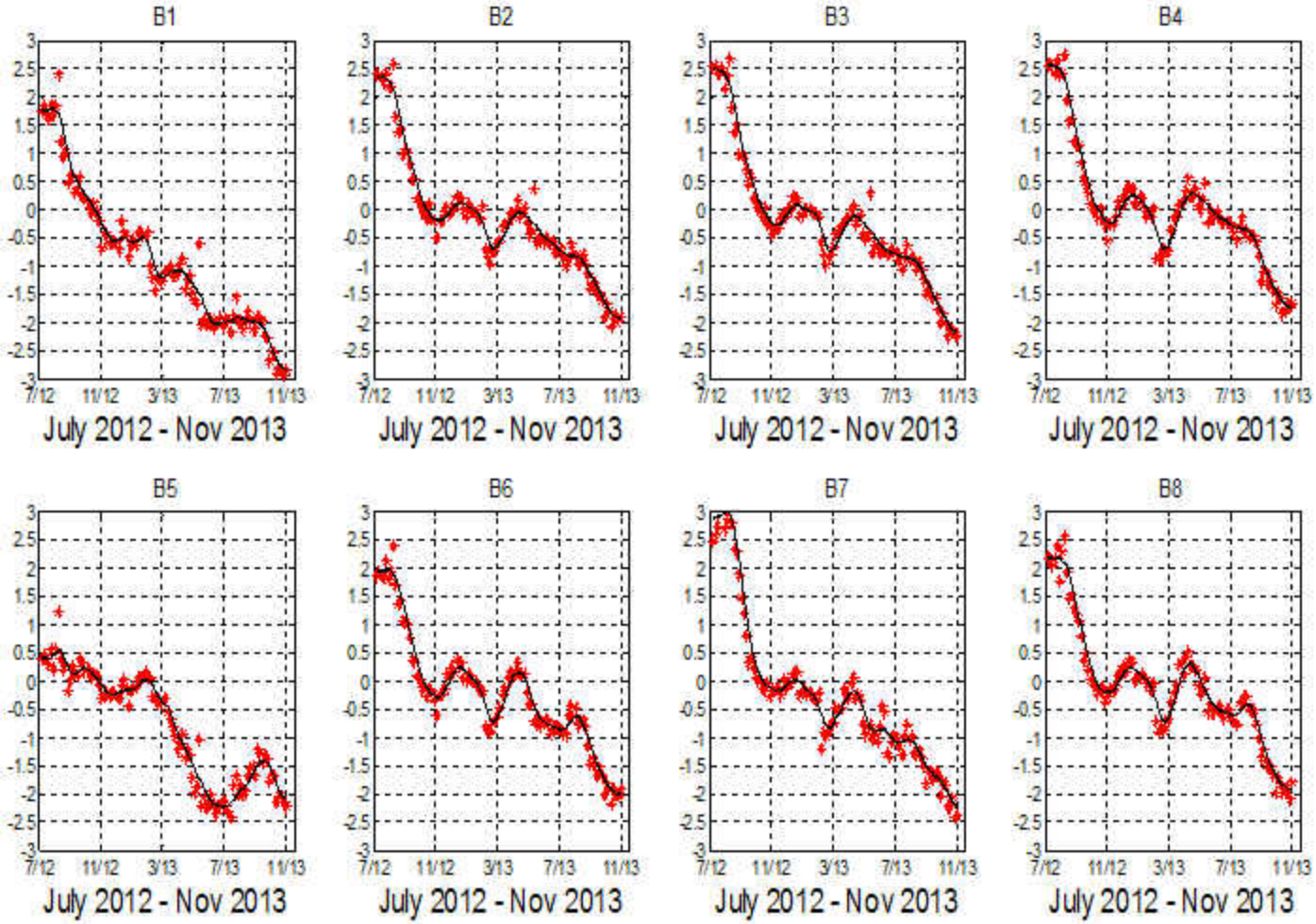

Figure 6-2 V6.0 DD biases (MWR-WS) for 23GHz for time period July 2012 – Nov 2013

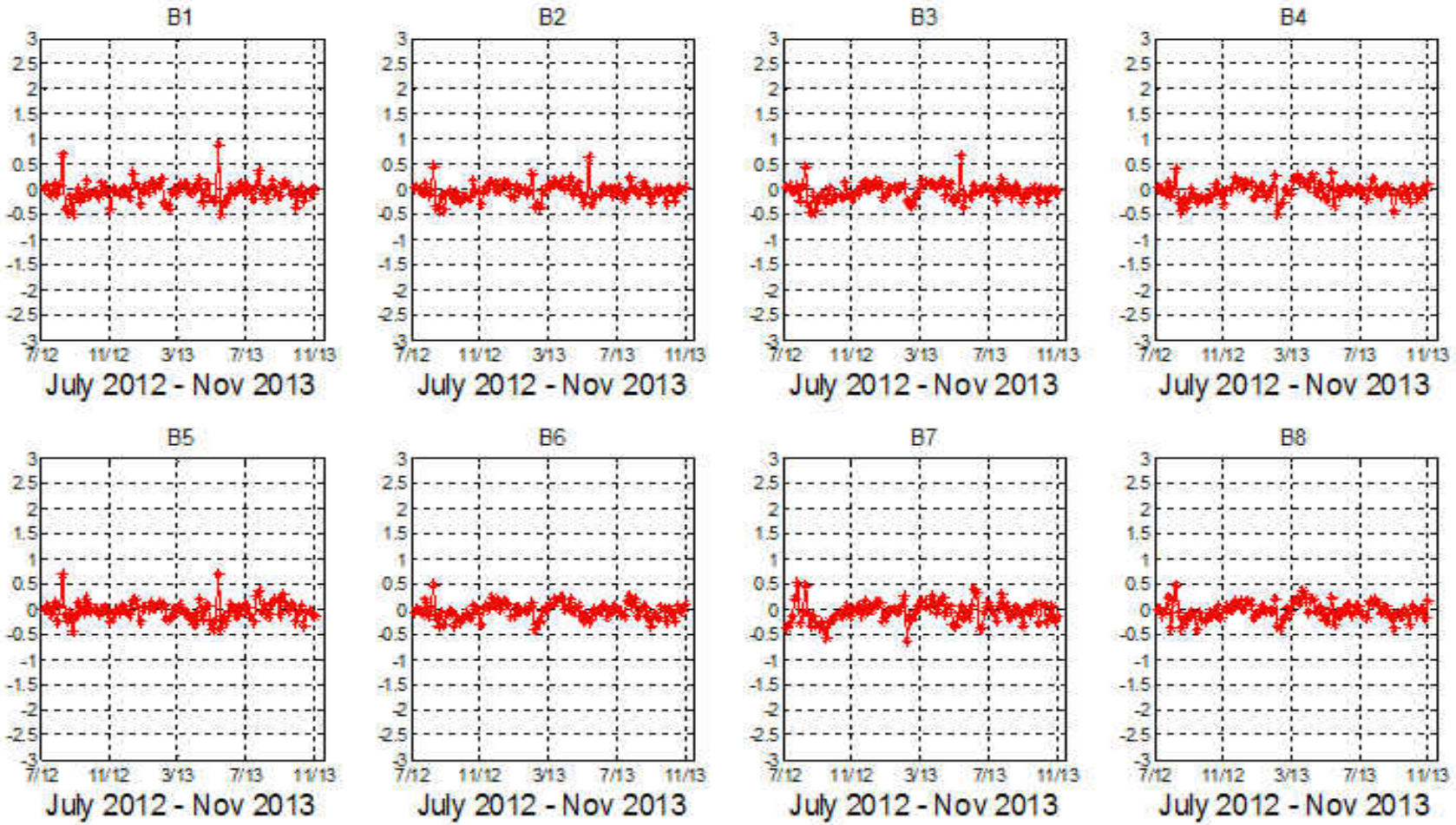

Figure 6-3 V7 adjusted DD biases (MWR-WS) for 23GHz for time period July 2012 – Nov 2013

APPENDIX A
MWR INVERSE MODEL COEFFICIENTS (V5.0S)

In MWR counts-to-Tb algorithm version 5.0S, the regression model is tuned up using collocated WS and MWR observations. Because the MWR and WS have different EIA, a Radiative transfer model was used to translate Ws Tb's to corresponding incident angle of individual MWR beams. the coefficients in (Eq. 3.1) were derived from the on-orbit XCAL data. The WindsSat Tb's adjusted to the MWR EIA's were used in the equation to obtain the regression coefficients b1 through b5 for each channel each horn and are tabulated below:

Table A-1 Channel 36.5 GHz, Vertical polarization

Horn #	B1	B2	B3	B4	B5
1	-51.632418002728194	2.151260529101236	-9.348280894604559e-04	-0.011960737938107	-0.646326514915267
2	-5.098274451922471e+02	5.792868675746081	-0.007623334011861	-0.155467385418551	-0.628202957435299
3	-1.617618203245264e+02	2.992715963981955	-0.002668043434178	0.013827018575412	-0.628440406282809
4	-1.468017059179357e+02	2.882980872823312	-0.001984863634392	-0.078508168267743	-0.683033344756797
5	-2.434332028131630e+02	3.559590094577231	-0.003952189785950	-0.043761179762434	-0.511039932790668
6	-2.271820755429545e+02	3.407004642085678	-0.003352775390451	-0.076899801997989	-0.536026973262781
7	-1.644264635544842e+02	2.937568433972628	-0.002659715213569	-0.184041152366778	-0.393606158218554
8	-2.433544099976945e+02	3.566165069863248	-0.003651835414043	-0.103285358104578	-0.526141914129374

Table A-2 Channel 36.5 GHz, Horizontal polarization

Horn #	B1	B2	B3	B4	B5
1	-1.006995204475407e+02	3.242294449131145	-0.004005094589420	0.020727030919678	-0.820386098474569
2	-1.131137282387518e+02	3.521678723840673	0.004377224544759	-0.216184045189491	-0.681992431814899
3	-31.085239280190370	2.479377275918045	-0.002155869308547	0.059963878631665	-0.816873735276818
4	-5.484395957297707	2.476219887621540	-0.002110201106920	-0.192801169106149	-0.669003180435575
5	-77.651754836155650	2.776836513101550	-0.002874769348302	0.185268211741363	-0.891778052317215
6	-22.987960915918550	2.588206691902331	-0.002272201898491	-0.289431447995206	-0.583972145369877
7	-1.442717177271959e+02	3.468538157323713	-0.004289888076808	0.142435796600126	-0.916956306639033
8	-44.276720850041090	2.744584532012874	-0.002593814665025	-0.261658562575962	-0.607476416583968

Table A-3 Channel 23.8 GHz, Horizontal polarization

Horn #	B1	B2	B3	B4	B5
1	-1.893790365375965	1.382596373842289	5.416265027122371e-04	0.317503847726502	-0.805407242211549
2	-76.404219280413670	1.806342217412257	-3.948624500746702e-04	0.063787416324712	-0.439534106963413
3	-33.628013894112830	1.589936133143321	-1.522831659766910e-04	0.212333613809162	-0.587045971853559
4	-15.382361138133993	1.362101423029914	1.542278870371555e-04	0.154813856672028	-0.457739132282796
5	-22.804115269682153	1.589112728412167	-2.184125410002660e-04	0.180359419461031	-0.578004809294857
6	-14.591737887138047	1.403989251863432	1.209084357883729e-04	0.173833008714543	-0.516842142948622
7	-99.253149156408850	1.710178715845812	-2.355368320401603e-04	-0.423876139254538	0.144745896538417
8	-11.493797162854282	1.399323376584104	7.484693118049984e-05	0.184490428741517	-0.520544958758505

APPENDIX B
SMEAR CORRECTION

This Appendix is from CONAE and the reference #11.

Mathematical Approach to Beam Coupling

The following equation (Eq. B-1) establishes the relationship between digital counts at the output of MWR, $\widetilde{C}$, which are assumed coupled, and the corresponding digital counts without coupling (theoretical), *C*. Both vectors C and $\widetilde{C}$, represent the information organized in a temporarily increasing order, according to the sampling sequence for all the feed-horns.

$$\begin{bmatrix} \vdots \\ \widetilde{C}_{\mathrm{E}}(k) \\ \widetilde{C}_{\mathrm{E}}(k+1) \\ \widetilde{C}_{\mathrm{E}}(k+2) \\ \widetilde{C}_{\mathrm{E}}(k+3) \\ \widetilde{C}_{\mathrm{E}}(k+4) \\ \vdots \end{bmatrix} = \frac{1}{8} \begin{bmatrix} \ddots & \ddots & \ddots & \ddots & \ddots & \ddots & \ddots & \ddots \\ \ddots & a & 8-a & 0 & 0 & 0 & 0 & \ddots \\ \ddots & 0 & a & 8-a & 0 & 0 & 0 & \ddots \\ \ddots & 0 & 0 & a & 8-a & 0 & 0 & \ddots \\ \ddots & 0 & 0 & 0 & a & 8-a & 0 & \ddots \\ \ddots & 0 & 0 & 0 & 0 & a & 8-a & \ddots \\ \ddots & \ddots & \ddots & \ddots & \ddots & \ddots & \ddots & \ddots \end{bmatrix} \begin{bmatrix} \vdots \\ C_{\mathrm{E}}(k-1) \\ C_{\mathrm{E}}(k) \\ C_{\mathrm{E}}(k+1) \\ C_{\mathrm{E}}(k+2) \\ C_{\mathrm{E}}(k+3) \\ C_{\mathrm{E}}(k+4) \\ \vdots \end{bmatrix} \qquad \text{(B-1)}$$

where the subscript E defines the 3 MWR states: Antenna, Antenna + Noise and Reference Load.

The parameter *a* in Eq. B-1 is the contribution from the preceding count *C*, with values $[0,..,8]$. From the eight analogic measurements (for every single state E) that are later integrated, *a* represents the number of integrations from the previous feed-horn that are "coupled" to the present feed-horn. The term coupling is used in this research due to the fact that the system of equations that represent the problem are mathematically coupled and can be solved (or de-coupled) in a recursive way, if only one measurement is not smeared (is not anomalous). In summary, $\widetilde{C}(j) = C(j)$ for some value *j* is needed. But in this problem, all the measurements

present the smear effect. Nonetheless, the symmetry of the problem allows a solution to be found.

Equation B-1 can be rewritten in terms of coupling percentage as follows:

$$\begin{bmatrix} \vdots \\ \widetilde{C}_{\mathrm{E}}(k) \\ \widetilde{C}_{\mathrm{E}}(k+1) \\ \widetilde{C}_{\mathrm{E}}(k+2) \\ \widetilde{C}_{\mathrm{E}}(k+3) \\ \widetilde{C}_{\mathrm{E}}(k+4) \\ \vdots \end{bmatrix} = \begin{bmatrix} \ddots & \ddots & \ddots & \ddots & \ddots & \ddots & \ddots & \ddots \\ \ddots & p & 1-p & 0 & 0 & 0 & 0 & \ddots \\ \ddots & 0 & p & 1-p & 0 & 0 & 0 & \ddots \\ \ddots & 0 & 0 & p & 1-p & 0 & 0 & \ddots \\ \ddots & 0 & 0 & 0 & p & 1-p & 0 & \ddots \\ \ddots & 0 & 0 & 0 & 0 & p & 1-p & \ddots \\ \ddots & \ddots & \ddots & \ddots & \ddots & \ddots & \ddots & \ddots \end{bmatrix} \begin{bmatrix} \vdots \\ C_{\mathrm{E}}(k-1) \\ C_{\mathrm{E}}(k) \\ C_{\mathrm{E}}(k+1) \\ C_{\mathrm{E}}(k+2) \\ C_{\mathrm{E}}(k+3) \\ C_{\mathrm{E}}(k+4) \\ \vdots \end{bmatrix} \tag{B-2}$$

where p represents the coupling percentage, with values $[0,..,1]$. By simple inspection it can be noted that the matrix that is presented in Eq. B-2 is bi-diagonal (lower diagonal), for this reason its inverse will also be lower triangular. Only p is unknown, and this is due to the fact that the contribution from a previous feed-horn is constant for every feed-horn and channel. This assumption is based on the symmetry of the problem.

Solving the system of equation, leads to:

$$\boxed{C_{\mathrm{E}}(k) = \sum_{i=0}^{\infty} (-1)^i \frac{p^i}{(1-p)^{i+1}} \widetilde{C}_{\mathrm{E}}(k-i) \quad \text{cuando} \quad 0 < p < 1/2} \tag{B-3}$$

The mathematical series presented in Eq. 3, converges if $p < 1/2$.

Error Analysis

To be able to apply the correction presented in the previous section, a cut off of the series is needed, and then analyzed the introduced error. In this way, the truncation error $\Delta C_{\mathrm{E}}{}^{n}$,

introduced in the estimation of C_E, when only the first n terms of the series are considered, can be bounded from above as:

$$\Delta C_E^{\,n} < \begin{cases} \max\{C_E\}\left(\dfrac{p}{1-p}\right)^n & cuando \quad 0 < p < 1/2 \\ \max\{C_E\}\left(\dfrac{1-p}{p}\right)^n & cuando \quad 1/2 < p < 1 \end{cases} \tag{B-4}$$

The terms $\left(\dfrac{p}{1-p}\right)^n$ and $\left(\dfrac{1-p}{p}\right)^n$ in Eq. B-4 are related to the number of n terms needed to limit the error, i.e., the greater the coupling ($p \to 1/2$) the greater the number of terms.

In the case that $p = 1/2$ the error can't be limited, since the series do not converge. But this is not the case of this problem, as is show in the following section.

Determining the Coupling Percentage *p*

Base on the hypothesis presented in previous sections, and assuming $a \in Z$ in Eq. B-1, the values of *p* are:

$$p = a/8 \quad \text{con} \quad a = 1,\ldots,8 \tag{B-5}$$

where, as it is mention before, *a* represents the number of numerical integrations from the previous feed-horn that are coupled with the $8-a$ numerical integrations of the feed-horn of interest.

Through a qualitative analysis of MWR measurements, it was possible to find the possible values, i.e., the possible coupling pairs $(8-a, a)$ are:

$$\begin{aligned}(8,0) &\leftrightarrow \quad p = 0 \\ (7,1) &\leftrightarrow \quad p = 0.125 \\ (6,2) &\leftrightarrow \quad p = 0.25 \\ (5,3) &\leftrightarrow \quad p = 0.375\end{aligned} \tag{B-6}$$

Then the correction presented in Eq. B-3 was applied to the four cases from Eq. B-6 and the results found in the previous section were applied to determine the minimum number of terms (n) needed. Due to the fact that n is p dependent, the determination of this value will be presented after the estimation of p in the following paragraphs.

By inspection, it was determined that $a = 2$ ($p = 0.25$) is not only the best of the four possibilities, presented in Eq. B-6, but also the only one that corrects the problem almost completely.

In the following section the results obtained in the estimation of a and p are presented, analyzing the MWR measurements.

Statistical Estimation of the Coupling Percentage, using On Board Measurements

Before continuing is important to note that, as was expected, the count measurements from the reference load do not showed the anomalous smear effect, due to the fact that the reference is the same for the 8 feed-horns; but this doesn't mean that the issue is not present. For this reason the measurements from the reference load are not analyzed in this section.

Figure B-1 presents an example of the Tb anomalous behavior, that also correspond to an anomalous behavior of the counts Ca and Cn.

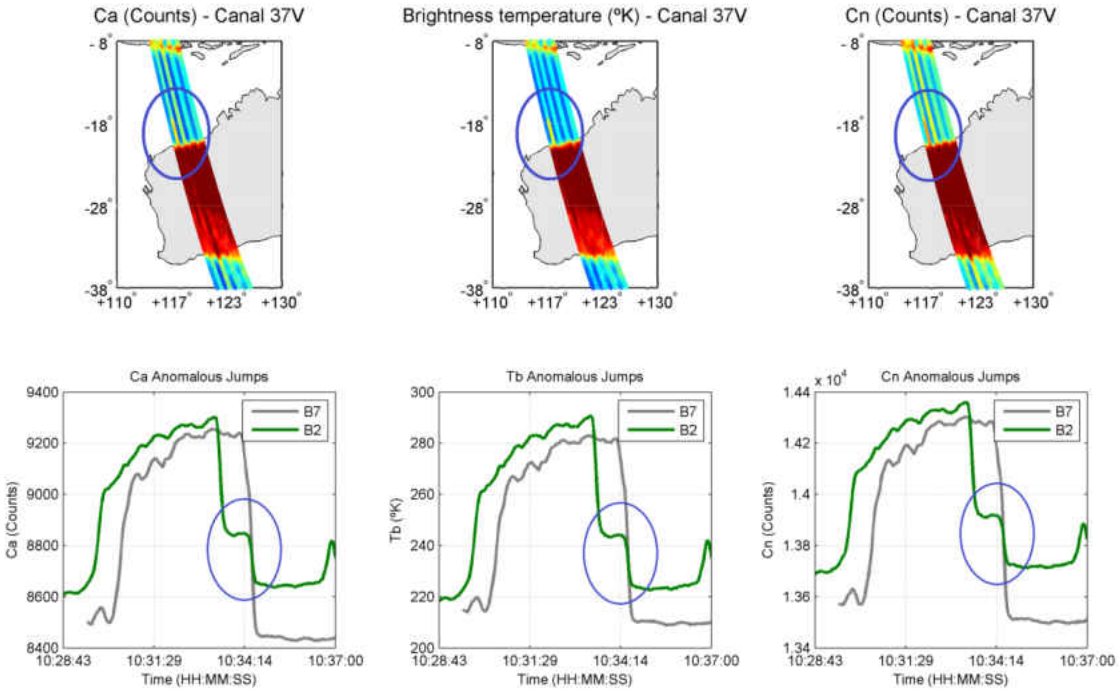

Figure B-1.

One way to estimate the coupling parameters is focus the analysis in the anomalous jumps in Tb, especially in areas close to the coast, and with this pose a relation to be able to determine *p*.

Let analyze that 2 points that are related to the same anomalous jump in times t_1 and t_2, with count values $\widetilde{C}_1$ and $\widetilde{C}_2$, respectably. Figure B-2 shows an example of this, where $\widetilde{Ca}(t)$ is plotted for beam 2 (green) and 7 (grey, for the 37V channel.

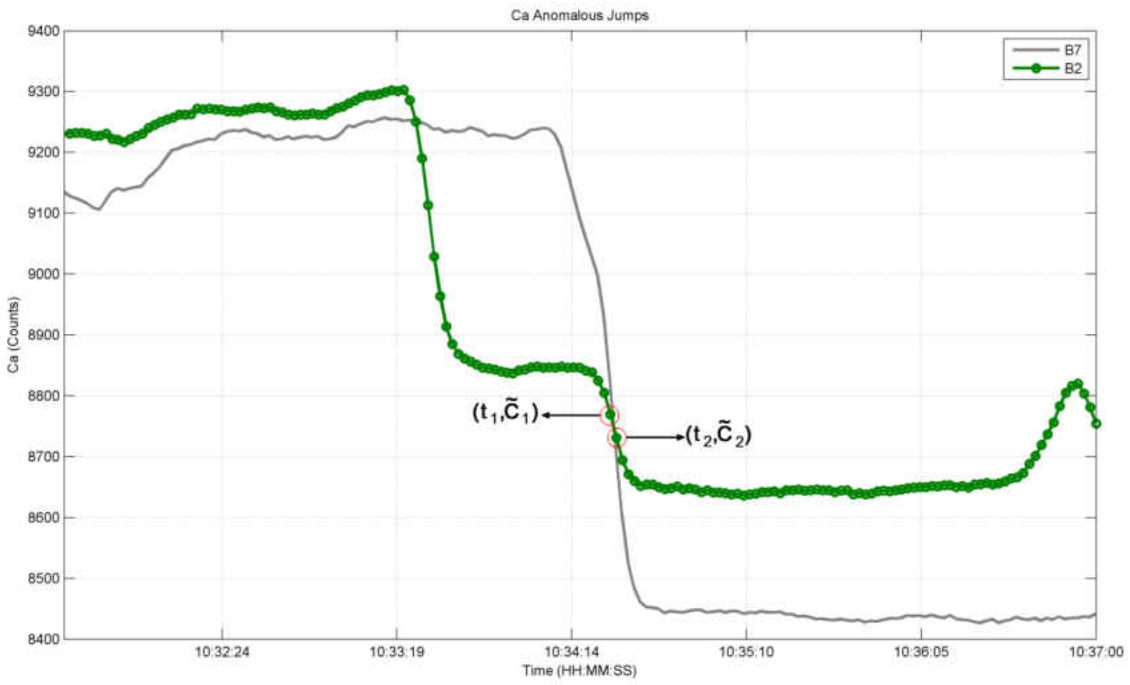

Figure B-2.

If the anomaly wasn't present, then $C_1 \approx C_2$, where C_1 and C_2 are the corrected counts for $\widetilde{C}_1$ and $\widetilde{C}_2$ respectively. To estimate the coupling parameter a it can be assumed that $C_1 = C_2$ and then apply Eq. B-3 to both sides. Solving this equation:

$$\boxed{\sum_{i=0}^{\infty} \gamma^i \left[\widetilde{C}\left(\frac{t_2}{\Delta t} - i \right) - \widetilde{C}\left(\frac{t_1}{\Delta t} - i \right) \right] = 0 \quad \text{con} \quad -1 < \gamma = \frac{p}{p-1} < 0} \tag{B-7}$$

where $\widetilde{C}$ is the same vector that was defined at the beginning of this Appendix in Eq. B-1; and for this reason Δt represents the time between 2 MWR consecutives measurements, i.e., is the 0.24 s integration time. It is important to note that the term in brackets represents the jump in $\widetilde{C}$ between two consecutive measurements for the same feed-horn, for a every i.

Next it's necessary to establish a new truncation error for the series, which results in:

$$\varepsilon^{(k)} < \max\left\{\Delta\tilde{C}\left(i,t_1,t_2\right)\right\}|\gamma|^k \tag{B-8}$$

where $\varepsilon^{(k)}$ represents the error introduced by replacing the series for its first *k* terms (grade $k-1$ polynomial) and $\Delta\widetilde{C}\left(i,t_1,t_2\right)$ is the bracket term in Eq. B-7.

Due to the fact that a jump area is being analyzed, is expected that the $\max\left\{\Delta\widetilde{C}\left(i,t_1,t_2\right)\right\}$ could be replaced by $\widetilde{C}\left(\frac{t_2}{\Delta t}-j\right)-\widetilde{C}\left(\frac{t_1}{\Delta t}-j\right)$ for $j=i+1$ or $j=i$, since it was hypothesized that the anomalous jump is due to a jump in the previous measurement feed-horn.

Analyzing several cases, it was established that $k=9$, and then the estimation of *p* is reduced to solving the root of $\gamma_0 \in \Re$ such that $-1<\gamma_0<0$, in each of the 8th grade polynomials given by the first 9 terms of Eq. B-7 and the corresponding consecutives pair of points of an anomalous point.

Analyzing the behavior of $\widetilde{C}$ near the anomalous jumps, it was determined the relations between the numerical derivatives of the feed-horns measurements and its corresponding previous measurement feed-horn for the 3 MWR channels. Taking into account this criteria a search algorithm was implemented to the 200 orbits, differentiating between channel and feed-horns.

Due to the errors introduced in the estimation of *p*, it is inconvenient to use an arithmetic estimator for *p*, and instead the statistic mode was used.

The next figures present the results obtained for the coupling percentage *p* and its corresponding *a* parameter.

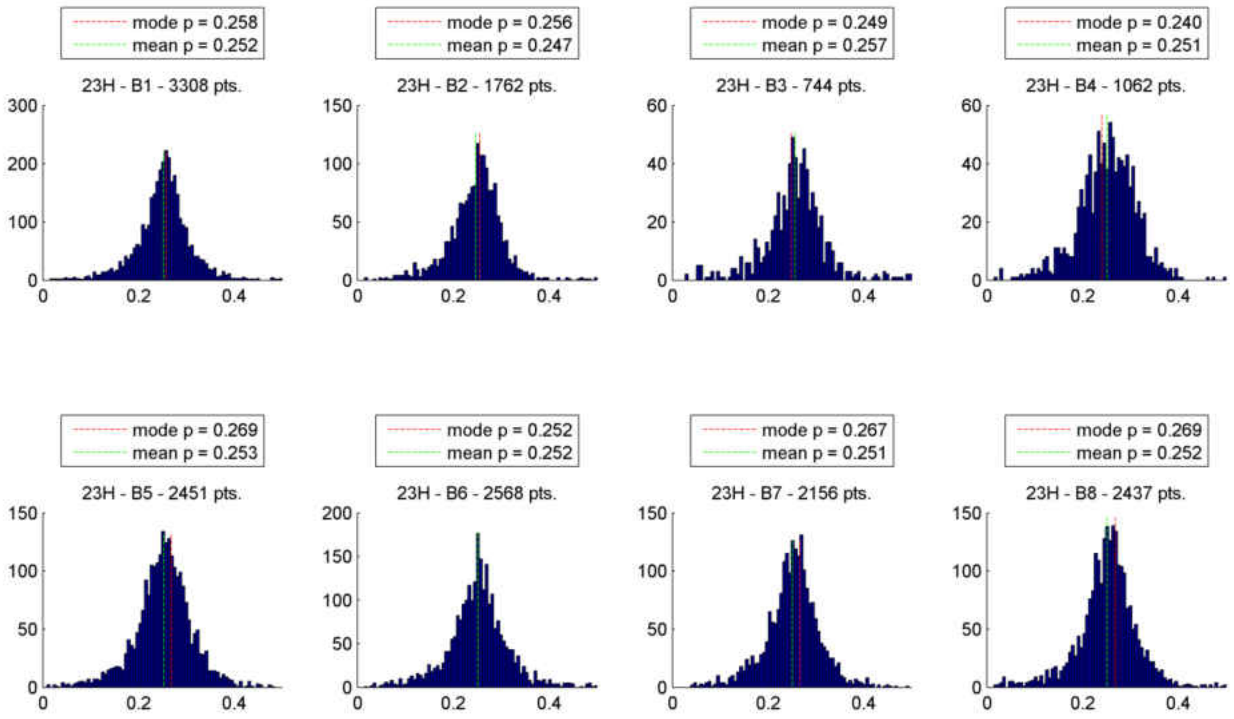

Figure B-3.

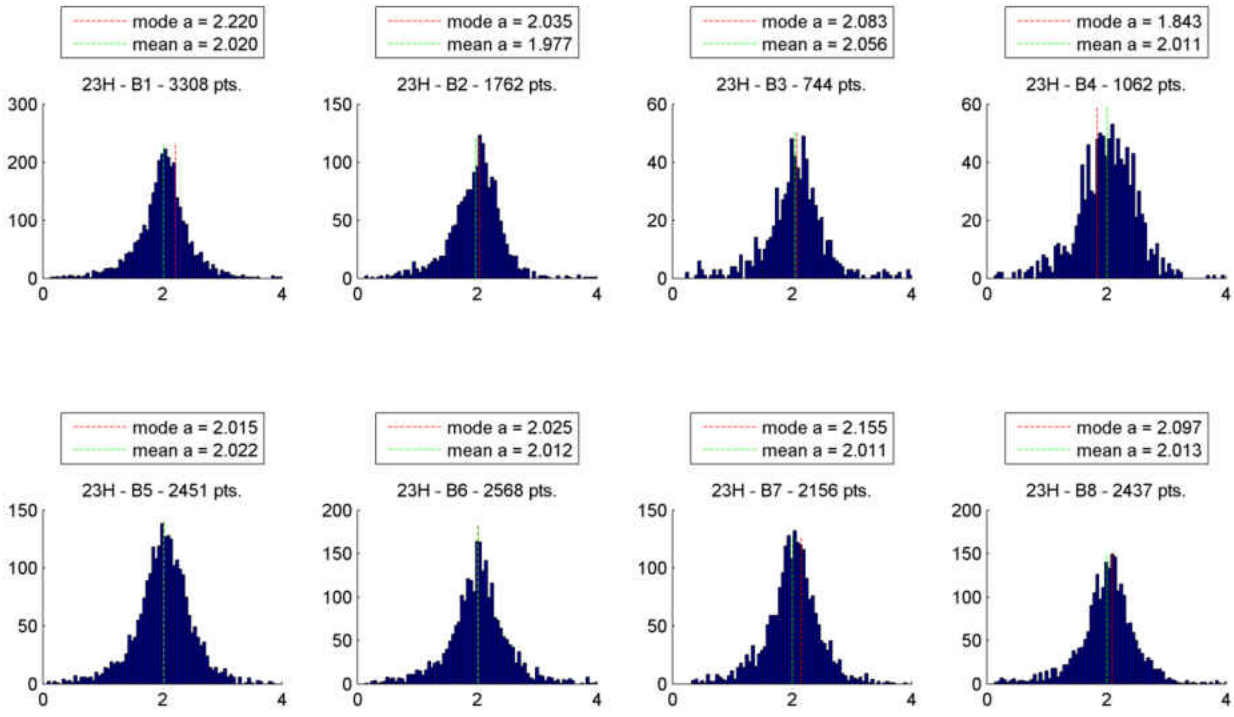

Figure B-4.

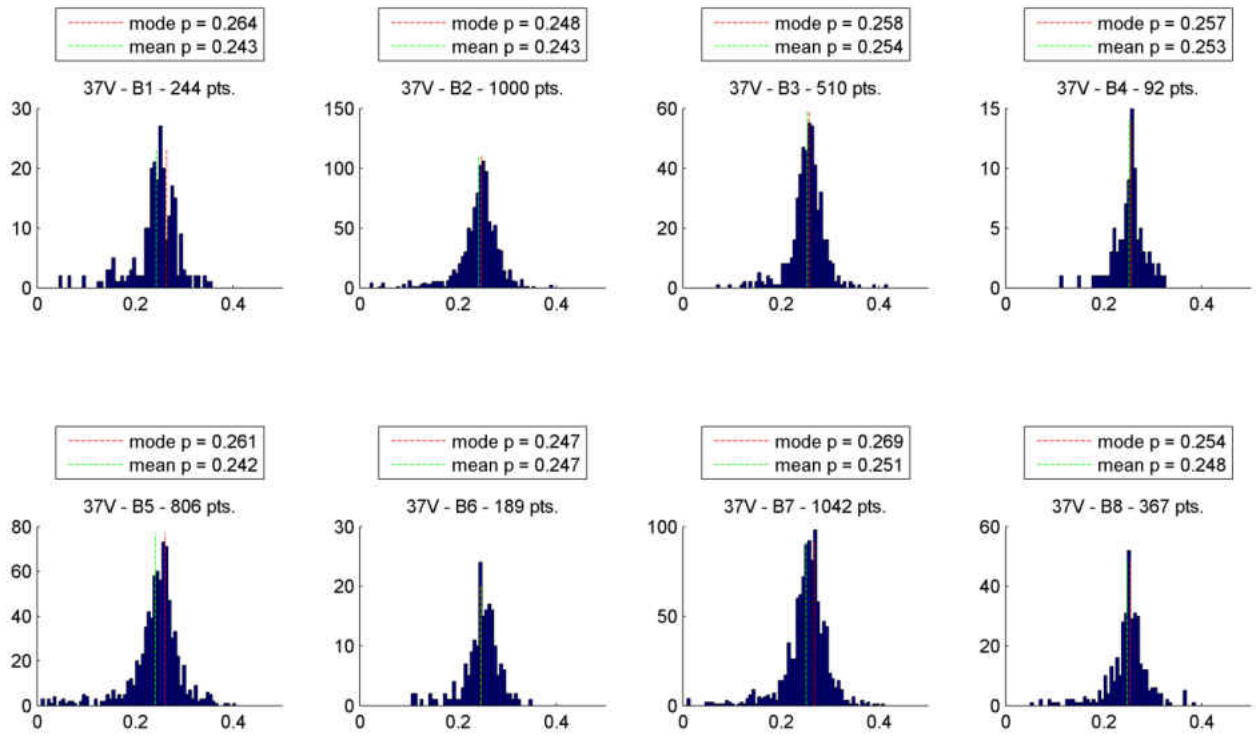

Figure B-5.

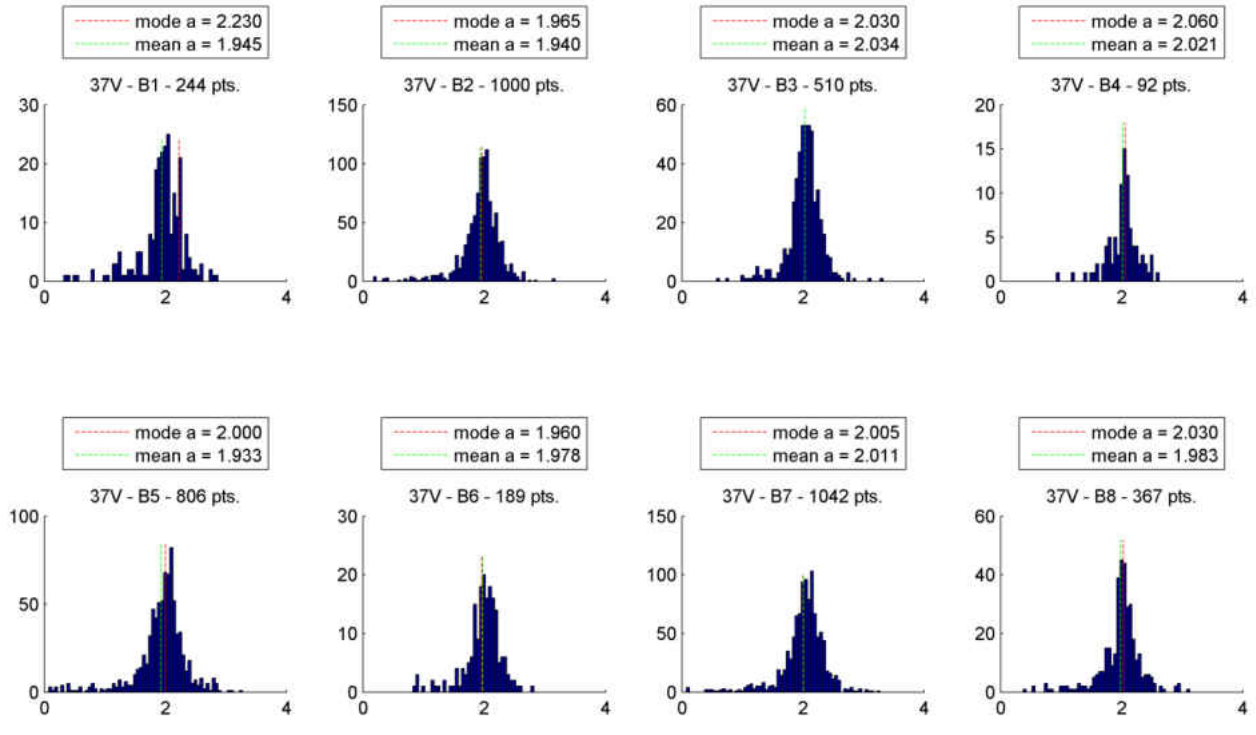

Figure B-6.

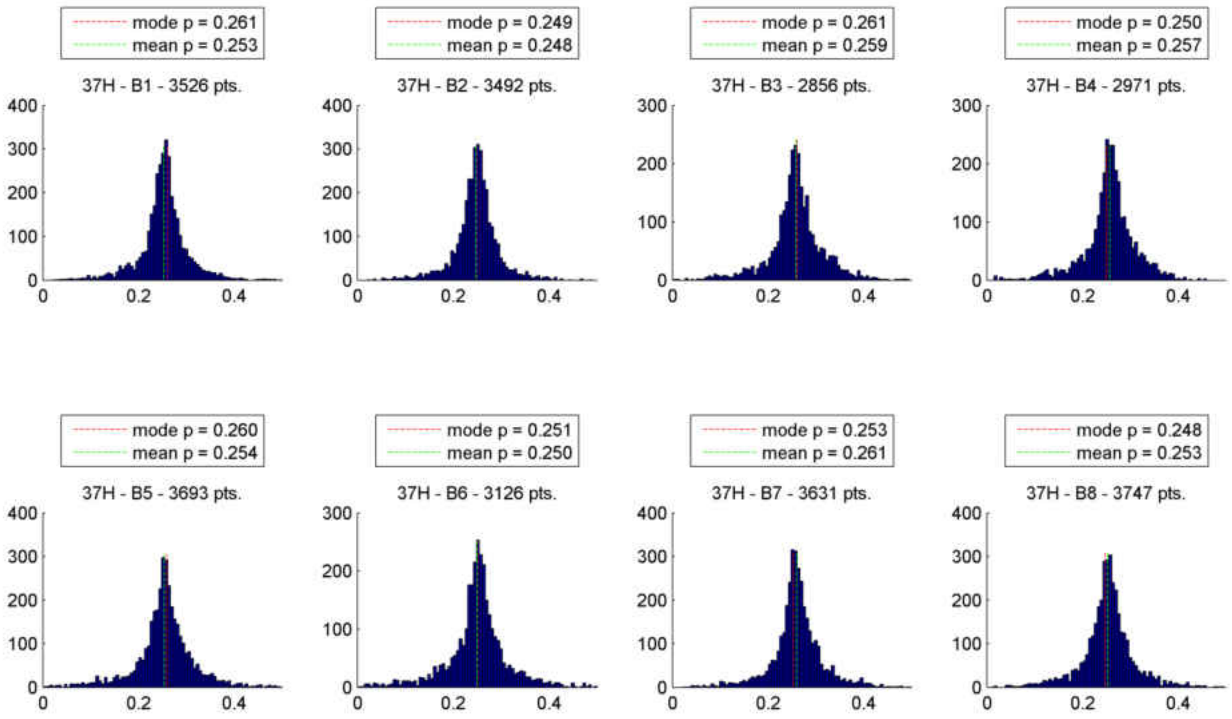

Figure B-7.

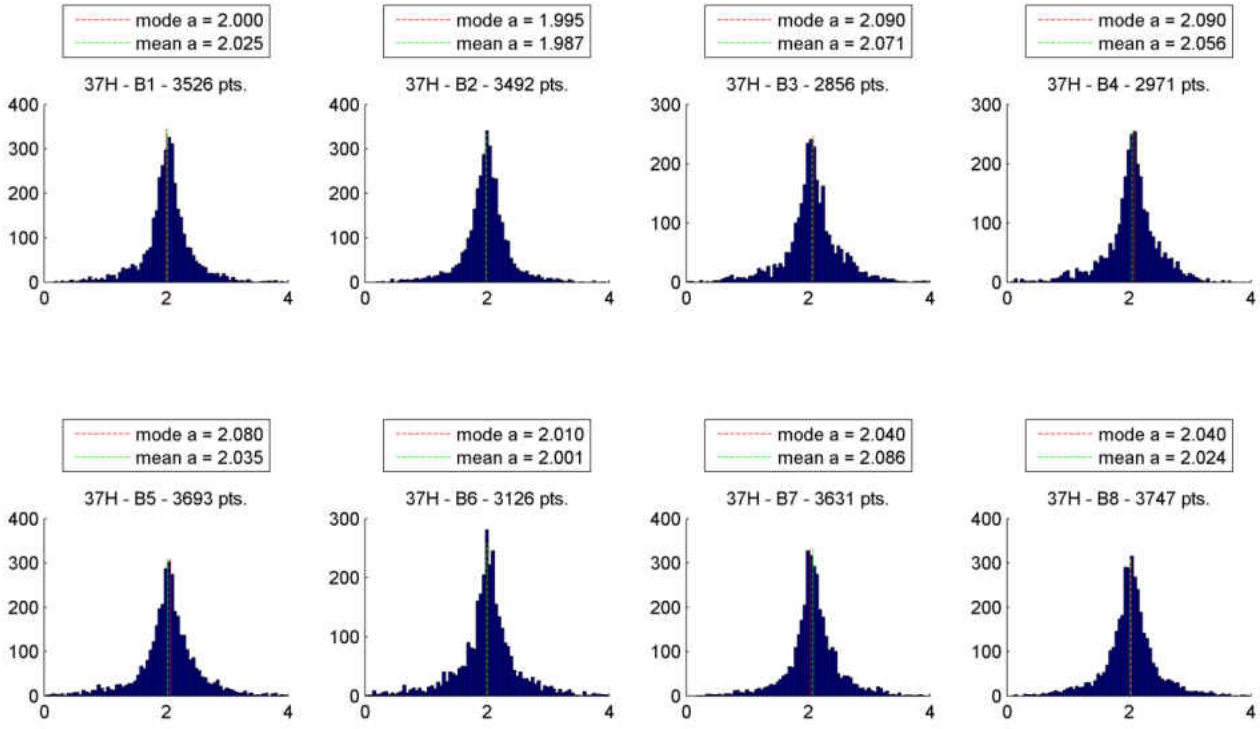

Figure B-8.

The results presented a good agreement with the value $p = 0.25$ ($a = 2$), establish by inspection but justified by the hypothesis. Although the estimation method requires improvement or a more efficient way of estimating p, the plots from figures B-3 to B-8 showed a good symmetry, substantiated in the similarities between the statistical mode and arithmetic mean.

In the following figures, results considering the data for all the 8 feed-horns together are presented.

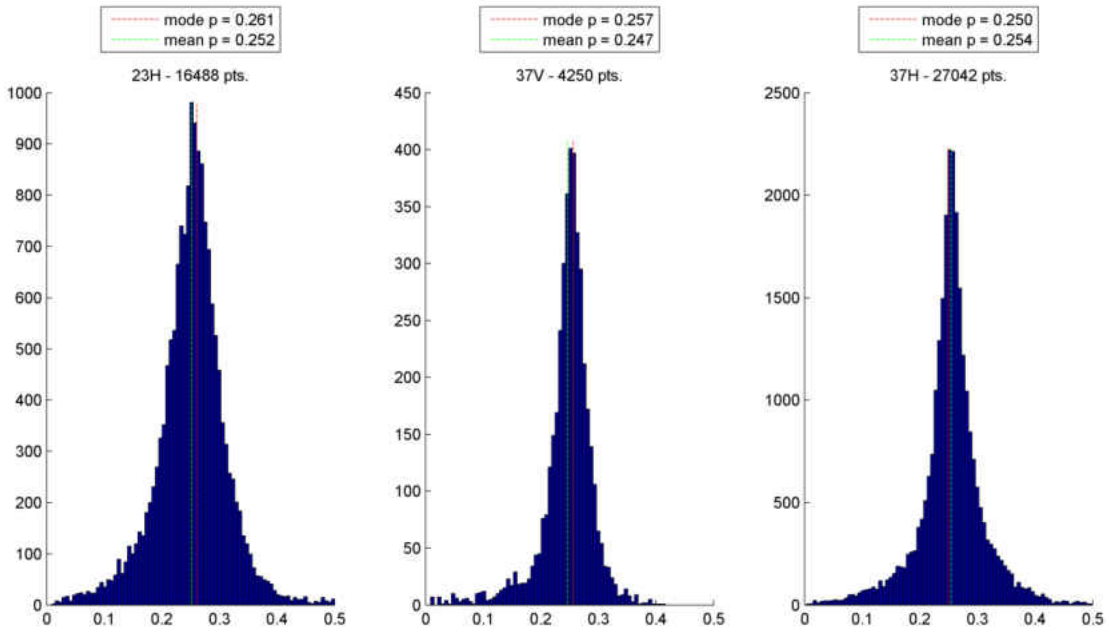

Figure B-9.

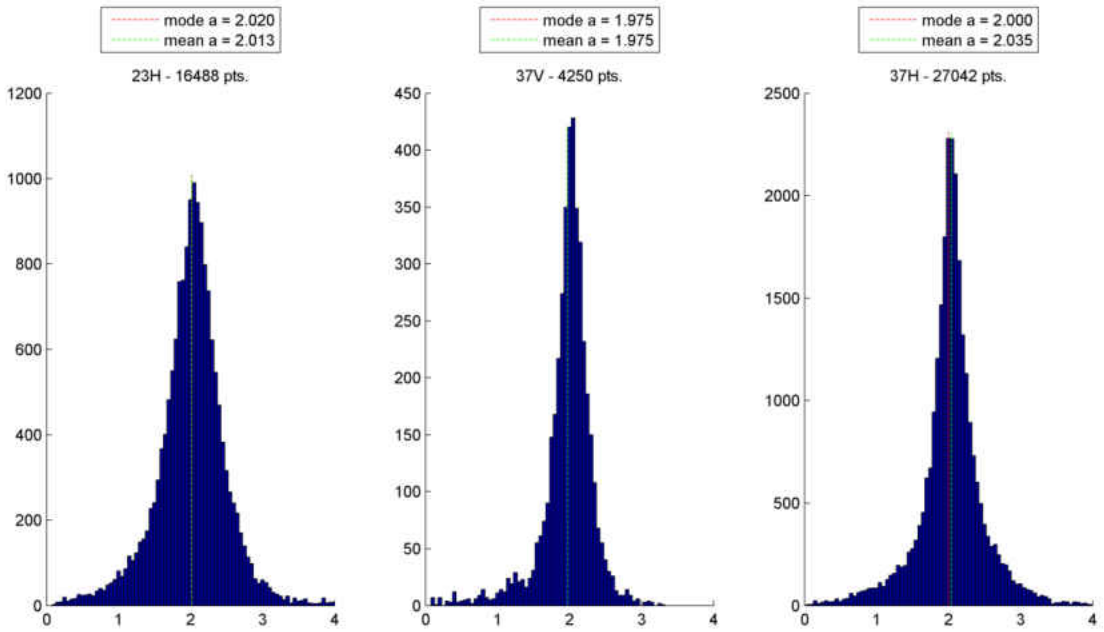

Figure B-10.

In the following section it was assumed a constant p value for each feed-horn and the 3 channels, and equal to 0.25.

Truncation Error and its Effect in Tb

Based on the explanation of the truncation error, presented in previous sections, introduced in the implementation of Eq. B-3, it was necessary to determine the minimum number of terms (n) to limit this error. It was then an error propagation was implemented, considering the calibration equation developed by CFRSL, which relates digital counts and its corresponding brightness temperature.

The next three figures show the worst cases from the 200 orbits of MWR data available at the time.

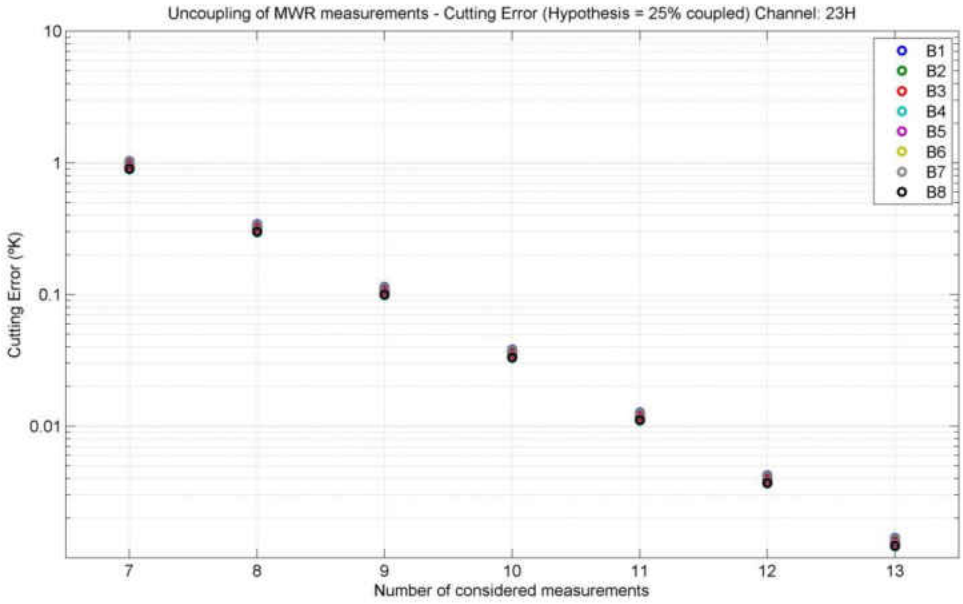

Figure B-11.

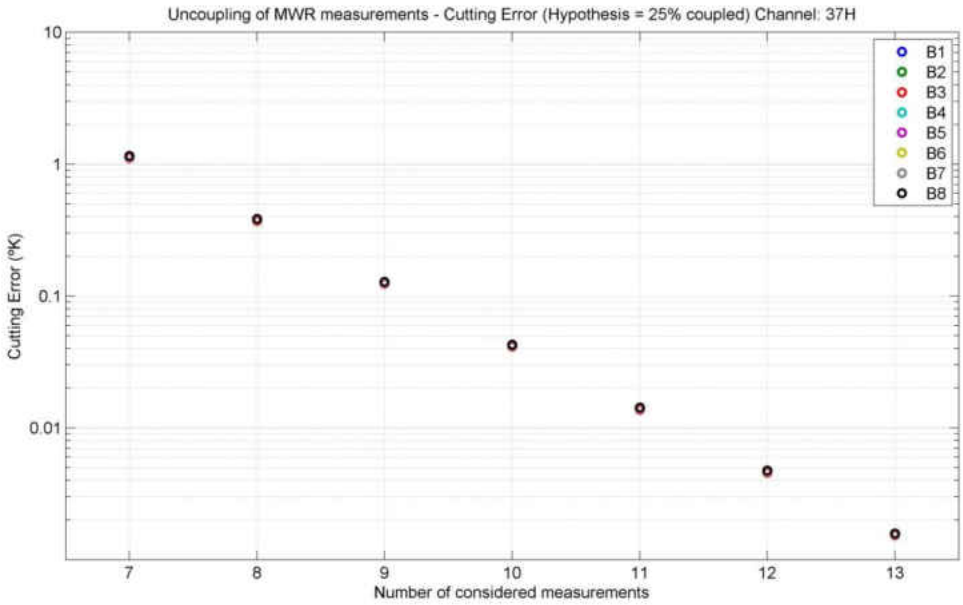

Figure B-12.

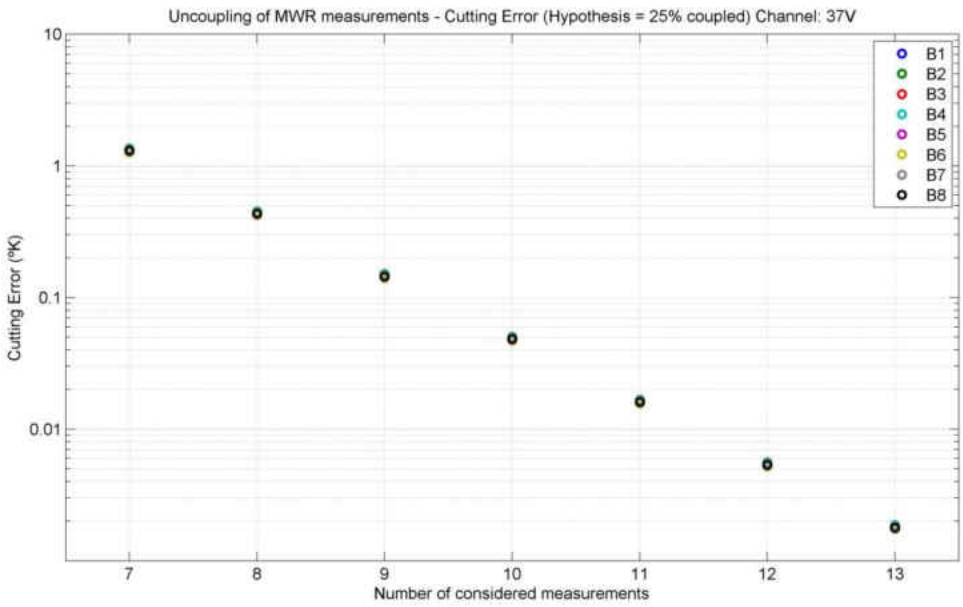

Figure B-13.

From this results it can be noted that it is enough to consider the first 10 terms in the series on Eq. B-3, to introduce then a cut off error less than 0.1K, in the decoupling process.

APPENDIX C
MWR COUNTS TO TB ALGORITHM MATLAB CODE

```
%% CONAE L1A to CFRSL L1 conversion V5.0S

% sayak k biswas, 08/26/2011
% sayak.nitc@gmail.com
% V2 - 09/01/2011 - with new regression based coefficients
% new coeff file -> MWR_coeff_v2.mat
% V2.1 - 09/04/2011 - bias correction added (slope offset correction)
%MWR_bias_v1.mat
% corrected the length of Lat, Lon and EIA fields - 09/13/2011
% V2.2 - 10/13/2011 - added new values of slope offset (MWR_bias_v2.mat )
% further LAT, LON length correction

%V3.0 - 11/23/2011 - added counts in the structure
%V4.0 - 01/03/2012 - new calibration based on post-launch regression
%                  - slope  = 0 ; offset = 0 (MWR_bias_v4.mat)
%                  - cal files used: MWR_coeff_v4.mat, MWR_bias_v4.mat
%% V6.0 11/19/13
% Modified by Zoubair Ghazi
% Linearition, smoothing average, switch matrix coefficients. and APC
% coefficients were performed




%%%%%%%%%%%%%%%%%%%%%%%%%%%%%%%%%%%%%%%%%%%%%%%%%%%%%%%%%%%%%%%%%%%%%%%%%%%%%%%
   clear all;
% clc;
date_start='20130622'; %starting date
date_stop='20130629';    % stop date
for m=str2double(date_start):str2double(date_stop)
%     date_str = '2011112'; % all Oct / 3rd Oct to 7th Oct
    date_str = num2str(m);
    l1dir = 'Z:/MWR/MWR_Data/L1A';
    l2dir = 'Z:/MWR/MWR_Data/L1B';
    opdir =
'C:\Users\zoubair\Desktop\Research\Dissertation\smear_effect\data\smear'; %
output directory for matlab files

    s = dir([ l1dir '/EO_' date_str '*_CUSS_SACD_MWR_L1A_SCI*' ]);
    load MWR_bias_v6_beta3.mat bias;% loading bias coefficients - APC
Correction
    load MWR_coeff_v6_beta3.mat coeff;% loading switch matrix coefficients


    for k = 1:length(s)
        l1name = s(k).name;
        s2 = dir([ l2dir '/' l1name(1:18) '*L1B_SCI*']); % compare all three
fields hh:mm:ss
        if isempty(s2)== 0
            tic
            l2name = s2.name;
%             filename = [ l1dir '/' l1name ];
%             filenameb = [ l2dir '/' l2name ];
            filename = [ l1dir '/' l1name '/data/' l1name ];
            filenameb = [ l2dir '/' l2name '/data/' l2name ];
```

```
%              filename = [ l1dir '/' l1name '/' l1name ];
%             filenameb = [ l2dir '/' l2name '/' l2name ];
            date_str = [l1name(4:7) '-' l1name(8:9) '-' l1name(10:11)];
            doy = datenum(date_str) - datenum('2014-01-00');% change the
year(2012) to a new year that needs to be processed(for example datenum(2013-
01-00))
            doy_str = num2str(doy,'%.3d');
           %% Information about orbits
            Orbit_Number = double(hdf5read(filename,'/Global
Metadata/Acquisition/','Orbit Number')); %Orbit Number
            Cycle_Number = double(hdf5read(filename,'/Global
Metadata/Acquisition/','Cycle Number')); %Cycle Number
            %% output directories

            opname = [opdir '/Q' l1name(4:7) doy_str l1name(13:18) '_CN_'
num2str(Cycle_Number) '_ON_' num2str(Orbit_Number) '_MWR_L1_V6.0_beta3.mat'];


%%%%%%%%%%%%%%%%%%%%%%%%%%%%%%%%%%%%%%%%%%%%%%%%%%%%%%%%%%%%%%%%%%%%%%%%%%%%

%%%%%%%%%%%%%%%%%%%%%%%%%%%%%%%%%%%%%%%%%%%%%%%%%%%%%%%%%%%%%%%%%%%%%%%%%%%%
            %% Reference Load Temperature (from MWR telemetry)

            To36v = double(mean([hdf5read(filename,'/Converted
Telemetry/mwr_hkp_tm_t09') hdf5read(filename,'/Converted
Telemetry/mwr_hkp_tm_t10')],2))+273.15; % ref load 36 v pol
            %MT_9                                                %MT_10
            To36h = double(mean([hdf5read(filename,'/Converted
Telemetry/mwr_hkp_tm_t23') hdf5read(filename,'/Converted
Telemetry/mwr_hkp_tm_t24')],2))+273.15; % ref load 36 h pol
            %MT_23           %MT_24
            To23h = double(mean([hdf5read(filename,'/Converted
Telemetry/mwr_hkp_tm_t11') hdf5read(filename,'/Converted
Telemetry/mwr_hkp_tm_t12')],2))+273.15; % ref load 23 h pol
            %MT_11           %MT_12

            %% Read Front-end temperatures
            % 23H switches
            T4 = double(hdf5read(filename,'/Converted
Telemetry/mwr_hkp_tm_t04')+273.15); %L23-1
            T5 = double(hdf5read(filename,'/Converted
Telemetry/mwr_hkp_tm_t05')+273.15); %L23-2
            T6 = double(hdf5read(filename,'/Converted
Telemetry/mwr_hkp_tm_t06')+273.15); %L23-3
            T7 = double(hdf5read(filename,'/Converted
Telemetry/mwr_hkp_tm_t07')+273.15); %L23-4 (horn#2 & #4)
            T8 = double(hdf5read(filename,'/Converted
Telemetry/mwr_hkp_tm_t08')+273.15); %L23-5 (horn#6 & #8)
            T33 = double(hdf5read(filename,'/Converted
Telemetry/mwr_hkp_tm_t33')+273.15); %L23-6 (horn#1 & #3)
            T34 = double(hdf5read(filename,'/Converted
Telemetry/mwr_hkp_tm_t34')+273.15); %L23-7 (horn#5 & #7)
            % 36V switches
            T35 = double(hdf5read(filename,'/Converted
Telemetry/mwr_hkp_tm_t35')+273.15); %L36V-1
```

```
            T36 = double(hdf5read(filename,'/Converted
Telemetry/mwr_hkp_tm_t36')+273.15); %L36V-2
            T37 = double(hdf5read(filename,'/Converted
Telemetry/mwr_hkp_tm_t37')+273.15); %L36V-3
            T38 = double(hdf5read(filename,'/Converted
Telemetry/mwr_hkp_tm_t38')+273.15); %L36V-4 (horn#6 & #8)
            T39 = double(hdf5read(filename,'/Converted
Telemetry/mwr_hkp_tm_t39')+273.15); %L36V-5 (horn#2 & #4)
            T40 = double(hdf5read(filename,'/Converted
Telemetry/mwr_hkp_tm_t40')+273.15); %L36V-6 (horn#5 & #7)
            T41 = double(hdf5read(filename,'/Converted
Telemetry/mwr_hkp_tm_t41')+273.15); %L36V-7 (horn#1 & #3)
            % 36H switches
            T42 = double(hdf5read(filename,'/Converted
Telemetry/mwr_hkp_tm_t42')+273.15); %L36H-1
            T43 = double(hdf5read(filename,'/Converted
Telemetry/mwr_hkp_tm_t43')+273.15); %L36H-2
            T44 = double(hdf5read(filename,'/Converted
Telemetry/mwr_hkp_tm_t44')+273.15); %L36H-3
            T46 = double(hdf5read(filename,'/Converted
Telemetry/mwr_hkp_tm_t46')+273.15); %L36H-5 (horn#6 & #8)
            T45 = double(hdf5read(filename,'/Converted
Telemetry/mwr_hkp_tm_t45')+273.15); %L36H-4 (horn#2 & #4)
            T48 = double(hdf5read(filename,'/Converted
Telemetry/mwr_hkp_tm_t48')+273.15); %L36H-7 (horn#5 & #7)
            T47 = double(hdf5read(filename,'/Converted
Telemetry/mwr_hkp_tm_t47')+273.15); %L36H-6 (horn#1 & #3)
            % 23H horn plate
            T21 = double(hdf5read(filename,'/Converted
Telemetry/mwr_hkp_tm_t21')+273.15);
            % 36V & H horn plate
            T22 = double(hdf5read(filename,'/Converted
Telemetry/mwr_hkp_tm_t22')+273.15);
            %Noise Diode Sensors
           T13 = double(hdf5read(filename,'/Converted
Telemetry/mwr_hkp_tm_t13')+273.15); %NoiseDiode 23Ghz
           T14 = double(hdf5read(filename,'/Converted
Telemetry/mwr_hkp_tm_t14')+273.15); %NoiseDiode 36Ghz

            %% time comuptation
            mwr_time = double(hdf5read(filename,'/Raw MWR Data/mwr_time'));
            time = datenum(1980,01,06,0,0,mwr_time); % % time in matlab
datenum

            %% Read Counts
            % 23H
            Ca23h = double(hdf5read(filename,'/Raw MWR
Data/mwr_k_h_antenna')); %sig
            Cn23h = double(hdf5read(filename,'/Raw MWR
Data/mwr_k_h_antenna_plus_noise'));   %sig+noise
            Co23h = double(hdf5read(filename,'/Raw MWR Data/mwr_k_h_load'));
%ref
            % 36V          sig                          sig+noise
ref
            Ca36v = double(hdf5read(filename,'/Raw MWR
Data/mwr_ka_v_antenna')); %sig
```

```
            Cn36v = double(hdf5read(filename,'/Raw MWR
Data/mwr_ka_v_antenna_plus_noise'));   %sig+noise
            Co36v = double(hdf5read(filename,'/Raw MWR Data/mwr_ka_v_load'));
%ref
            % 36H          sig                         sig+noise
ref
            Ca36h = double(hdf5read(filename,'/Raw MWR
Data/mwr_ka_h_antenna')); %sig
            Cn36h = double(hdf5read(filename,'/Raw MWR
Data/mwr_ka_h_antenna_plus_noise'));   %sig+noise
            Co36h = double(hdf5read(filename,'/Raw MWR Data/mwr_ka_h_load'));
%ref

            %% Smear Correction

            [Ca23h Cn23h Co23h] = SmearCorrection(Ca23h,Cn23h,Co23h,time);
            [Ca36h Cn36h Co36h] = SmearCorrection(Ca36h,Cn36h,Co36h,time);
            [Ca36v Cn36v Co36v] = SmearCorrection(Ca36v,Cn36v,Co36v,time);

            %% Reading  corresponding L1B file for Geolocation data

            %     filenameb = 'EO_20100522_235454_CUSS_SACD_MWR_L1B_SCI.h5';
            %Rx23H
            k_h_lat = double(hdf5read(filenameb,'/Geolocation
Data/k_h_latitude'));
            k_h_lon = double(hdf5read(filenameb,'/Geolocation
Data/k_h_longitude'));
            k_h_eia = double(hdf5read(filenameb,'/Geolocation
Data/k_h_zenith_angle_to_spacecraft'));
            k_h_az  = double(hdf5read(filenameb,'/Geolocation
Data/k_h_azimuth_angle_to_spacecraft'));
            %Rx36H
            ka_h_lat = double(hdf5read(filenameb,'/Geolocation
Data/ka_h_latitude'));
            ka_h_lon = double(hdf5read(filenameb,'/Geolocation
Data/ka_h_longitude'));
            ka_h_eia = double(hdf5read(filenameb,'/Geolocation
Data/ka_h_zenith_angle_to_spacecraft'));
            ka_h_az  = double(hdf5read(filenameb,'/Geolocation
Data/ka_h_azimuth_angle_to_spacecraft'));
            %Rx36V
            ka_v_lat = double(hdf5read(filenameb,'/Geolocation
Data/ka_v_latitude'));
            ka_v_lon = double(hdf5read(filenameb,'/Geolocation
Data/ka_v_longitude'));
            ka_v_eia = double(hdf5read(filenameb,'/Geolocation
Data/ka_v_zenith_angle_to_spacecraft'));
            ka_v_az  = double(hdf5read(filenameb,'/Geolocation
Data/ka_v_azimuth_angle_to_spacecraft'));
            % RX37H spares
            Spare1_36h=NaN(length(Ca36h),1);
            Spare2_36h=NaN(length(Ca36h),1);
            Spare3_36h=NaN(length(Ca36h),1);
            Spare4_36h=NaN(length(Ca36h),1);
            Spare5_36h=NaN(length(Ca36h),1);
            % RX23H spares
```

```
            Spare1_23h=NaN(length(Ca23h),1);
            Spare2_23h=NaN(length(Ca23h),1);
            Spare3_23h=NaN(length(Ca23h),1);
            Spare4_23h=NaN(length(Ca23h),1);
            Spare5_23h=NaN(length(Ca23h),1);
            % RX37V spares
            Spare1_36v=NaN(length(Ca36v),1);
            Spare2_36v=NaN(length(Ca36v),1);
            Spare3_36v=NaN(length(Ca36v),1);
            Spare4_36v=NaN(length(Ca36v),1);
            Spare5_36v=NaN(length(Ca36v),1);

            %%  Linearization : the output are linearized counts and noide
diode deflection injected noise Tn

[Ca23h,Cn23h,Co23h,Tn23h]=linearization(Ca23h,Cn23h,Co23h,To23h,390,-2.1708e-
004);

[Ca36h,Cn36h,Co36h,Tn36h]=linearization(Ca36h,Cn36h,Co36h,To36h,270,-6.9064e-
004);

[Ca36v,Cn36v,Co36v,Tn36v]=linearization(Ca36v,Cn36v,Co36v,To36v,274,-7.4677e-
004);
            %% Remove NEDT using running moving average
            gain23h = gain_filter_v2((Cn23h-Ca23h)./(Tn23h),191);
            gain36h = gain_filter_v2((Cn36h-Ca36h)./(Tn36h),159);
            gain36v = gain_filter_v2((Cn36v-Ca36v)./(Tn36v),191);
            %% Tin linear
            Tin23h = (Ca23h-Co23h)./gain23h + To23h;
            Tin36v = (Ca36v-Co36v)./gain36v + To36v;
            Tin36h = (Ca36h-Co36h)./gain36h + To36h;

            %% Tap Computation per horn basis
            horn_id23 = double(hdf5read(filename,'/Raw MWR
Data/mwr_k_band_horn_id')); %horn numbers 23 GHz
            horn_id36 = double(hdf5read(filename,'/Raw MWR
Data/mwr_ka_band_horn_id')); %horn numbers 37 GHz

            for i = 1:8

                ind23 = find(horn_id23 == i);
                ind36 = find(horn_id36 == i);


                temp.Lat = k_h_lat(i,:)';
                temp.Lon = k_h_lon(i,:)';
                temp.EIA = k_h_eia(i,:)';
                temp.az  = k_h_az(i,:)';


                temp.Lat(temp.Lat == 0) = [];
                temp.Lon(temp.Lon == 0) = [];
                temp.EIA(temp.EIA == 0) = [];
                temp.az(temp.az == 0)   = [];
```

```
                lim = min(length(temp.Lat),length(ind23)); % choose the min
length

                temp.Lat = temp.Lat(1:lim);
                temp.Lon = temp.Lon(1:lim);
                temp.EIA = temp.EIA(1:lim);
                temp.az  = temp.az(1:lim);
                ind23 = ind23(1:lim);


                temp.Tin  = Tin23h(ind23);
                temp.time = time(ind23);
                temp1.To  = To23h(ind23);

                % counts
                temp.Ca = Ca23h(ind23);
                temp.Cn = Cn23h(ind23);
                temp.Co = Co23h(ind23);
                temp.Tn = Tn23h(ind23);
                temp.gain = gain23h(ind23);
                %Noise Diode Temperature from sensor
                temp.Nd = T13(ind23); %Noise Diode for 23Gh
                %spares

                temp.spare1=Spare1_23h(ind23);
                temp.spare2=Spare2_23h(ind23);
                temp.spare3=Spare3_23h(ind23);
                temp.spare4=Spare4_23h(ind23);
                temp.spare5=Spare5_23h(ind23);

                eval(['b = coeff.RX23H.B' num2str(i) ';']);
                eval(['err = bias.RX23H.B',num2str(i) ';']);% load bias
slope&offset

                switch(i)
                    case 1
                        temp1.T1 = T4(ind23);temp1.T2 = T6(ind23);temp1.T3 =
T33(ind23);temp1.T4 = T21(ind23);
                    case 2
                        temp1.T1 = T4(ind23);temp1.T2 = T5(ind23);temp1.T3 =
T7(ind23);temp1.T4 = T21(ind23);
                    case 3
                        temp1.T1 = T4(ind23);temp1.T2 = T6(ind23);temp1.T3 =
T33(ind23);temp1.T4 = T21(ind23);
                    case 4
                        temp1.T1 = T4(ind23);temp1.T2 = T5(ind23);temp1.T3 =
T7(ind23);temp1.T4 = T21(ind23);
                    case 5
                        temp1.T1 = T4(ind23);temp1.T2 = T6(ind23);temp1.T3 =
T34(ind23);temp1.T4 = T21(ind23);
                    case 6
                        temp1.T1 = T4(ind23);temp1.T2 = T5(ind23);temp1.T3 =
T8(ind23);temp1.T4 = T21(ind23);
                    case 7
```

```
                        temp1.T1 = T4(ind23);temp1.T2 = T6(ind23);temp1.T3 =
T34(ind23);temp1.T4 = T21(ind23);
                    case 8
                        temp1.T1 = T4(ind23);temp1.T2 = T5(ind23);temp1.T3 =
T8(ind23);temp1.T4 = T21(ind23);
                end

                temp.Tb=(temp.Tin-
((b(2).*temp1.To+b(3).*temp1.T1+b(4).*temp1.T2+b(5).*temp1.T3+b(6).*temp1.T4)
)./b(1);
                temp.Tb = (temp.Tb - err.offset)./ err.slope;% correct bias
                temp.calib_coeff = err;
                temp.calib_coeff.b = b;temp.Telem_Temp = temp1;
                eval(['data.RX23H.B' num2str(i) ' = temp;']);
                clear temp temp1 temp2;
                %% 36 V
                %      temp.Ta = Ta36(ind36);

                temp.Lat = ka_v_lat(i,:)';
                temp.Lon = ka_v_lon(i,:)';
                temp.EIA = ka_v_eia(i,:)';
                temp.az  = ka_v_az(i,:)';

                temp.Lat(temp.Lat == 0) = [];
                temp.Lon(temp.Lon == 0) = [];
                temp.EIA(temp.EIA == 0) = [];
                temp.az(temp.az == 0)   = [];

                lim = min(length(temp.Lat),length(ind36)); % choose the min
length

                temp.Lat = temp.Lat(1:lim);
                temp.Lon = temp.Lon(1:lim);
                temp.EIA = temp.EIA(1:lim);
                temp.az  = temp.az(1:lim);
                ind36 = ind36(1:lim);

                temp.Tin = Tin36v(ind36);
                temp.time = time(ind36);
                temp1.To = To36v(ind36);

                % counts
                temp.Ca = Ca36v(ind36);
                temp.Cn = Cn36v(ind36);
                temp.Co = Co36v(ind36);
                temp.Tn = Tn36v(ind36);
                temp.gain = gain36v(ind36);
                 %Noise Diode Temperature from sensor
                temp.Nd = T14(ind36); %Noise Diode for 36Gh
                 %spares
                temp.spare1=Spare1_36v(ind23);
                temp.spare2=Spare2_36v(ind23);
                temp.spare3=Spare3_36v(ind23);
                temp.spare4=Spare4_36v(ind23);
                temp.spare5=Spare5_36v(ind23);
```

```
                eval(['b = coeff.RX37V.B' num2str(i) ';']);
                eval(['err = bias.RX37V.B',num2str(i) ';']);% load bias
slope&offset

                switch(i)
                    case 1
                        temp1.T1 = T35(ind36);temp1.T2 = T37(ind36);temp1.T3
= T41(ind36);temp1.T4 = T22(ind36);
                    case 2
                        temp1.T1 = T35(ind36);temp1.T2 = T36(ind36);temp1.T3
= T39(ind36);temp1.T4 = T22(ind36);
                    case 3
                        temp1.T1 = T35(ind36);temp1.T2 = T37(ind36);temp1.T3
= T41(ind36);temp1.T4 = T22(ind36);
                    case 4
                        temp1.T1 = T35(ind36);temp1.T2 = T36(ind36);temp1.T3
= T39(ind36);temp1.T4 = T22(ind36);
                    case 5
                        temp1.T1 = T35(ind36);temp1.T2 = T37(ind36);temp1.T3
= T40(ind36);temp1.T4 = T22(ind36);
                    case 6
                        temp1.T1 = T35(ind36);temp1.T2 = T36(ind36);temp1.T3
= T38(ind36);temp1.T4 = T22(ind36);
                    case 7
                        temp1.T1 = T35(ind36);temp1.T2 = T37(ind36);temp1.T3
= T40(ind36);temp1.T4 = T22(ind36);
                    case 8
                        temp1.T1 = T35(ind36);temp1.T2 = T36(ind36);temp1.T3
= T38(ind36);temp1.T4 = T22(ind36);
                end

                temp.Tb=(temp.Tin-
((b(2).*temp1.To+b(3).*temp1.T1+b(4).*temp1.T2+b(5).*temp1.T3+b(6).*temp1.T4)
)./b(1);
                temp.Tb = (temp.Tb - err.offset)./ err.slope;% correct bias
                temp.calib_coeff = err;
                temp.calib_coeff.b = b;temp.Telem_Temp = temp1;
                eval(['data.RX37V.B' num2str(i) ' = temp;']);
                clear temp temp1 temp2;
                %% 36 H
                %       temp.Ta = Ta36(ind36);

                temp.Lat = ka_h_lat(i,:)';
                temp.Lon = ka_h_lon(i,:)';
                temp.EIA = ka_h_eia(i,:)';
                temp.az  = ka_h_az(i,:)';

                temp.Lat(temp.Lat == 0) = [];
                temp.Lon(temp.Lon == 0) = [];
                temp.EIA(temp.EIA == 0) = [];
                temp.az(temp.az == 0)   = [];

                lim = min(length(temp.Lat),length(ind36)); % choose the min
length
```

```
                temp.Lat = temp.Lat(1:lim);
                temp.Lon = temp.Lon(1:lim);
                temp.EIA = temp.EIA(1:lim);
                temp.az  = temp.az(1:lim);
                ind36 = ind36(1:lim);

                temp.Tin = Tin36h(ind36);
                temp.time = time(ind36);
                temp1.To = To36h(ind36);

                % counts
                temp.Ca = Ca36h(ind36);
                temp.Cn = Cn36h(ind36);
                temp.Co = Co36h(ind36);
                temp.Tn = Tn36h(ind36);
                temp.gain = gain36h(ind36);
                 %Noise Diode Temperature from sensor
                temp.Nd = T14(ind36); %Noise Diode for 36Gh
                %spares
                temp.spare1=Spare1_36h(ind23);
                temp.spare2=Spare2_36h(ind23);
                temp.spare3=Spare3_36h(ind23);
                temp.spare4=Spare4_36h(ind23);
                temp.spare5=Spare5_36h(ind23);

                eval(['b = coeff.RX37H.B' num2str(i) ';']);
                eval(['err = bias.RX37H.B',num2str(i) ';']);% load bias
slope&offset

                switch(i)
                    case 1
                        temp1.T1 = T42(ind36);temp1.T2 = T44(ind36);temp1.T3
= T47(ind36);temp1.T4 = T22(ind36);
                    case 2
                        temp1.T1 = T42(ind36);temp1.T2 = T43(ind36);temp1.T3
= T45(ind36);temp1.T4 = T22(ind36);
                    case 3
                        temp1.T1 = T42(ind36);temp1.T2 = T44(ind36);temp1.T3
= T47(ind36);temp1.T4 = T22(ind36);
                    case 4
                        temp1.T1 = T42(ind36);temp1.T2 = T43(ind36);temp1.T3
= T45(ind36);temp1.T4 = T22(ind36);
                    case 5
                        temp1.T1 = T42(ind36);temp1.T2 = T44(ind36);temp1.T3
= T48(ind36);temp1.T4 = T22(ind36);
                    case 6
                        temp1.T1 = T42(ind36);temp1.T2 = T43(ind36);temp1.T3
= T46(ind36);temp1.T4 = T22(ind36);
                    case 7
                        temp1.T1 = T42(ind36);temp1.T2 = T44(ind36);temp1.T3
= T48(ind36);temp1.T4 = T22(ind36);
                    case 8
                        temp1.T1 = T42(ind36);temp1.T2 = T43(ind36);temp1.T3
= T46(ind36);temp1.T4 = T22(ind36);
                end
```

```
                temp.Tb=(temp.Tin-
((b(2).*temp1.To+b(3).*temp1.T1+b(4).*temp1.T2+b(5).*temp1.T3+b(6).*temp1.T4)
)./b(1);
                temp.Tb = (temp.Tb - err.offset)./ err.slope;% correct bias
                temp.calib_coeff = err;
                temp.calib_coeff.b = b;temp.Telem_Temp = temp1;
                eval(['data.RX37H.B' num2str(i) ' = temp;']);
                clear temp temp1 temp2;

            end
            % save as matlab file
            save(opname,'data');
toc
            disp([l1name ' -> ' opname]);
        else
            disp(['Missing L1B for ' l1name]);
        end% end isempty s2 check

    end
end
```

APPENDIX D
MWR ANTENNA SWITCH MATRIX COEFFICIENTS

In this dissertation, the ASM loss coefficients were empirically derived. Using Eq 4.15 and substituting T_{ap} by the measured blackbody target apparent temperature, the coefficients b1 through b6 was derived based upon a regression model using the mesured temperatures (T_o, T_1, T_2, T_3, *and* T_4) and calculated (T_{in}) for each channel and each beam. The derived ASM loss coefficients for the three channels are tabulated below:

23GHz H-pol MWR ASM

Horn #	b1	b2	b3	b4	b5	b6
1	0.67438	-0.54306	1.43576	-2.02254	1.41613	0.03251
2	0.71399	-0.38018	1.19894	-2.02556	1.64646	-0.15425
3	0.73130	-0.56172	1.50844	-2.15451	1.46753	0.00058
4	0.79209	-0.49299	1.41873	-2.55336	2.03659	-0.20091
5	0.74579	-0.52948	2.11321	-3.13804	1.79694	0.00240
6	0.74342	-0.23588	0.01956	1.86900	-1.76044	0.35936
7	0.68216	-0.13980	0.53659	1.08866	-1.43355	0.26851
8	0.75166	-0.23778	0.06166	1.79479	-1.73166	0.35579

37GHz H-pol MWR ASM

Horn #	b1	b2	b3	b4	b5	b6
1	0.62706	0.21571	-0.86628	-2.41461	3.70535	-0.27382
2	0.64582	0.10593	0.12055	-0.97760	0.81005	0.28922
3	0.63798	0.23636	-0.93770	-2.35933	3.71133	-0.29555
4	0.64071	0.09310	-0.01945	-1.48758	1.52046	0.24706
5	0.65371	-0.31739	2.38665	-9.27854	7.63594	-0.09648
6	0.63537	0.05147	0.89528	-1.45818	0.82690	0.03902
7	0.63853	-0.44092	3.04940	-11.42137	9.30519	-0.14853
8	0.63082	0.04658	0.94023	-1.53745	0.90415	0.00525

37GHz V-pol MWR ASM

Horn #	b1	b2	b3	b4	b5	b6
1	0.58246	-0.03871	0.57149	-0.32343	0.16234	0.03684
2	0.55287	-0.05505	0.70932	0.57849	-0.86921	0.08124
3	0.59368	-0.03642	0.58306	-0.46387	0.28204	0.03149
4	0.55038	-0.04395	0.67959	0.69870	-0.96413	0.07877
5	0.59611	-0.05133	1.05905	-1.46945	0.83670	0.02034
6	0.58967	-0.04422	0.55560	-0.29994	0.15933	0.03340
7	0.58371	-0.07742	1.52172	-2.55950	1.51364	0.00983
8	0.58266	-0.04494	0.56892	-0.43875	0.29771	0.02669

APPENDIX E
DOUBLE DIFFERENCE BETWEEN MWR AND WINDSAT

The MWR (V6.0) and WS data from 2012 and 2013 was used, to validate the MWR Tb. After the gridding and collocating processes of the data for both sensors, CFRSL RTM was used to adjust WS Tb's using Eq. 5.1. After applying the APC and other radiometric biases correction on the MWR Tb's, a five day average double difference technique was performed to verify the results of the MWR counts-to-Tb algorithm (V6.0). The time series of the 5-day average double difference and the image of the five day 5º latitude for the are presented in the figures below:

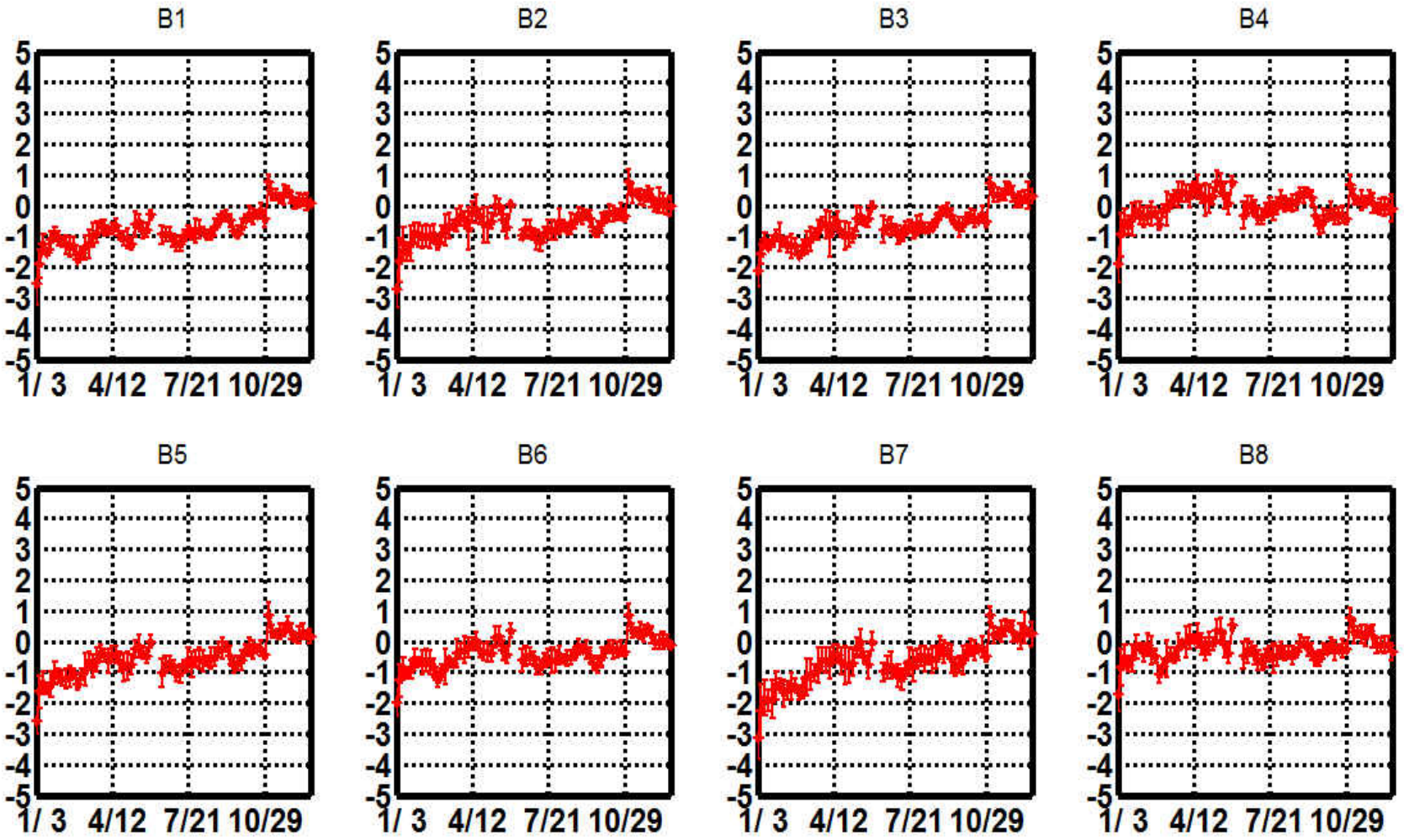

Figure E.1 37GHz H-pol 5 day average double difference between MWR and WindSat of 2012

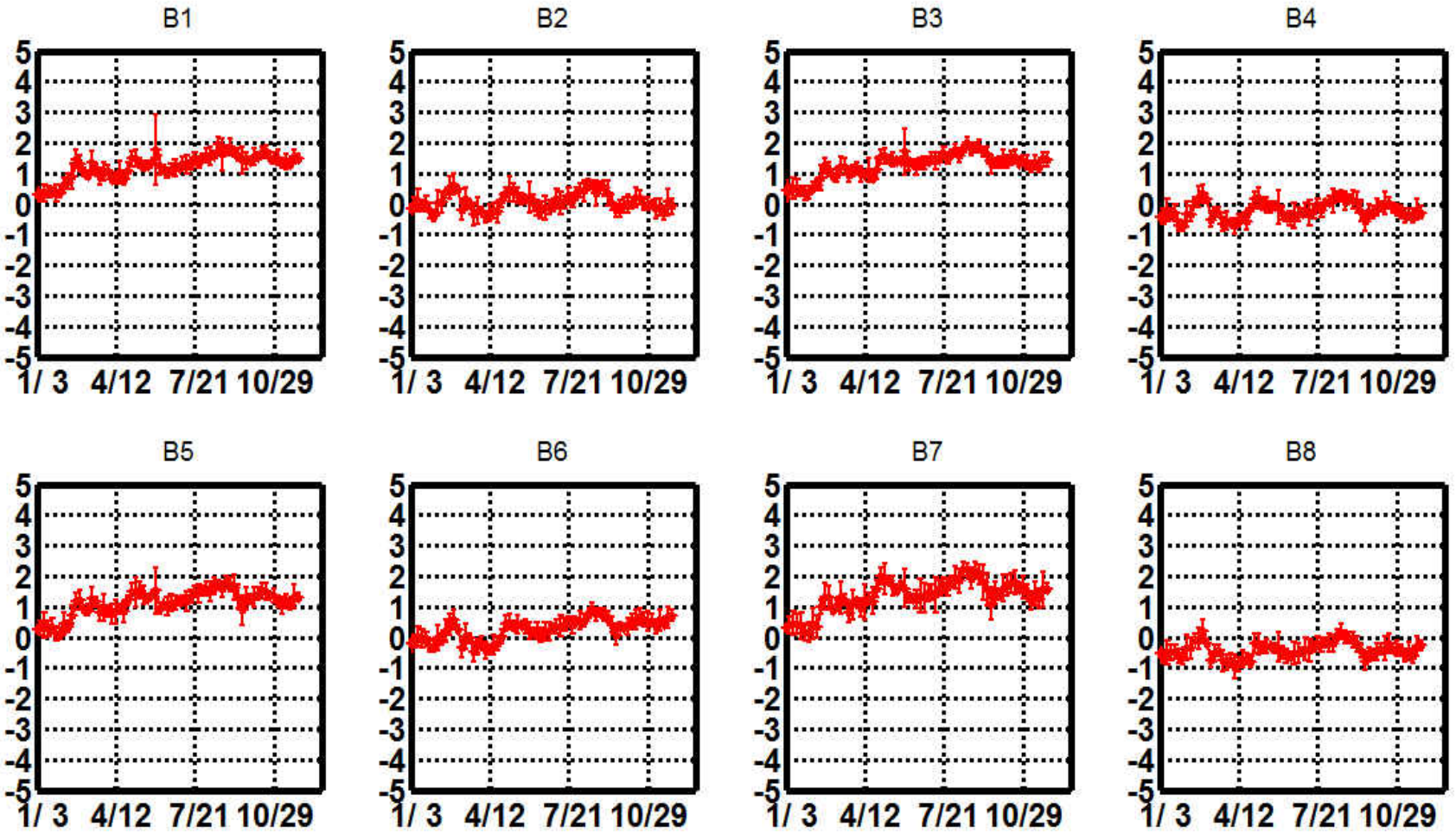

Figure E.2 37GHz H-pol 5 day average double difference between MWR and WindSat of 2013

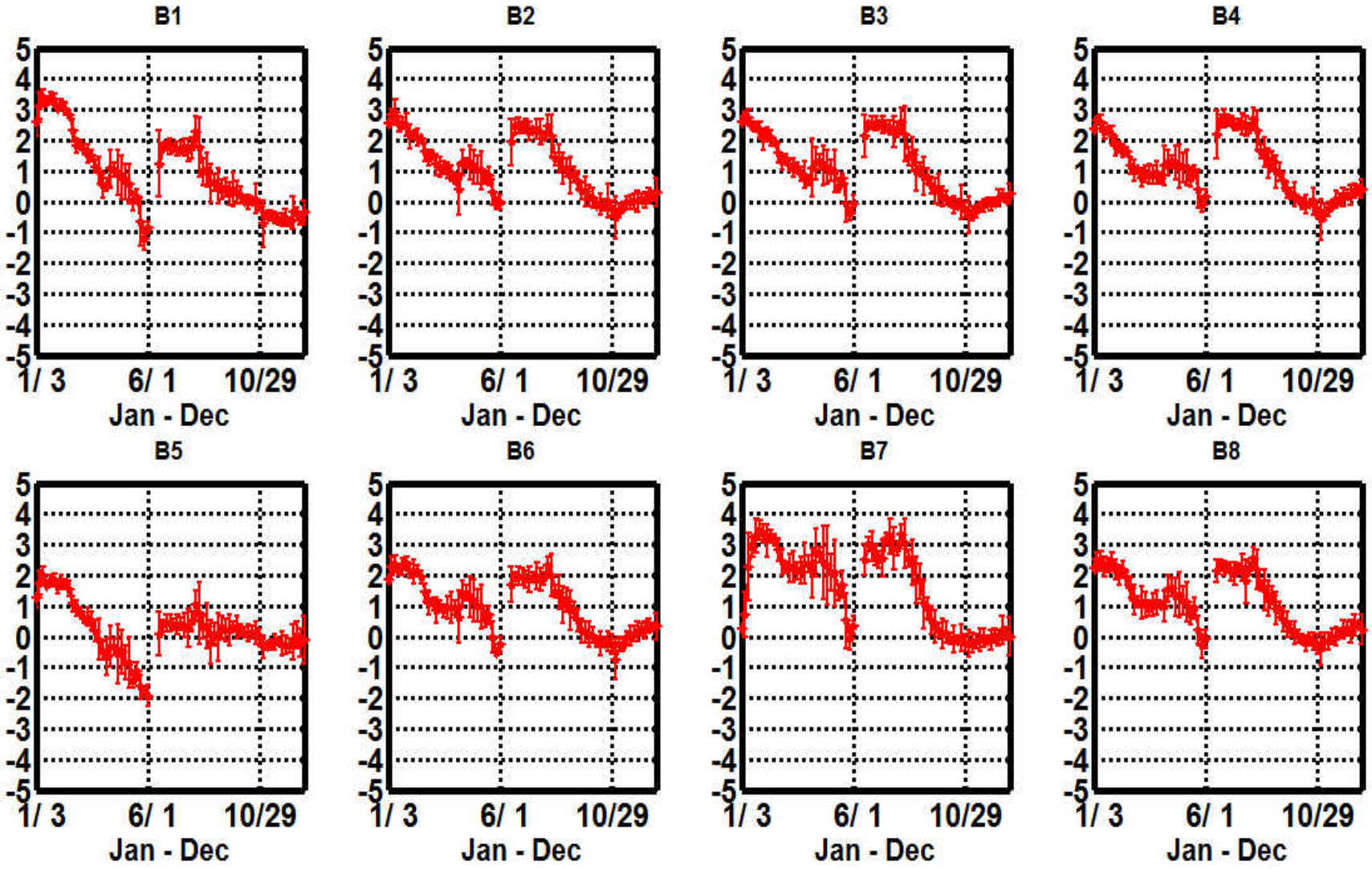

Figure E.3 23GHz H-pol 5 day average double difference between MWR and WindSat of 2012

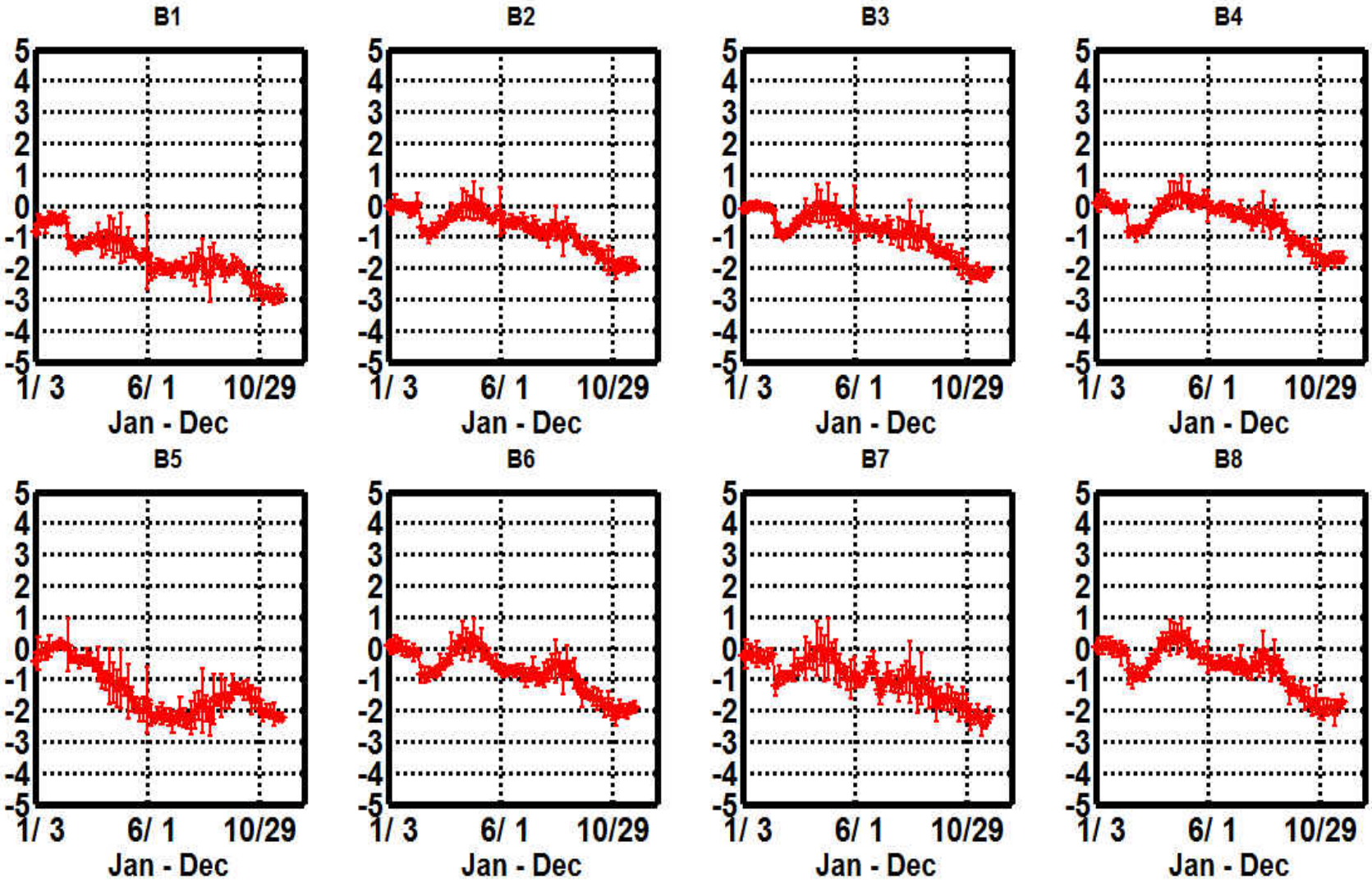

Figure E.4 23GHz H-pol 5 day average double difference between MWR and WindSat of 2013

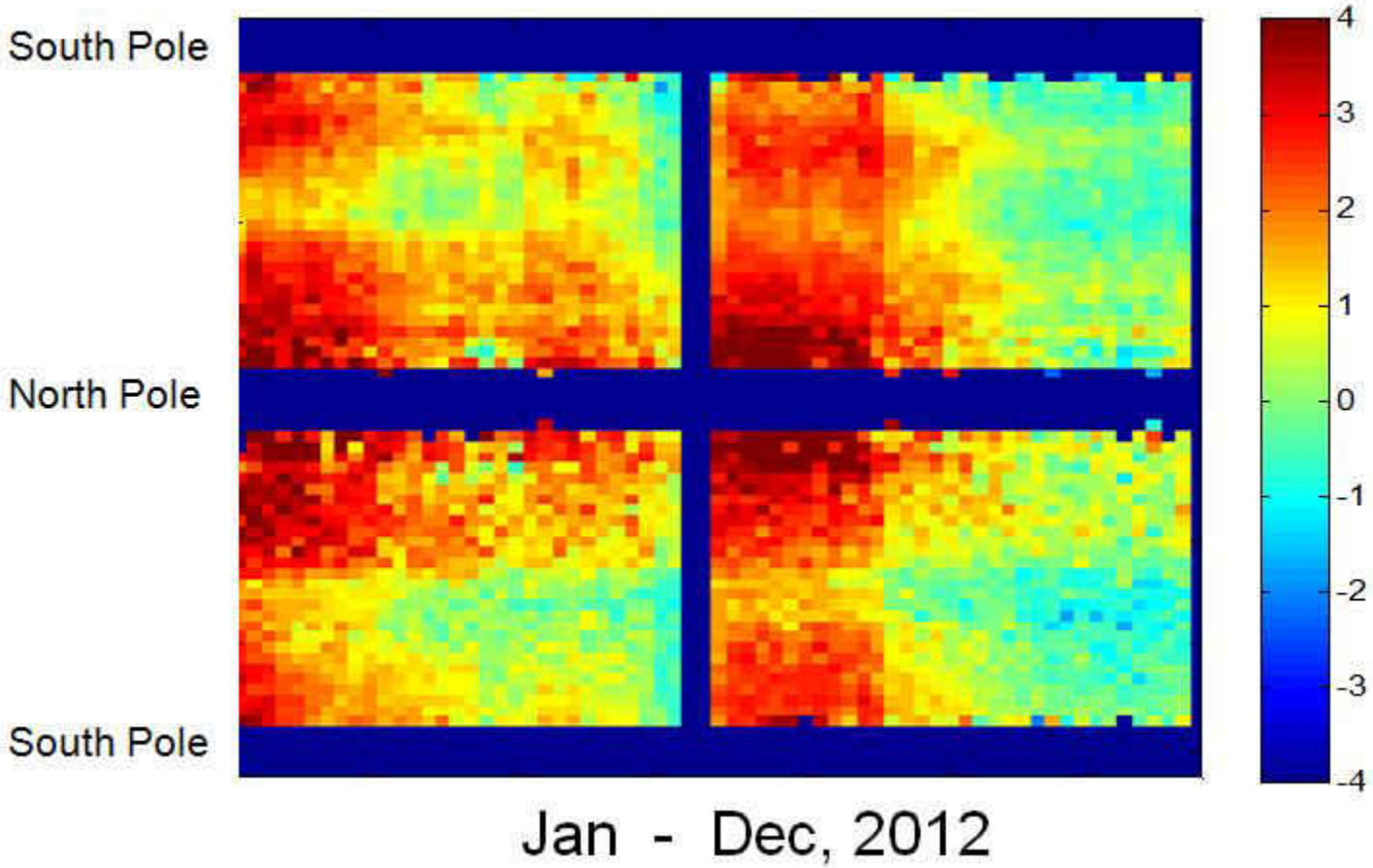

Figure E.5 23GHz H-pol 5 Five days Average in 5° Lat Zones even Beams

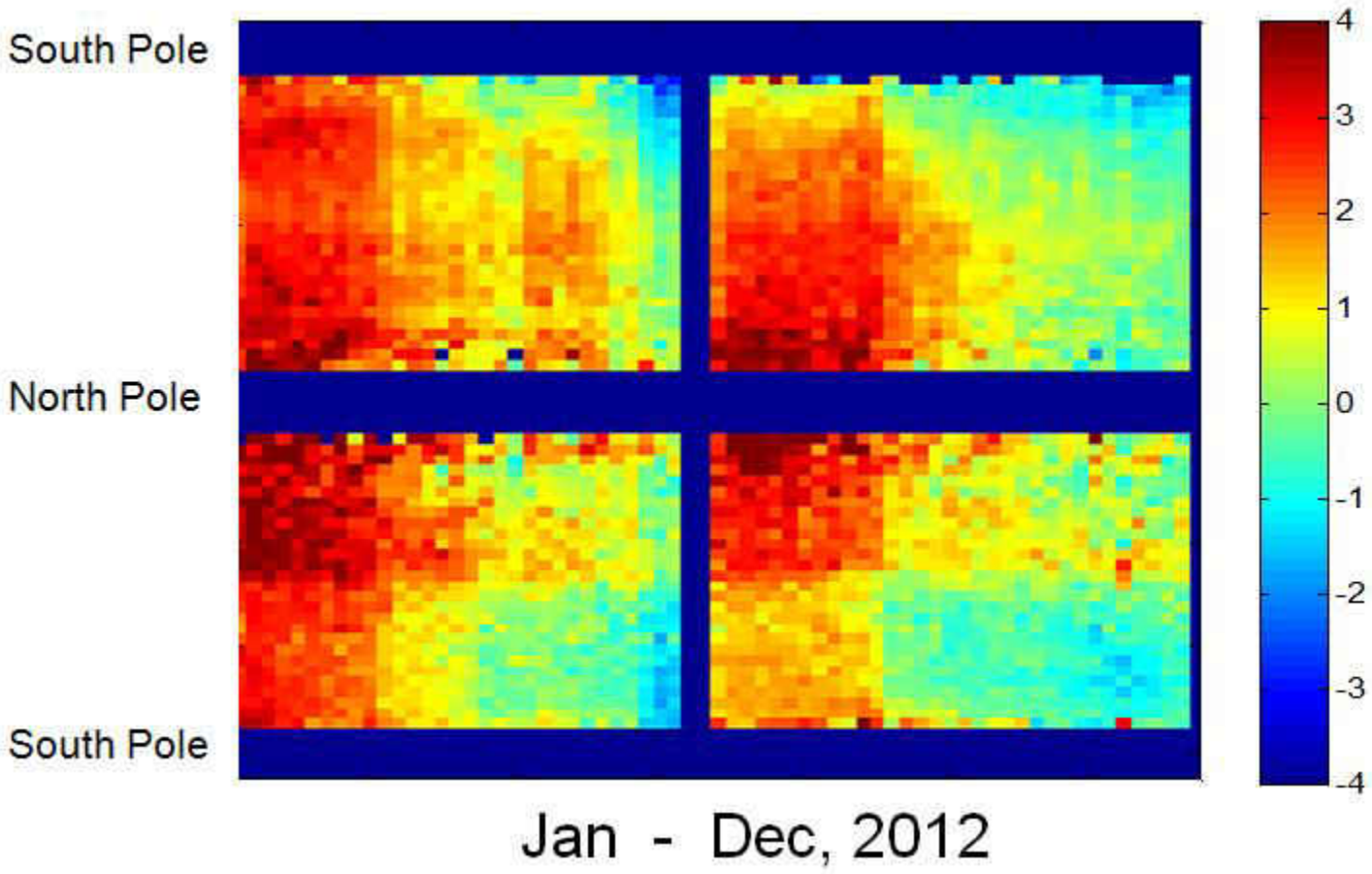

Figure E.6 23GHz H-pol 5 Five days Average in 5° Lat Zones odd Beams

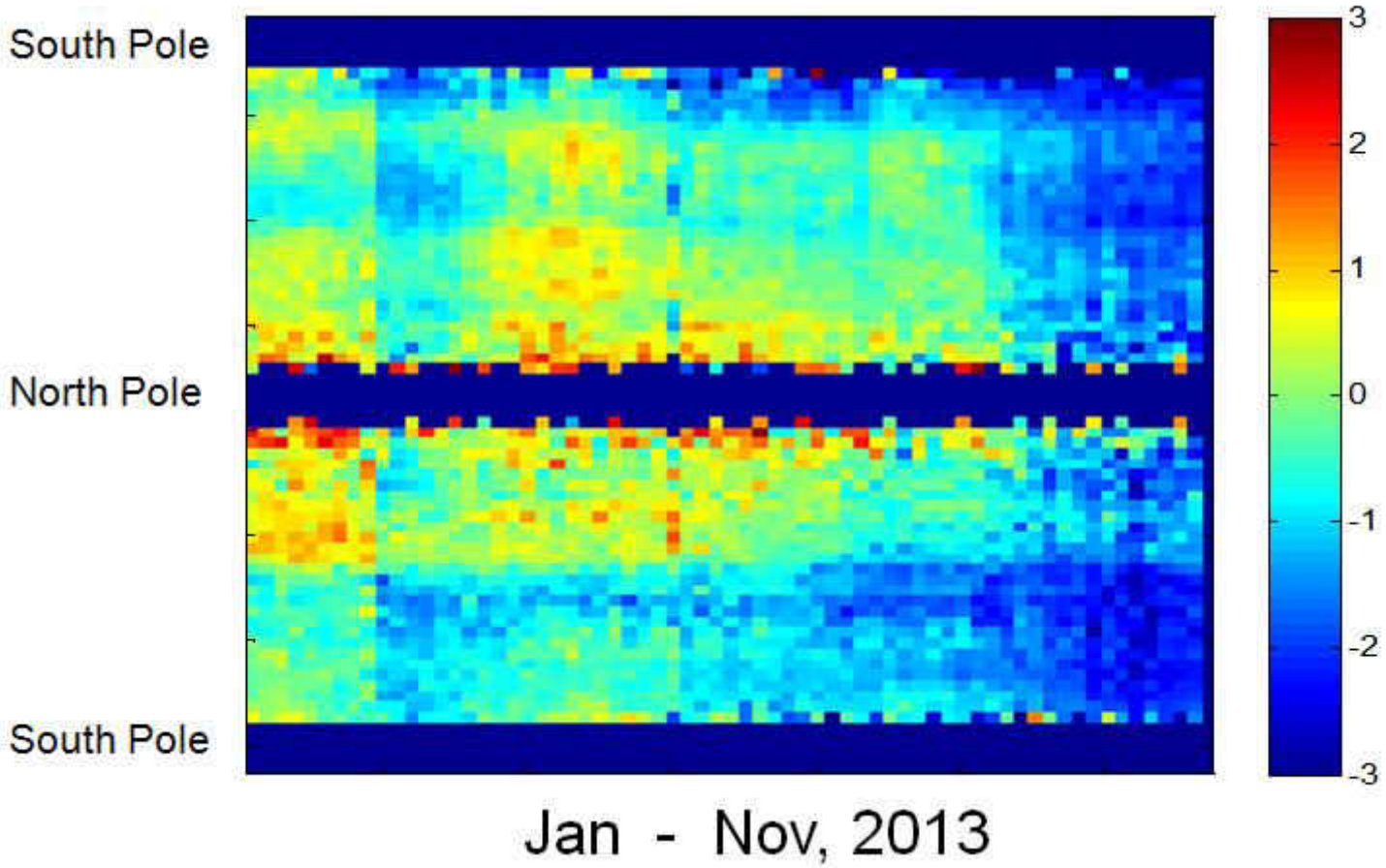

Figure E.7 23GHz H-pol 5 Five days Average in 5° Lat Zones even Beams

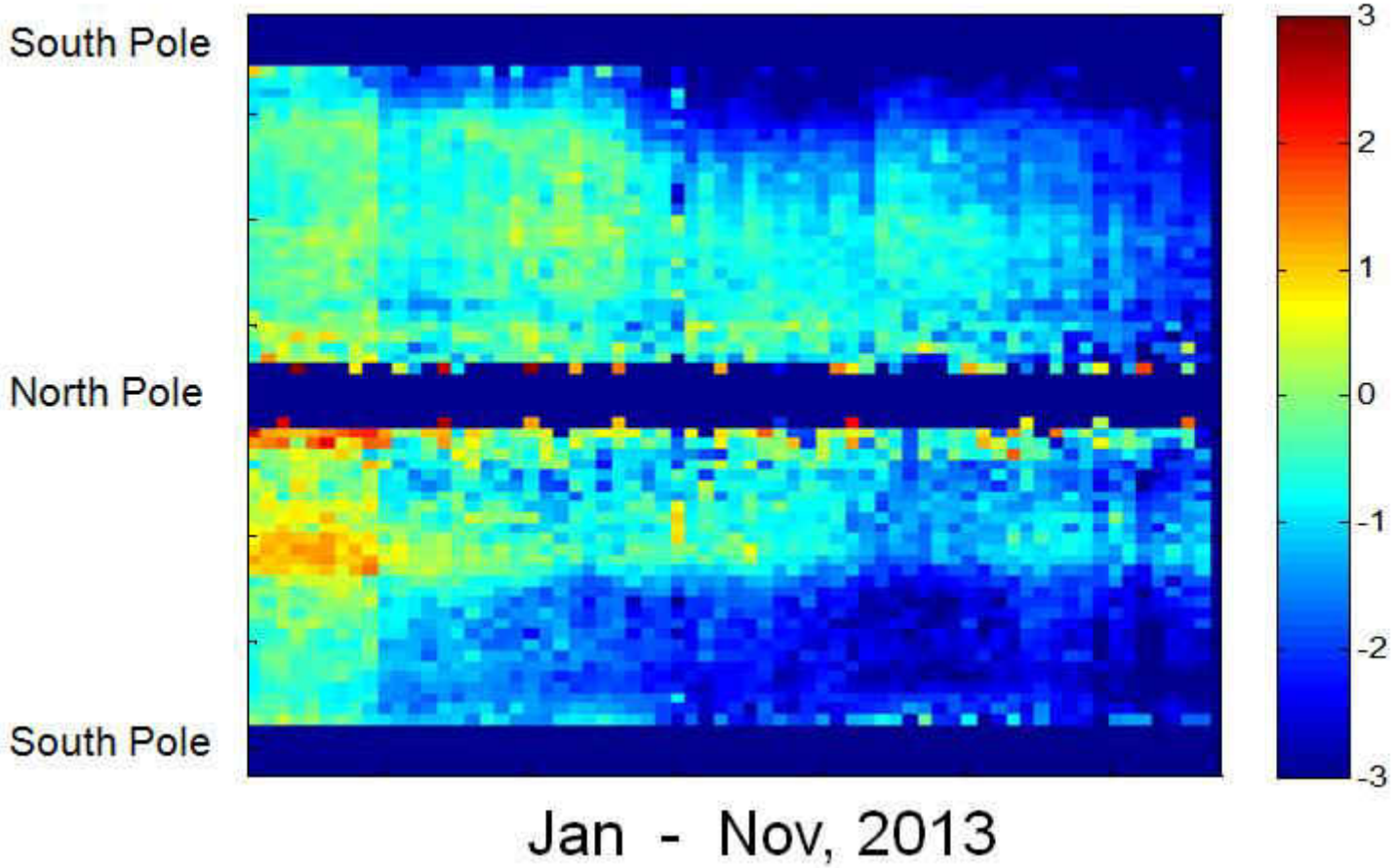

Figure E.8 23GHz H-pol 5 Five days Average in 5° Lat Zones odd Beams

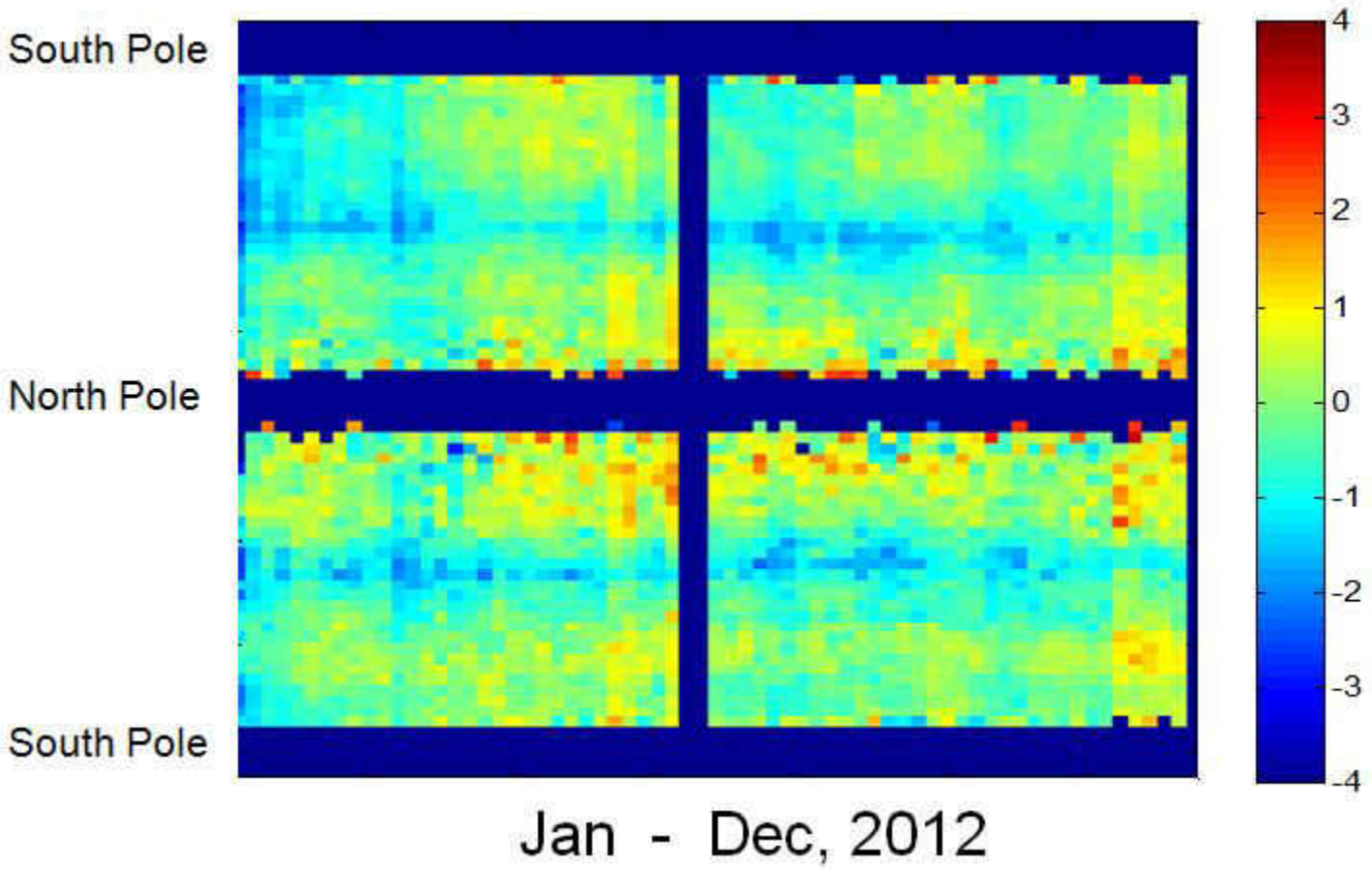

Figure E.9 37GHz H-pol 5 Five days Average in 5° Lat Zones even Beams

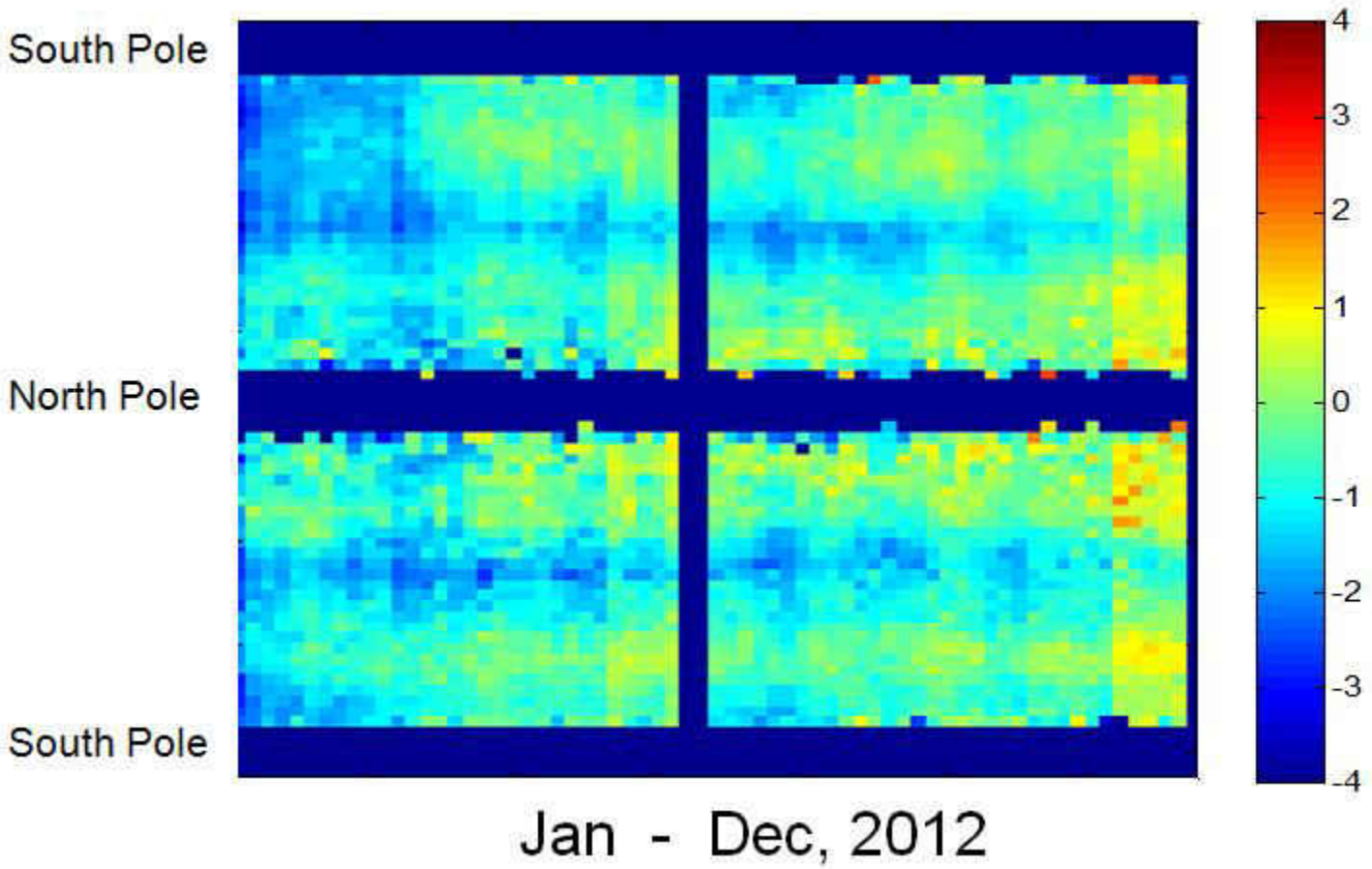

Figure E.10 37GHz H-pol 5 Five days Average in 5° Lat Zones odd Beams

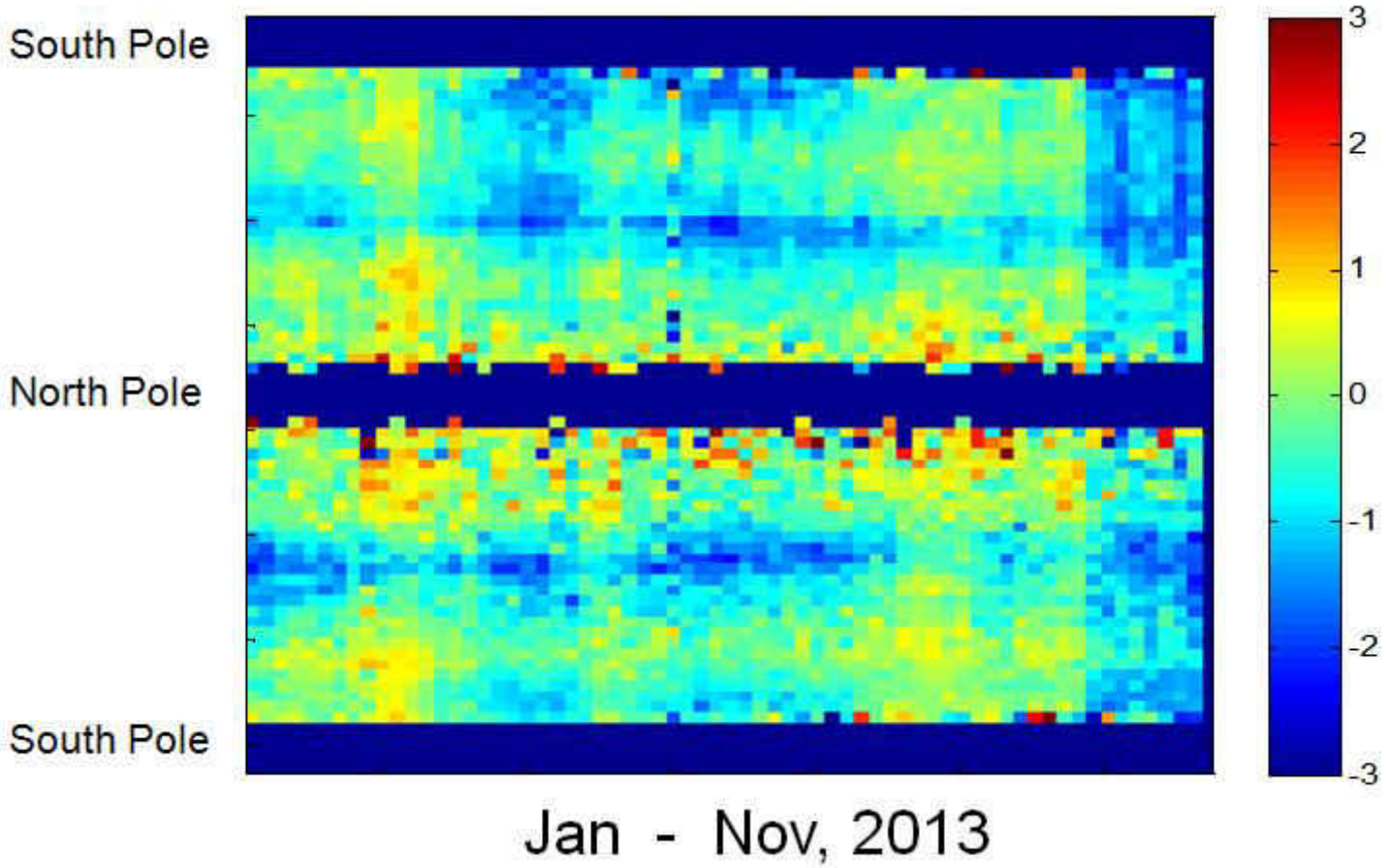

Figure E.11 37GHz H-pol 5 Five days Average in 5° Lat Zones even Beams

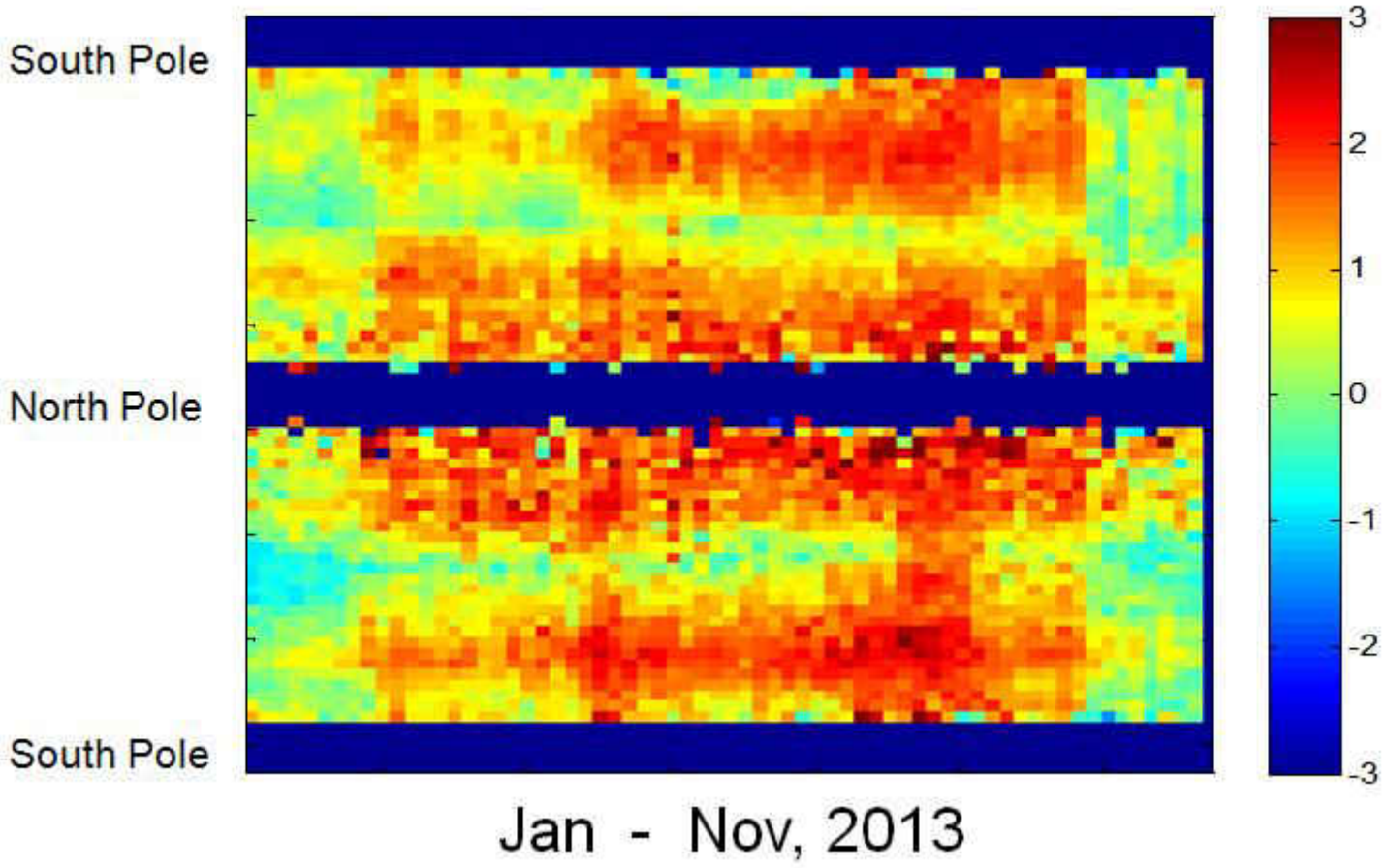

Figure E.12 37GHz H-pol 5 Five days Average in 5° Lat Zones odd Beams

APPENDIX F
COLD SKY CALIBRATION MEASUREMENTS

For the MWR frequencies, space is homogenous isotropic distributed target of a brightness temperature 2.73K. This greatly evaluates the radiometric calibration procedure by looking at the deep space measurements. A comparison of V5.0S and V6.0 of the deep space calibration measurements is shown in the figures below for 37GHz H-pol and 23GHz H-pol. The results of the MWR calibration V5.0S shows that the MWR Tb's have a very high biases during the deep space calibration measurements, whereas V6.0 demonstrates the perfection of the new MWR calibration, where the MWR Tb's are ~2.73K when the main reflector looks at the deep space.

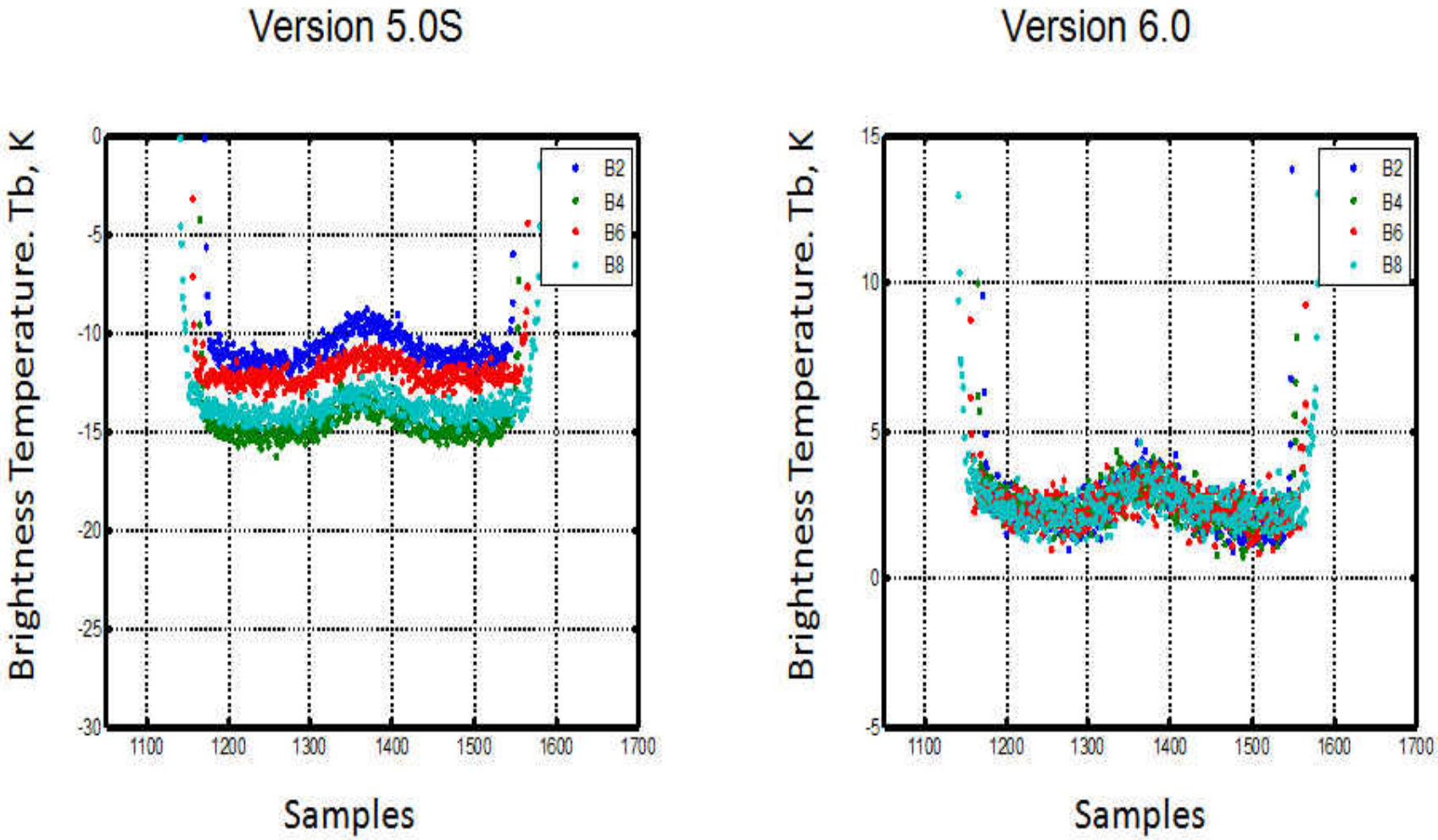

Figure F.1 37GHz H-pol cold sky calibration measurements, even beams

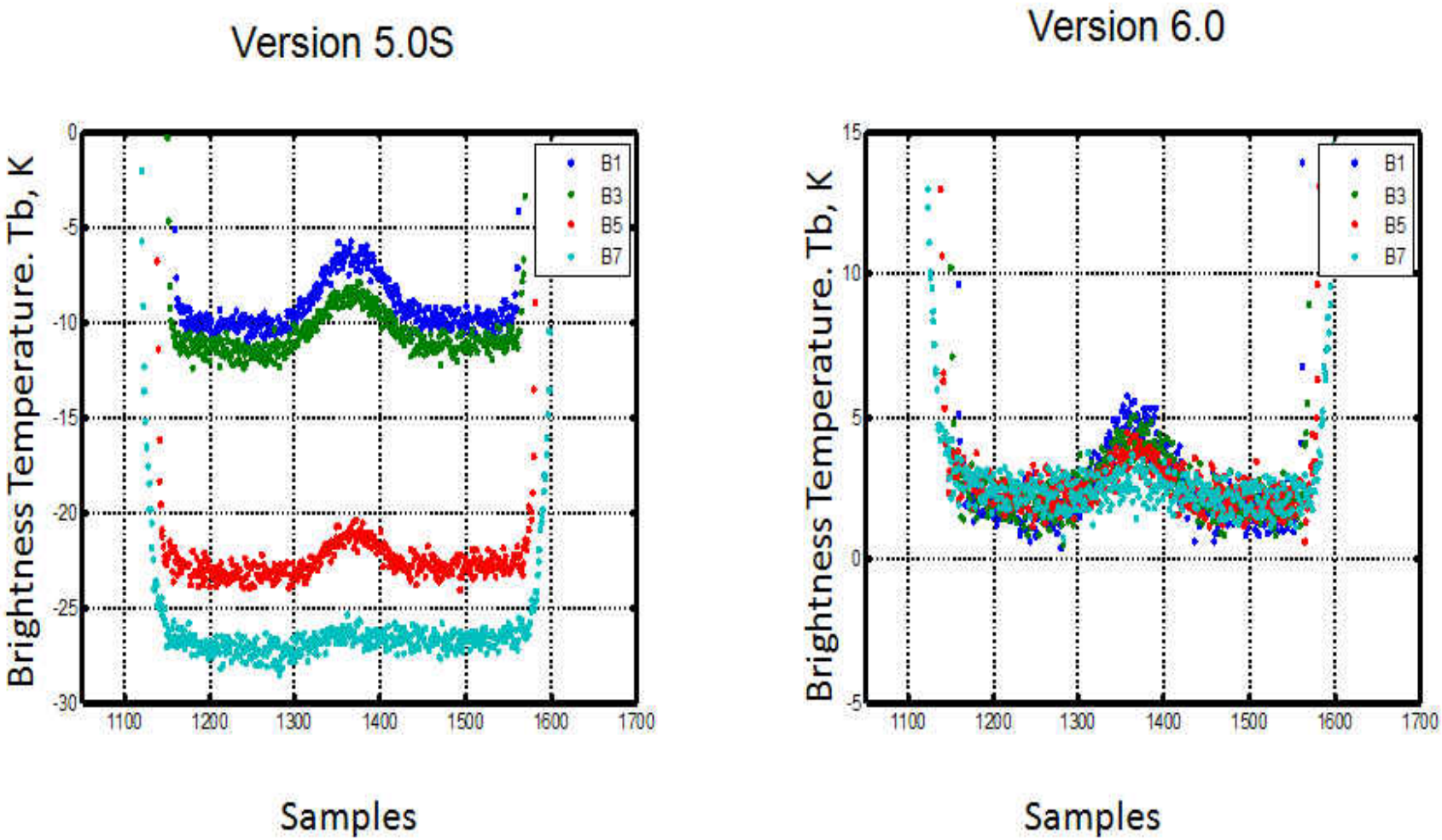

Figure F.2 37GHz H-pol cold sky calibration measurements, odd beams

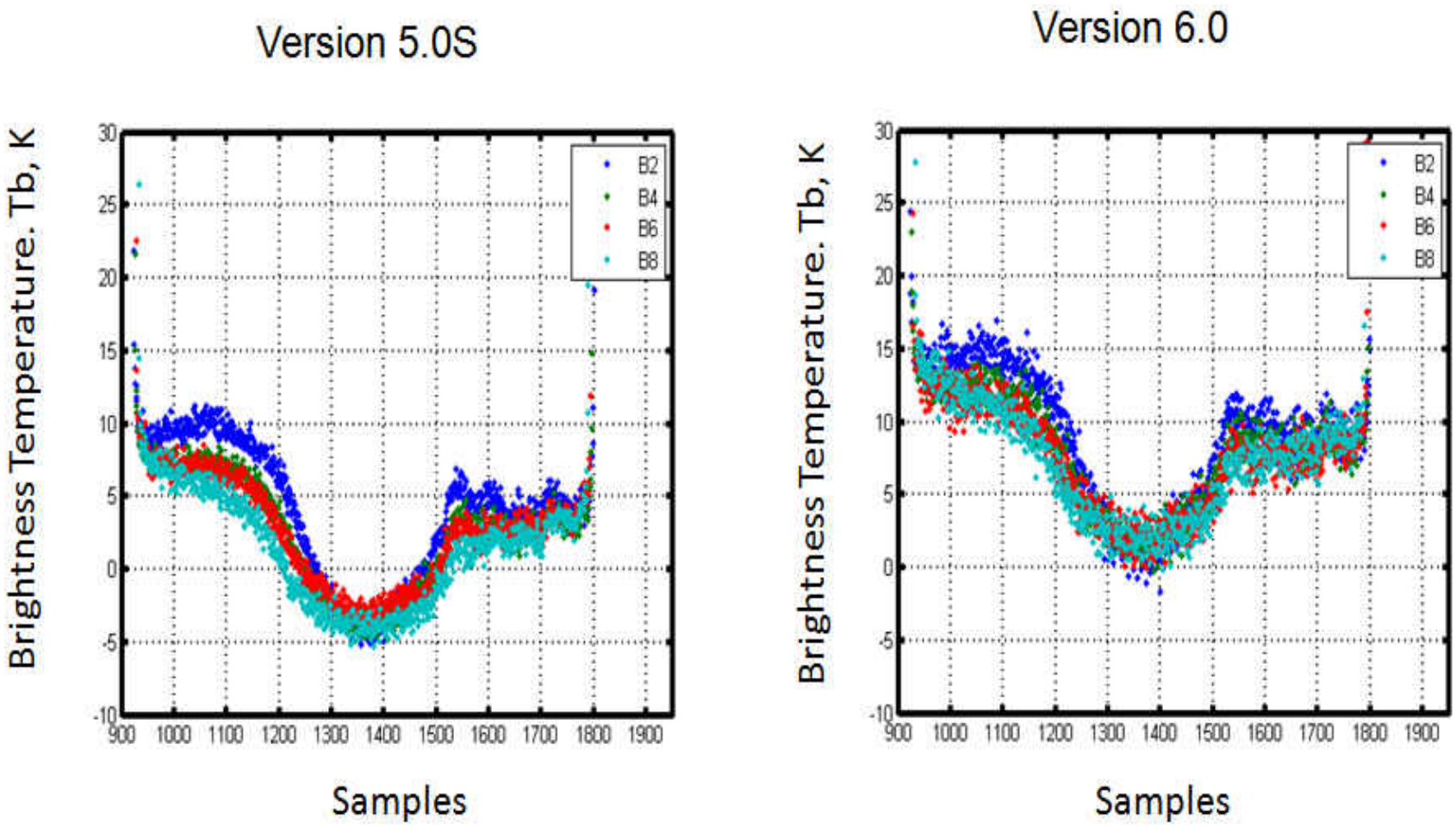

Figure F.3 23GHz H-pol cold sky calibration measurements, even beams

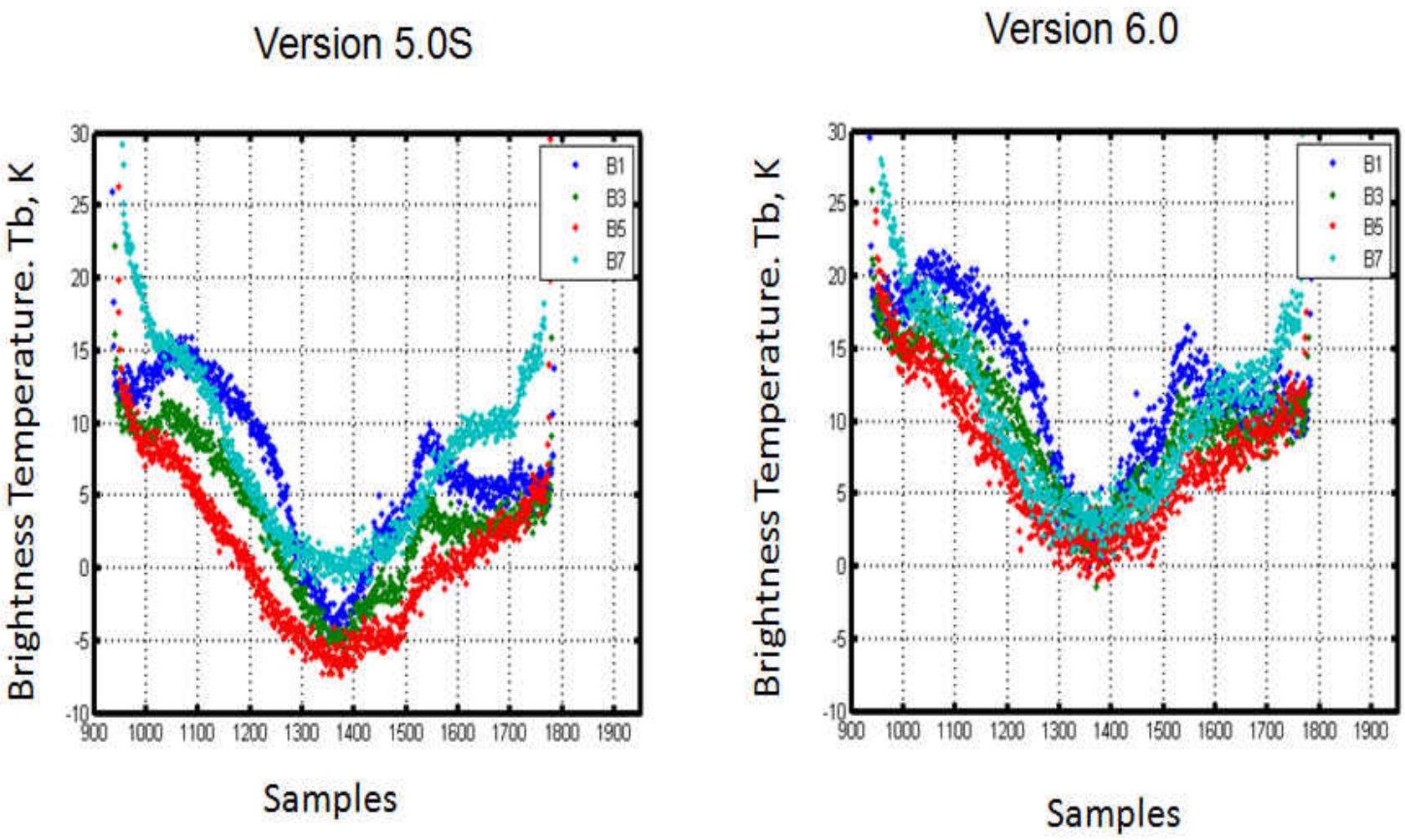

Figure F.4 23GHz H-pol cold sky calibration measurements, odd beams

APPENDIX G
MWR TB OVER LAND ANALYSIS

During my research, a comparison between MWR and WS Tb's over land was performed. No adjustments of the Tb observations over land were made, because the Tb dependence on the earth incidence angle is negligible. Despite the fact that MWR and WindSat share some similarities, the spatial coverage causes the differences in Tb over land between the two sensors. The WindSat has a mean spatial resolution of ~15 Km, whereas MWR has a mean spatial resolution of ~50 Km (~ 3 time the WindSat footprint). This causes the MWR and WindSat observations to be inconsistent, especially for complex terrain and heterogeneous landscapes. It is expected that the higher biases will be over large water bodies, such as coastal areas, Amazon River, and Great Lakes. The results of this analysis are presented below:

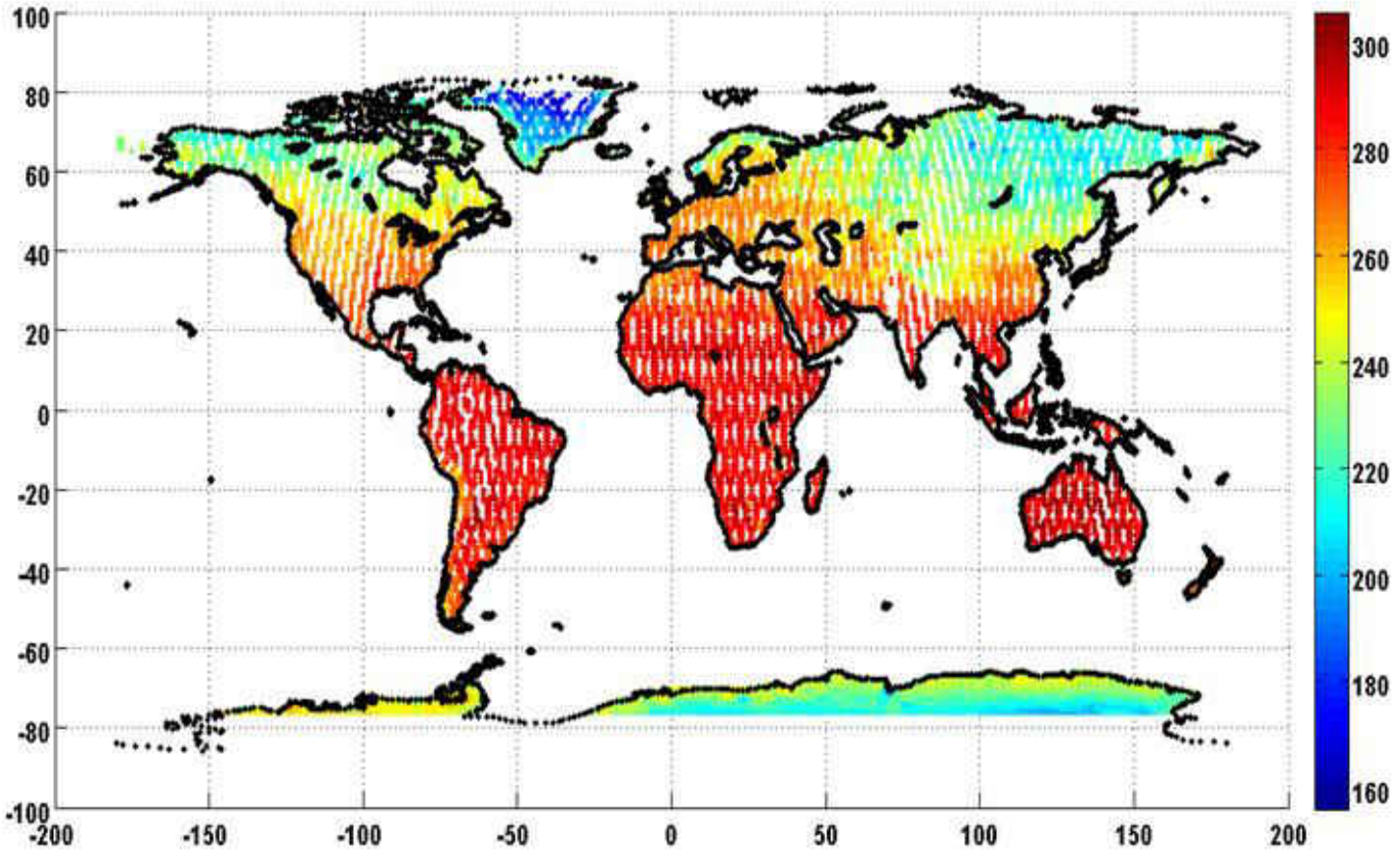

Figure G.1 Global Image of MWR Tb Collocated with WS, color is the scene Tb

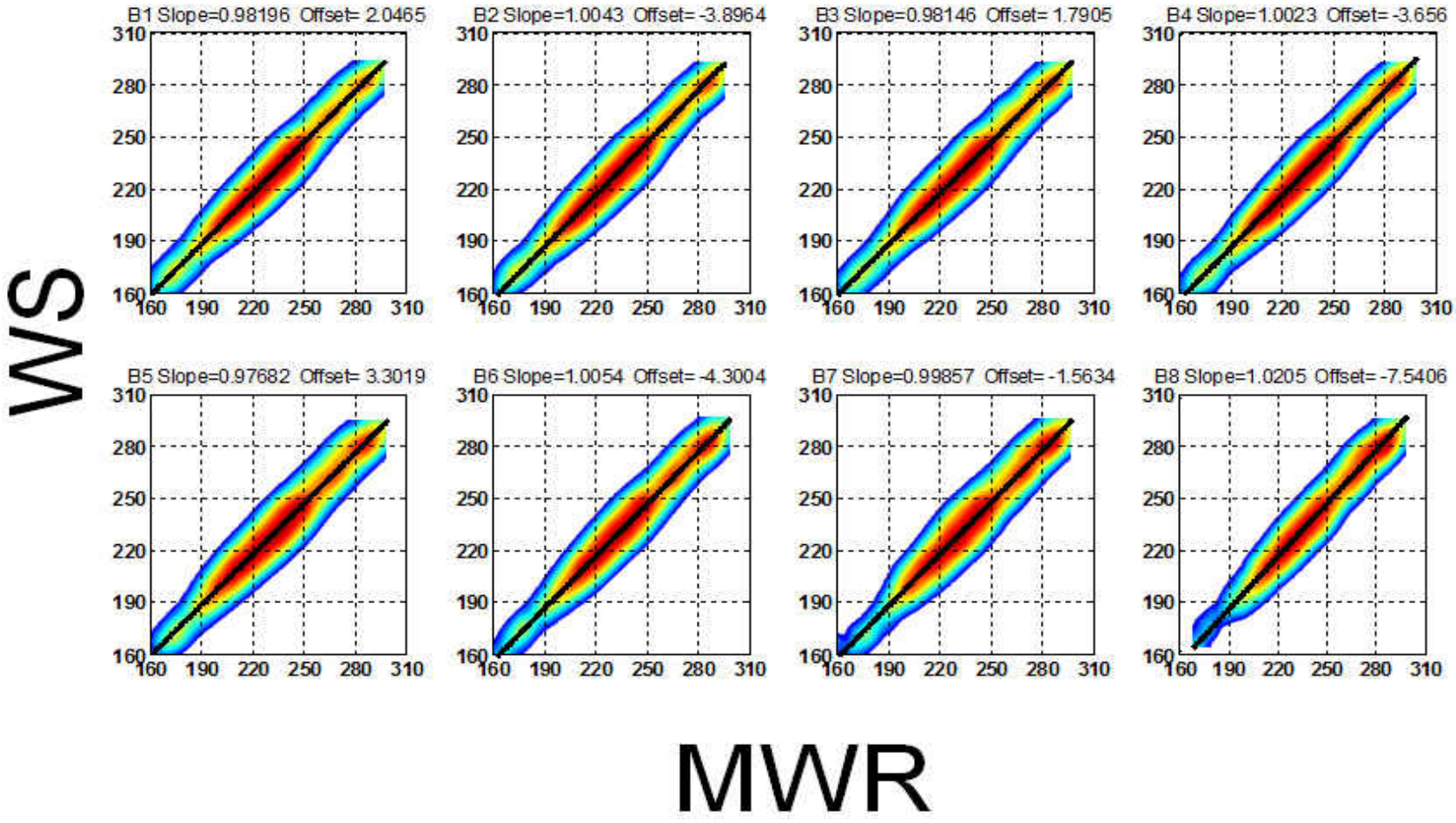

Figure G.2 37V, MWR Tb @ 52°& 58° compared to WindSat Tb @ 53°Ascending Revs, Color is # points

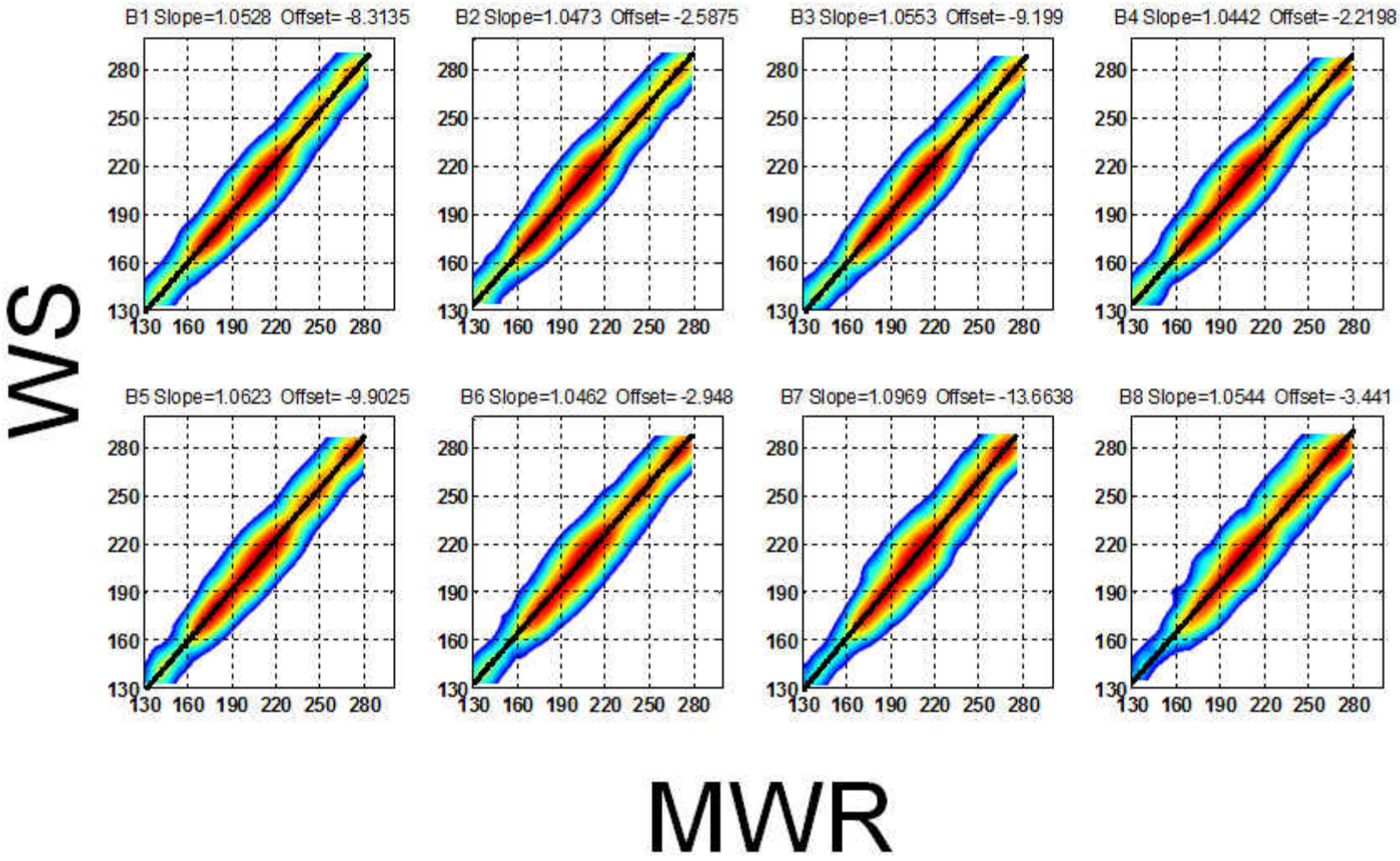

Figure G.3 37H, MWR Tb @ 52°& 58° compared to WindSat Tb @ 53° Ascending Revs, Color is # points

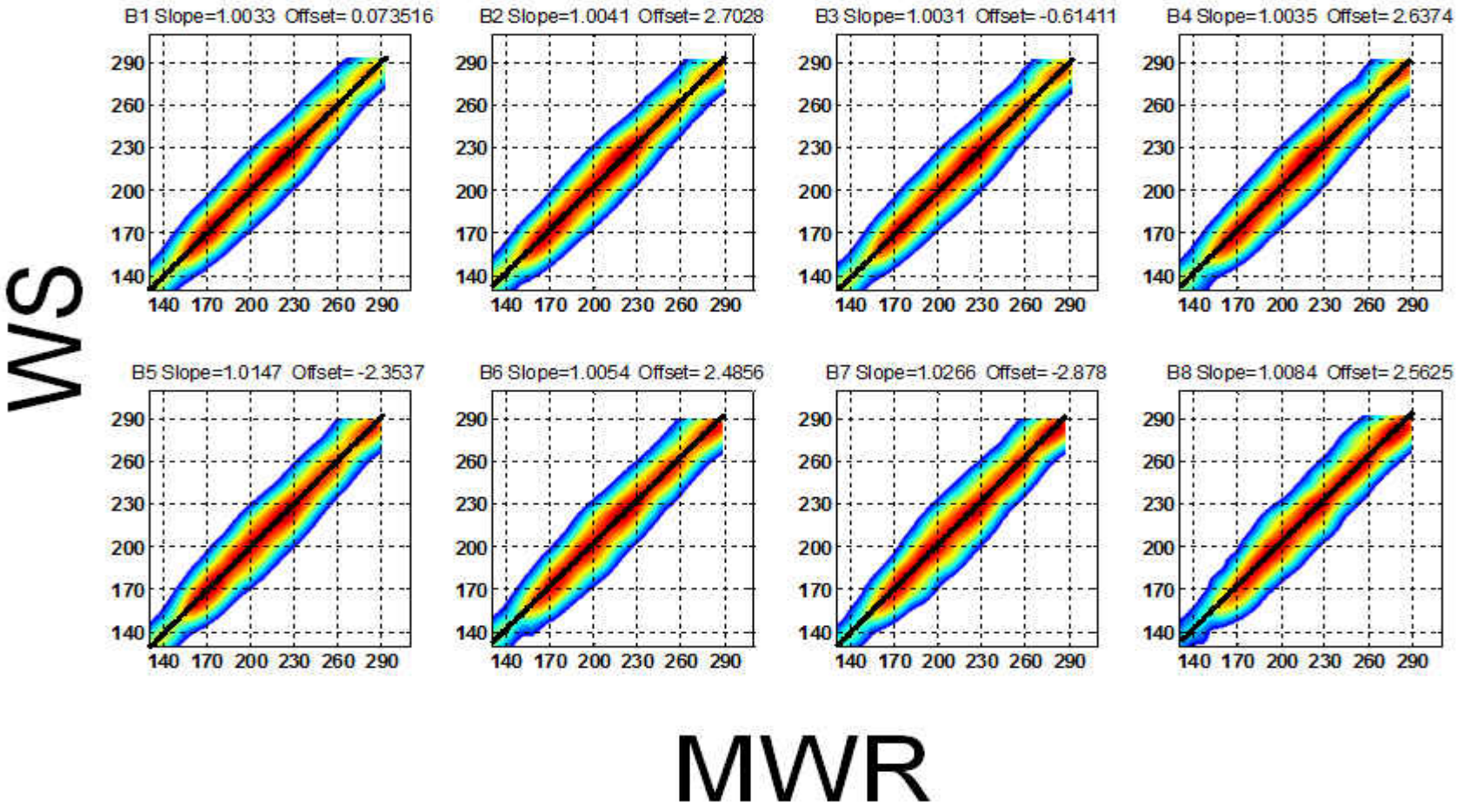

Figure G.4 23H, MWR Tb @ 52°& 58° compared to WindSat Tb @ 53° Ascending Revs, Color is # points

APPENDIX H
MWR TB V7

New MWR Tb dataset will be produced for tuning and validation of the wind speed algorithms. For this analysis, the data from MWR V6.0 from a time period between July 2012 and November 2013 and were chosen. After performing XCAL 5 day average double difference technique, a triangular moving average was applied to derive the smoothed biases that will be used to adjust the MWR Tb's. These new V7.0 Tb's will be normalized to match the WindSat Tb's in the mean to have zero DD Tb-bias. A comparison of the MWR V7 Tb and the adjusted WS are presented below:

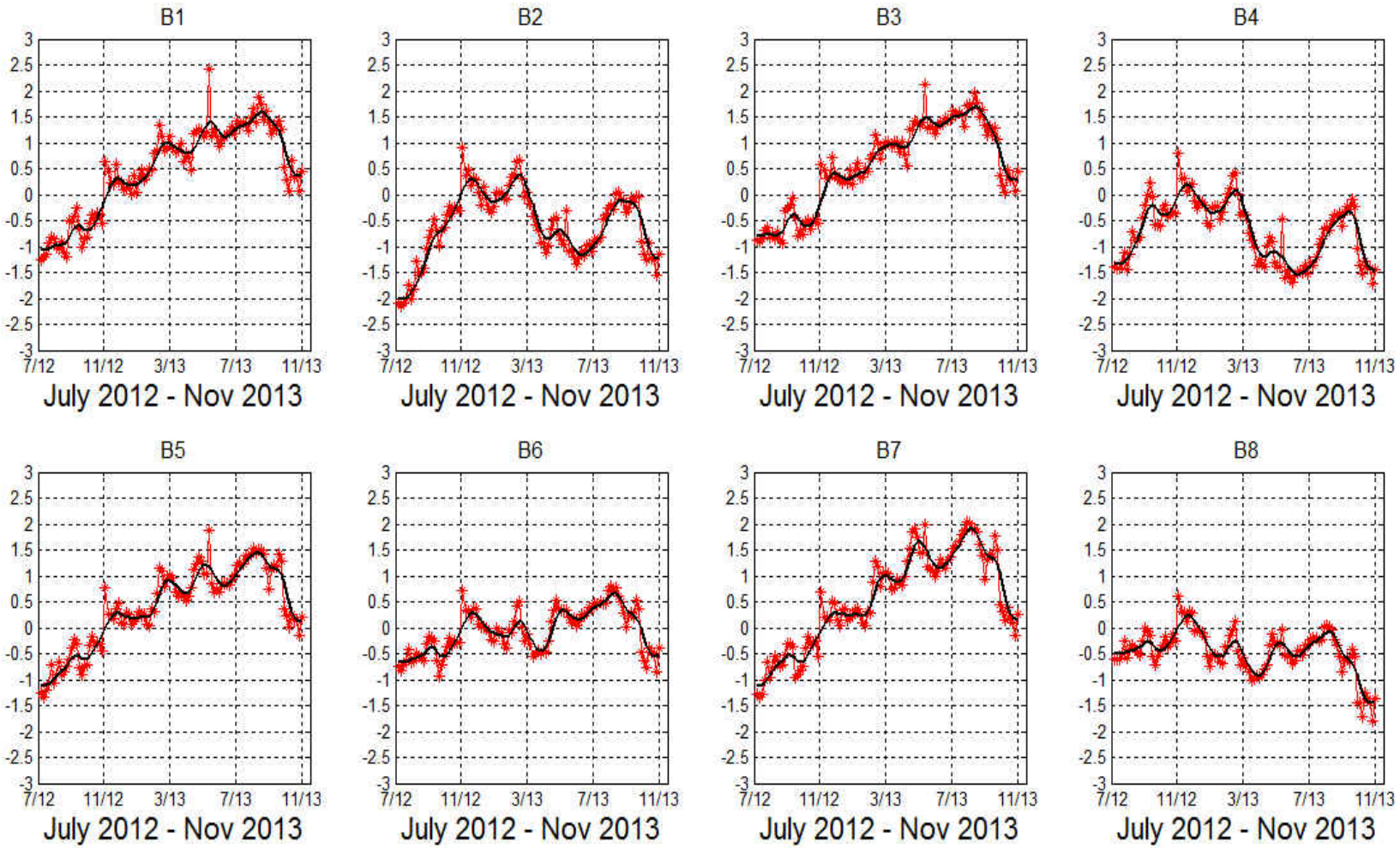

Figure H.1 37H DD biases (MWR-WS)

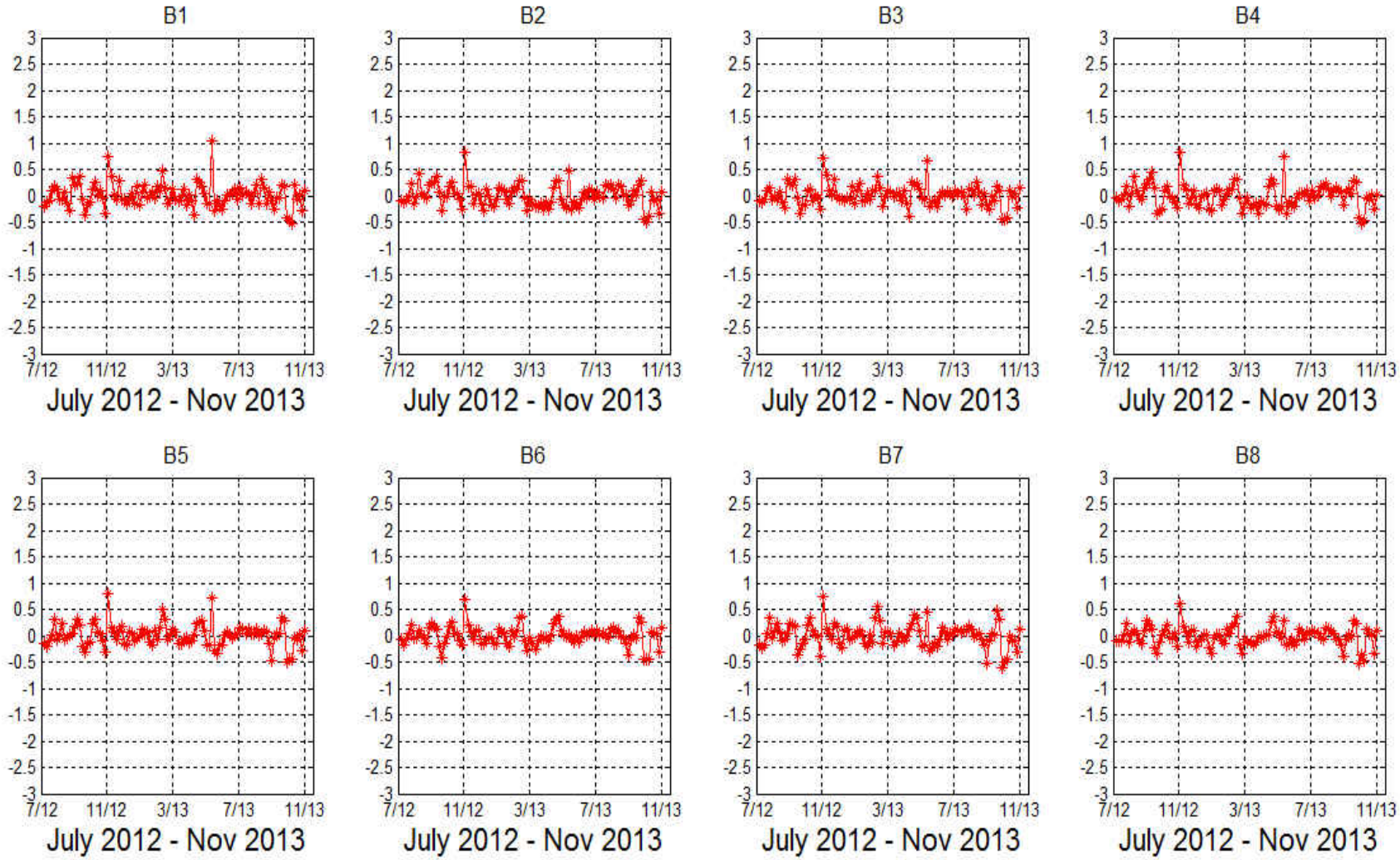

Figure H.2 37H DD adjusted (MWR-WS)

LIST OF REFERENCES

[1] D. M. Le Vine, G. S. E. Lagerloef, and S. E. Torrusio, "Aquarius and Remote Sensing of Sea Surface Salinity from Space," *Proceedings of the IEEE,* vol. 98, pp. 688-703, 2010.

[2] D. M. Le Vine, G. S. E. Lagerloef, F. R. Colomb, S. H. Yueh, and F. A. Pellerano, "Aquarius: An Instrument to Monitor Sea Surface Salinity From Space," *Geoscience and Remote Sensing, IEEE Transactions on,* vol. 45, pp. 2040-2050, 2007.

[3] A. B. Tanner, W. J. Wilson, and F. A. Pellerano, "Development of a high stability L-band radiometer for ocean salinity measurements," in *Geoscience and Remote Sensing Symposium, 2003. IGARSS '03. Proceedings. 2003 IEEE International*, 2003, pp. 1238-1240 vol.2.

[4] M. M. Jacob, *MWR User's Guide-English Version;* Comision De Actividades Especiales, Argentina, Document Code. GS-OIV-OPS-GU-00500-A, October 20, 2010.

[5] Aquarius/SAC-D Microwave Radiometer Critical Design Review data package, Buenos Aires, AR, Aug. 22-24, 2007.

[6] F. T. Ulaby, R. K. Fung, and A. K. Fung; Microwave remote sensing: active and passive.Volume I, Capter 6: Microwave Remote Sensing Fundamentals and Radiometry. Norwood, MA: Artech House, 1981

[7] S. Biswas, "Brightness temperature calibration of Aquarius/SAC-D microwave radiometer (MWR)." Ph.D. Dissertation, University of Central Florida, Orlando, 2011.

[8] S. K. Biswas, S. Farrar, K. Gopalan, A. Santos-Garcia, W. L. Jones, and S. Bilanow, "Intercalibration of Microwave Radiometer Brightness Temperatures for the Global Precipitation Measurement Mission," *Geoscience and Remote Sensing, IEEE Transactions on,* vol. 51, pp. 1465-1477, 2013.

[9] W. L. Jones, J. D. Park, S. Soisuvarn, H. Liang, P. W. Gaiser, and K. M. St Germain, "Deep-space calibration of the WindSat radiometer," *Geoscience and Remote Sensing, IEEE Transactions on,* vol. 44, pp. 476-495, 2006.

[10] S. S. Khan, "Simulation of Brightness Temperatures for the Microwave Radiometer on the Aquarius/SAC-D Mission," M.S. Thesis, University of Central Florida, 2009.

[11] S. Farrar, M. Labanda, M. M. Jacob, S. Masuelli, S. Biswas, H. Raimondo, et al., "An empirical correction for the MWR brightness temperature smear effect*," in Geoscience and Remote Sensing Symposium (IGARSS), 2012 IEEE International*, 2012, pp. 4680-4683.

[12] P. W. Gaiser, K. M. St Germain, E. M. Twarog, G. A. Poe, W. Purdy, D. Richardson, et al., "The WindSat spaceborne polarimetric microwave radiometer: sensor description and early orbit performance," *Geoscience and Remote Sensing, IEEE Transactions on*, vol. 42, pp. 2347-2361, 2004.

[13] Ghazi, Z.; Biswas, S.; Jones, L.; Hejazin, Y.; Jacob, M.M., "On-orbit signal processing procedure for determining Microwave Radiometer non-linearity," *Southeastcon, 2013 Proceedings of IEEE* , vol., no., pp.1,5, 4-7 April 2013 doi: 10.1109/SECON.2013.6567504.

[14] Z. Ghazi, A. Santos-Garcia, M. M. Jacob, and L. Jones, "CONAE Microwave Radiometer (MWR) counts to Tb algorithm and on-orbit validation," in *Microwave Radiometry and Remote Sensing of the Environment (MicroRad), 2014 13th Specialist Meeting on*, 2014, pp. 207-210.

[15] W.J. Wilson, A. Tanner, F. Pellerano, *Ultra Stable Microwave Radiometers for Future Sea Surface Salinity Missions*; Jet Propulsion Laboratory, California Institute of Technology, Pasadena, CA, USA, Tech. Rep. D-31794, April 2005.

[16] \Satellite Toolkit." weblink - http://www.stk.com/.

[17] A. Santos-Garcia, S. Biswas, and L. Jones, "Aquarius/SAC-D Microwave Radiometer brightness temperature validation," in *Oceans, 2012*, 2012, pp. 1-4.

[18] “Aquarius, Sea Surface Salinity from Space. Internet:http://aquarius.nasa.gov.